



**Defense Nuclear Agency  
Alexandria, VA 22310-3398**



**DNA-TR-95-64**

## **Probabilistic Structural Analysis of Deep Tunnels**

**Ben H. Thacker  
David S. Riha  
Y.-T. (Justin) Wu  
Southwest Research Institute  
P.O. Box 28255  
San Antonio, TX 78228-0255**

**February 1996**

**Technical Report**

**19960226 067**

**CONTRACT No. DNA 001-90-C-0134**

**Approved for public release;  
distribution is unlimited.**

**DTIC QUALITY INSPECTED 1**

Destroy this report when it is no longer needed. Do not return to sender.

PLEASE NOTIFY THE DEFENSE NUCLEAR AGENCY,  
ATTN: CSTI, 6801 TELEGRAPH ROAD, ALEXANDRIA, VA  
22310-3398, IF YOUR ADDRESS IS INCORRECT, IF YOU  
WISH IT DELETED FROM THE DISTRIBUTION LIST, OR  
IF THE ADDRESSEE IS NO LONGER EMPLOYED BY YOUR  
ORGANIZATION.



## DISTRIBUTION LIST UPDATE

This mailer is provided to enable DNA to maintain current distribution lists for reports. (We would appreciate your providing the requested information.)

- ☐ Add the individual listed to your distribution list.
- ☐ Delete the cited organization/individual.
- ☐ Change of address.

### NOTE:

Please return the mailing label from the document so that any additions, changes, corrections or deletions can be made easily. For distribution cancellation or more information call DNA/IMAS (703) 325-1036.

NAME: \_\_\_\_\_

ORGANIZATION: \_\_\_\_\_

#### OLD ADDRESS

#### CURRENT ADDRESS

\_\_\_\_\_  
\_\_\_\_\_  
\_\_\_\_\_

\_\_\_\_\_  
\_\_\_\_\_  
\_\_\_\_\_

TELEPHONE NUMBER: (    ) \_\_\_\_\_

#### DNA PUBLICATION NUMBER/TITLE

#### CHANGES/DELETIONS/ADDITIONS, etc.) (Attach Sheet if more Space is Required)

\_\_\_\_\_  
\_\_\_\_\_  
\_\_\_\_\_

\_\_\_\_\_  
\_\_\_\_\_  
\_\_\_\_\_

DNA OR OTHER GOVERNMENT CONTRACT NUMBER: \_\_\_\_\_

CERTIFICATION OF NEED-TO-KNOW BY GOVERNMENT SPONSOR (if other than DNA): \_\_\_\_\_

SPONSORING ORGANIZATION: \_\_\_\_\_

CONTRACTING OFFICER OR REPRESENTATIVE: \_\_\_\_\_

SIGNATURE: \_\_\_\_\_

CUT HERE AND RETURN



DEFENSE NUCLEAR AGENCY  
ATTN: TITL  
6801 TELEGRAPH ROAD  
ALEXANDRIA, VA 22310-3398

DEFENSE NUCLEAR AGENCY  
ATTN: TITL  
6801 TELEGRAPH ROAD  
ALEXANDRIA, VA 22310-3398



REPORT DOCUMENTATION PAGE			Form Approved OMB No. 0704-0188	
Public reporting burden for this collection of information is estimated to average 1 hour per response including the time for reviewing instructions, searching existing data sources, gathering and maintaining the data needed, and completing and reviewing the collection of information. Send comments regarding this burden estimate or any other aspect of this collection of information, including suggestions for reducing this burden, to Washington Headquarters Services, Directorate for Information Operations and Reports, 1215 Jefferson				
1. AGENCY USE ONLY (Leave blank)	2. REPORT DATE 960201	3. REPORT TYPE AND DATES COVERED Technical 900901 - 950630		
4. TITLE AND SUBTITLE Probabilistic Structural Analysis of Deep Tunnels		5. FUNDING NUMBERS C - DNA 001-90-C-0134 PE - 62715H PR - RS TA - RH WU - DH303480		
6. AUTHOR(S)  Ben H. Thacker, David S. Riha, and Y.-T. (Justin) Wu				
7. PERFORMING ORGANIZATION NAME(S) AND ADDRESS(ES) Southwest Research Institute P.O. Box 28255 San Antonio, TX 78228-0255		8. PERFORMING ORGANIZATION REPORT NUMBER 06-3742		
9. SPONSORING/MONITORING AGENCY NAME(S) AND ADDRESS(ES) Defense Nuclear Agency 6801 Telegraph Road Alexandria, VA 22310-3398 SPSD/Senseny		10. SPONSORING/MONITORING AGENCY REPORT NUMBER  DNA-TR-95-64		
11. SUPPLEMENTARY NOTES This work was sponsored by the Defense Nuclear Agency under RDT&E RMC Code B4662D RS RH SPSD 4300A 25904D.				
12a. DISTRIBUTION/AVAILABILITY STATEMENT  Approved for public release; distribution is unlimited.		12b. DISTRIBUTION CODE		
13. ABSTRACT (Maximum 200 words) <p>Accurate and efficient methods for performing probabilistic structural analysis are developed and demonstrated using highly detailed numerical tunnel models. Typical result from the probabilistic analysis include probability of failure, cumulative distribution functions, and probabilistic sensitivities with respect to all input statistical parameters. The results are useful for survivability/vulnerability assessments, strategic planning, tunnel design, and test planning.</p> <p>The report describes a program comprising development and application of several advanced probabilistic analysis methods, verification and validation of deterministic numerical models, and application of probabilistic analysis methods to several different tunnel problems. Statistical properties measured in laboratory testing are used directly in the calculations. A novel probabilistic cap constitutive model is developed that allows the model parameters to be treated as non-normal dependent random variables.</p> <p>The probabilistic methods used are based on a class of methods known as Fast Probability Integration (FPI). For probabilistic finite element analysis, the Advanced Mean Value (AMV) method is generally recommended. The methods are verified using Latin hypercube, adaptive importance sampling, and Monte Carlo Simulation. In the cases studied, the probabilistic methods used were shown to be as accurate as Monte Carlo simulation, but orders of magnitude more efficient.</p>				
14. SUBJECT TERMS Tunnel Probabilistic Analysis Cap Model Vulnerability Assessment		15. NUMBER OF PAGES 88		
		16. PRICE CODE		
17. SECURITY CLASSIFICATION OF REPORT UNCLASSIFIED	18. SECURITY CLASSIFICATION OF THIS PAGE UNCLASSIFIED	19. SECURITY CLASSIFICATION OF ABSTRACT UNCLASSIFIED	20. LIMITATION OF ABSTRACT  SAR	

CLASSIFIED BY:

N/A since Unclassified.

DECLASSIFY ON:

N/A since Unclassified.

## SUMMARY

Southwest Research Institute conducted a research project focused on developing a methodology for calculating the probabilistic response of deep underground tunnels as part of an ongoing program sponsored by DNA. A specific objective of the effort was to develop a methodology that is more efficient than traditional Monte Carlo. Prior to this project, probabilistic analysis of underground structures was made using Monte Carlo simulation; however, due to its inherent inefficiency, only analytical or very simple numerical tunnel models could be employed. Recently, it has been well established by the DNA geomechanics community that predicting tunnel response to highly dynamic loading requires highly-detailed numerical models, which in turn require substantial computational resources and time.

The major result of this project is the development and verification of a suite of probabilistic analysis methods that allow all significant uncertainties in complex numerical tunnel deformation/damage models to be simulated in an efficient manner. Specifically, new and enhanced existing probabilistic analysis algorithms have been developed and integrated with a general-purpose transient dynamic finite element program. We participated in two large verification and validation programs moderated by DNA to gain confidence in the underlying deterministic tunnel models. Several demonstration probabilistic analyses were performed and verified using Monte Carlo and/or other simulation methods. In all cases, the advanced probabilistic methods used were shown to be as accurate as Monte Carlo simulation, but orders of magnitude more efficient.

Several significant advances have been made within the probabilistic algorithms to tailor their use for underground tunnel analysis: a capability for computing efficiently the confidence bounds on the calculated probability of failure due to random and systematic errors; a capability for handling non-normal correlated random variables; new methods for performing sensitivity analysis to assess the impact of changing the mean, standard deviation, or distribution type of any input random variable; and a methodology for treating the estimated coefficients in the finite element constitutive model as random variables.

Specific accomplishments include:

1. An analytical model for predicting tunnel closure was formulated, implemented, and integrated with SwRI's fast probability integration (NESSUS/FPI) program. Probabilistic sensitivity factors computed as a by-product of the FPI calculation provided new insight into the importance ranking of the input variables.
2. A general automated interface was developed between the probabilistic algorithms in NESSUS/FPI and the PRONTO explicit dynamic finite element (FE) program. Any variable pertaining to the analysis can be considered random, e.g., material parameters, loading time history, and boundary conditions. Probabilistic methods such as advanced mean value, adaptive importance sampling, standard Monte Carlo, first order reliability method, second order reliability method, and fast probability integration can all be used.

3. A new method for estimating confidence bounds on the tunnel closure cumulative distribution function was developed and implemented in FPI. Confidence bounds are used to estimate the uncertainty band in a probabilistic prediction due to effects such as statistical uncertainty, bias and systematic errors. The new method is based on FPI's advanced mean value (AMV) probabilistic algorithm. Before this method was developed, Monte Carlo simulation was required to estimate the confidence bounds.
4. A new and general method for treating non-normal correlated random variables in the probabilistic analysis was developed and implemented in FPI. This capability allows the correlation coefficient between any of the random variables to be input regardless of the distribution type specified for each random variable. Prior to this development, only random variables having certain distribution functions could be correlated.
5. A probabilistic cap model methodology was developed and implemented. The development of the model focused on the accurate description of the parameter uncertainties in the constitutive model. The current model treats the parameters as random variables, since they can be measured and statistically modelled. Statistical parameters are estimated from repeat laboratory tests.
6. Several sensitivity calculations have been developed and implemented. First-order approximate sensitivities with respect to the mean and standard deviation of each input random variable are computed from the probabilistic sensitivity factors produced as a by-product of the FPI calculation. A new method for computing these same sensitivities which re-uses the samples used by the adaptive importance sampling (AIS) method has been developed. Finally, the sensitivity of the calculated probability with respect to the choice of input distribution has also been developed.
7. Several demonstrative probabilistic analyses have been performed using 1) an analytical tunnel closure model; 2) a transient dynamic FE model of a deep tunnel (500m deep), and 3) FE models of the SRI SWAT precision tests, and 4) a shallow tunnel targeting/vulnerability problem. In these analyses, the advanced probabilistic methods were shown to be accurate and orders of magnitude more efficient than Monte Carlo simulation.

Many of the algorithms enhanced and/or implemented on the DNA project were developed to some degree by a 9-year NASA project with SwRI entitled "Probabilistic Structural Analysis Methods for Select Space Shuttle Components" (PSAM). PSAM was aimed at developing probabilistic structural analysis methods for space shuttle main engine applications. This significant level of technology transfer from this NASA project to the DNA project greatly increased the scope and magnitude of accomplishments than what would have otherwise been possible.

## PREFACE

This research was conducted by Southwest Research Institute (SwRI) under Contract No. DNA001-90-C-0134 with the Defense Nuclear Agency (DNA) under the supervision of Dr. Paul E. Senseny. The authors would like to thank Dr. Senseny for his guidance and many helpful technical discussions throughout the program. The authors are also indebted to the following individuals for their significant contributions: Dr. Arlo Fossum (RE/SPEC) for his leadership and many enlightening discussions regarding the probabilistic cap model development, Dr. John Osnes (RE/SPEC) for his assistance in performing the Benchmark calculations, Dr. Tony Tornø (Rockwell) and Mr. Harry Millwater for their help with some of the probabilistic calculations, Dr. James Walker for help with implementing constitutive models, and Ms. Lori Salas and Ms. Linette McCord for their preparation of the manuscript.

## TABLE OF CONTENTS

Section	Page
SUMMARY .....	iii
PREFACE .....	v
1 INTRODUCTION .....	1
1.1 BACKGROUND .....	1
1.2 OBJECTIVE .....	1
1.3 SCOPE .....	2
2 DETERMINISTIC TUNNEL MODELS .....	3
2.1 INTRODUCTION .....	3
2.2 ANALYTICAL ELASTOPLASTIC TUNNEL CLOSURE MODEL .....	3
2.3 EXPLICIT DYNAMIC FINITE ELEMENT MODEL .....	4
2.3.1 Explicit Time Integration .....	5
2.3.2 Four Node Uniform Strain Element .....	6
2.3.3 Material Behavior .....	6
2.3.4 Transmitting Boundary Conditions .....	14
3 VERIFICATION AND VALIDATION OF DETERMINISTIC TUNNEL MODELS .....	16
3.1 INTRODUCTION .....	16
3.2 BENCHMARK ACTIVITY .....	16
3.3 PRECISION TEST MODELING .....	17
3.3.1 Static Tunnel Tests in Limestone .....	17
3.3.2 Dynamic Tunnel Tests in Limestone .....	25
3.3.3 Summary of PTM Exercise .....	31

## TABLE OF CONTENTS (Continued)

Section	Page
4	PROBABILISTIC ANALYSIS METHODS ..... 33
4.1	INTRODUCTION. .... 33
4.2	UNCERTAINTY MODELING ..... 33
4.2.1	Random Variables and Systematic Errors ..... 33
4.2.2	Random Fields and Spatial Variability ..... 35
4.3	LIMIT STATE FUNCTION ..... 35
4.4	SIMULATION METHODS ..... 36
4.4.1	Monte Carlo Simulation ..... 37
4.4.2	Latin Hypercube Simulation ..... 37
4.4.3	Adaptive Importance Sampling ..... 38
4.5	FAST PROBABILITY INTEGRATION ..... 39
4.6	ADVANCED MEAN VALUE METHOD ..... 40
4.7	CORRELATED NON-NORMALS ..... 41
4.8	CONFIDENCE BOUNDS ..... 43
4.9	SENSITIVITY ANALYSIS ..... 44
4.9.1	Design Sensitivities ..... 45
4.9.2	Probabilistic Sensitivities ..... 45
4.9.3	Sampling Based Probabilistic Sensitivities ..... 47
4.9.4	Sensitivity to Distribution Type ..... 48
5	NUMERICAL EXAMPLES ..... 49
5.1	ANALYTICAL TUNNEL CLOSURE MODEL ..... 49
5.2	PROBABILISTIC DEEP TUNNEL ANALYSIS ..... 53
5.3	TUNNEL VULNERABILITY ANALYSIS ..... 58
5.4	PROBABILISTIC SWAT-II ANALYSIS ..... 65
6	REFERENCES ..... 70

## FIGURES

Figure		Page
2-1	Analytical tunnel problem geometry: a) case 1 - outer elastic and three plastic zones, b) case 2 - outer elastic and two plastic zones .....	4
2-2	Sandler-Rubin cap model .....	9
2-3	Yield surfaces in the $\pi$ -plane .....	10
3-1	SRII static test configuration .....	18
3-2	Sandler-Rubin cap model. Also shown are the load paths from the SRII static tunnel tests and the smooth cap model .....	19
3-3	Comparison of experimental and predicted aluminum liner response .....	20
3-4	ST1 Crown-invert closures: a) 2-invariant, b) 3-invariant .....	21
3-5	ST1 Springline closures: a) 2-invariant, b) 3-invariant .....	22
3-6	ST2 Crown-invert closures: a) 2-invariant, b) 3-invariant .....	23
3-7	ST2 Springline closures: a) 2-invariant, b) 3-invariant .....	23
3-8	ST3 Crown-invert closures: a) 2-invariant, b) 3-invariant .....	24
3-9	ST3 Springline closures: a) 2-invariant, b) 3-invariant .....	24
3-10	SWAT-II test configuration .....	26
3-11	SwRI SWAT-II wedge mesh. ....	27
3-12	Free-field radial stresses at R=14.5cm. Predictions based on rate-independent model. ....	28
3-13	Free-field radial stresses at R=14.5cm. Predictions based on rate-dependent models: a) uncalibrated, b) calibrated. ....	28
3-14	SWAT-II crown-invert closures for R=14.5 cm tunnel: a) rate-independent, b) rate-dependent .....	29



## FIGURES (Continued)

Figure	Page
3-15 SWAT-II springline closures for R=14.5 cm tunnel: a) rate-independent, b) rate-dependent .....	30
3-16 SWAT-II crown-invert closures for R=19.2 cm tunnel: a) rate-independent, b) rate-dependent .....	30
3-17 SWAT-II springline closures for R=19.2 cm tunnel: a) rate-independent, b) rate-dependent .....	31
4-1 Normal and extreme value pdf .....	34
4-2 Illustration of the adaptive importance sampling (AIS) method .....	38
4-3 Joint pdf and MPP for two random variables in standard normal (u) space .....	40
4-4 50% and 95% confidence bounds for the analytical tunnel closure model .....	44
5-1 Cumulative distribution function for the analytical tunnel closure model .....	50
5-2 Probabilistic sensitivity factors ( $\alpha$ ) at cdf=15% or $p_k=0.85\%$ . As shown, Young's Modulus and external pressure are dominate .....	50
5-3 Design sensitivities at approximately $p_k=0.85$ .....	51
5-4 Probabilistic sensitivity with respect to mean .....	51
5-5 Probabilistic sensitivity with respect to standard deviation .....	52
5-6 Sensitivity to change in probability distribution type .....	53
5-7 Problem description, finite element mesh, and loading .....	54
5-8 Deformed shape plots magnified 10X for several times during the analysis and the time history of crown-invert closure .....	55

## FIGURES (Continued)

Figure	Page
5-9 Cumulative distribution function for crown-invert tunnel closure .....	57
5-10 Probabilistic sensitivity factors for the deep tunnel problem .....	57
5-11 Conceptual tunnel vulnerability model .....	58
5-12 Deterministic calculation procedure .....	60
5-13 Damage functions .....	61
5-14 Sequence of penetration calculations at different aimpoints, X .....	61
5-15 Deterministic calculational results: a) variation of penetration depth (left scale) and standoff (right scale) with aimpoint; b) variation in damage with aimpoint ...	62
5-16 Vulnerability function ( $=1-\text{cdf}$ ) .....	63
5-17 Variation in probability of kill with aimpoint .....	64
5-18 Nondimensionalized sensitivity of $p_k$ with respect to the mean of each parameter .	64
5-19 Nondimensionalized sensitivity of $p_k$ with respect to the standard deviation of each parameter .....	65
5-20 Refined mesh used for the probabilistic SWAT-II analysis .....	66
5-21 CDF of crown-invert closure showing 50% and 80% confidence bounds .....	68
5-22 Nondimensionalized sensitivity of $\beta$ with respect to the mean .....	68
5-23 Nondimensionalized sensitivity of $\beta$ with respect to the standard deviation .....	69

## TABLES

Table		Page
3-1	Sandler-Rubin cap model properties for Salem limestone .....	20
3-2	Duvaut-Lions viscoplastic parameter values .....	26
4-1	Monte Carlo simulation analysis times based on 5% error .....	36
4-2	Finite element solutions required to compute a CDF using the AMV+, p-levels, procedure .....	41
5-1	Random variables used in the probabilistic analysis .....	49
5-2	Problem variables and inputs .....	55
5-3	Model variables used in the tunnel targeting problem .....	59
5-4	Parameter summary .....	66
5-5	Correlation matrix .....	67
5-6	COV for the random variable mean and standard deviation .....	67

## SECTION 1

### INTRODUCTION

#### 1.1 BACKGROUND.

Predicting the behavior and failure of deep underground tunnels in severe loading environments is now becoming possible with new computational techniques and more powerful computers. The problems are highly transient, involve nonlinear material behavior and include large uncertainties in material properties, loading, and geometry. Sophisticated numerical models based on finite and distinct element methods are being developed and applied to these problems. However, computational costs are high as even a single analysis may require hours of computer time. This computational cost coupled with the need to account for uncertainties in a direct manner has led to the development and application of efficient probabilistic analysis methods.

Parameters used to describe geomechanics problems are known to possess large uncertainties. These large uncertainties in material properties, loading, and geometry stem from the fact that the composition of most rock is highly variable and includes joints and faults not accounted for in material testing. An assessment of the variability or randomness of the structural behavior and/or failure requires careful study for a thorough understanding of the problem. The traditional method of accounting for uncertainties is a factor-of-safety approach. However, this approach does not quantify the failure probability of a given design, which can lead to either overconservative or unreliable designs, nor does it identify the variable contributing the most to the failure probability.

The traditional method of probabilistic analysis is Monte Carlo simulation. This approach generally requires hundreds of thousands of simulations, and is impractical when each simulation involves extensive numerical calculations. The pursuit of alternative probabilistic analysis methods that are more efficient than Monte Carlo simulation has led to the development of many new approximate probabilistic methods over the past two decades. Many of these methods have been shown to be highly-accurate and applicable for use with complex numerical deterministic models.

#### 1.2 OBJECTIVE.

The objective of this research was to develop a methodology that predicts the uncertainty in structural deformation and damage in underground tunnels given the uncertainty in geologic and reinforcing-structure parameters. The method was to be more efficient than traditional Monte Carlo. The development of fast-running engineering models for tunnel response was also required.

The approach taken was to:

1. Develop a three-dimensional numerical model for the response of deep-buried tunnels.
2. Verify and validate the deterministic numerical model.
3. Develop and integrate efficient probabilistic methods with the validated deterministic model.
4. Prepare probabilistic inputs.
5. Calculate the uncertainty in structural deformation and identify key problem variables for several selected problems.
6. Demonstrate probabilistic analysis methods using a fast-running tunnel targeting model.

### 1.3 SCOPE.

To satisfy the objective, several new and efficient probabilistic methods were developed and integrated with a general purpose numerical model. A common element to the methods is the use of fast probability integration (FPI) algorithms, which have been shown to be many times more efficient than Monte Carlo simulation (Wu and Wirsching, 1987). The advanced mean-value (AMV) procedure, which is based on FPI, was found to be extremely efficient in computing the probabilistic response of complex structures with relatively few response calculations. As a means of verification, several advanced simulation methods were also employed such as Latin Hypercube Simulation (LHS) and Adaptive Importance Sampling (AIS)

This report is organized as follows: Section 2 summarizes the development of two deterministic models; an analytical tunnel closure model and a more general purpose finite element (FE) model. Section 3 reports on the verification and validation of the FE model. In Section 4, the probabilistic methods employed are presented. The probabilistic FE model is demonstrated on several problems in Section 5, including a deep tunnel analysis, a dynamic laboratory experiment, and a tunnel vulnerability problem. References to the literature are used where possible to keep the report concise.

## SECTION 2

### DETERMINISTIC TUNNEL MODELS

#### 2.1 INTRODUCTION.

In this Section, two deterministic models are presented. The first model, based on the work of Hendron-Aiyer (1972), has been used for tunnel analysis and includes both elastic and plastic closure. Although the model makes several simplifying assumptions, it has been used extensively in the DNA community for making rapid assessments and has performed remarkably well. The second model is a general-purpose finite element solid dynamics program (PRONTO) employing several constitutive models for modeling the elastic and plastic response of intact rock and joints. Since PRONTO is developed and maintained by Sandia National Laboratories (SNL) and is available for government and commercial use, the enhancements made to PRONTO during the course of this program are readily available.

#### 2.2 ANALYTICAL ELASTOPLASTIC TUNNEL CLOSURE MODEL.

The problem solved is that of a long, circular tunnel of radius  $a$  in an elastic-perfectly plastic Mohr-Coulomb material subjected to static axisymmetric pressure on the boundary of the tunnel and also at infinity. Plane strain is assumed along the axis of the tunnel, and the plastic flow of the medium may be nonassociative. The solution assumes that the internal and far-field pressure are increased together until the desired internal pressure is imposed. The far-field pressure is then further increased, resulting in yielding of the medium around the tunnel and increased tunnel closure.

The problem geometry is given in Figure 2-1. The variables in the model are Young's modulus, Poisson's ratio, unconfined compressive strength, angle of internal friction, a dilation parameter, internal pressure, and external pressure.

The formulae for tunnel closure,  $\Delta D/D$ , are given in Thacker and Senseny (1992) from the solution for the stress and displacement fields obtained by Wintergerst, *et al.*, (1991). Their work extended the solutions obtained by Florence and Schwer (1978) to allow for non-associated plastic flow. The Florence and Schwer solution removed the constraint of earlier solutions (Newmark, 1969; Hendron and Aiyer, 1972) that the least compressive principal stress be the radial stress. A complete description of the model and the analytical tunnel closure equations can be found in Thacker and Senseny (1992).

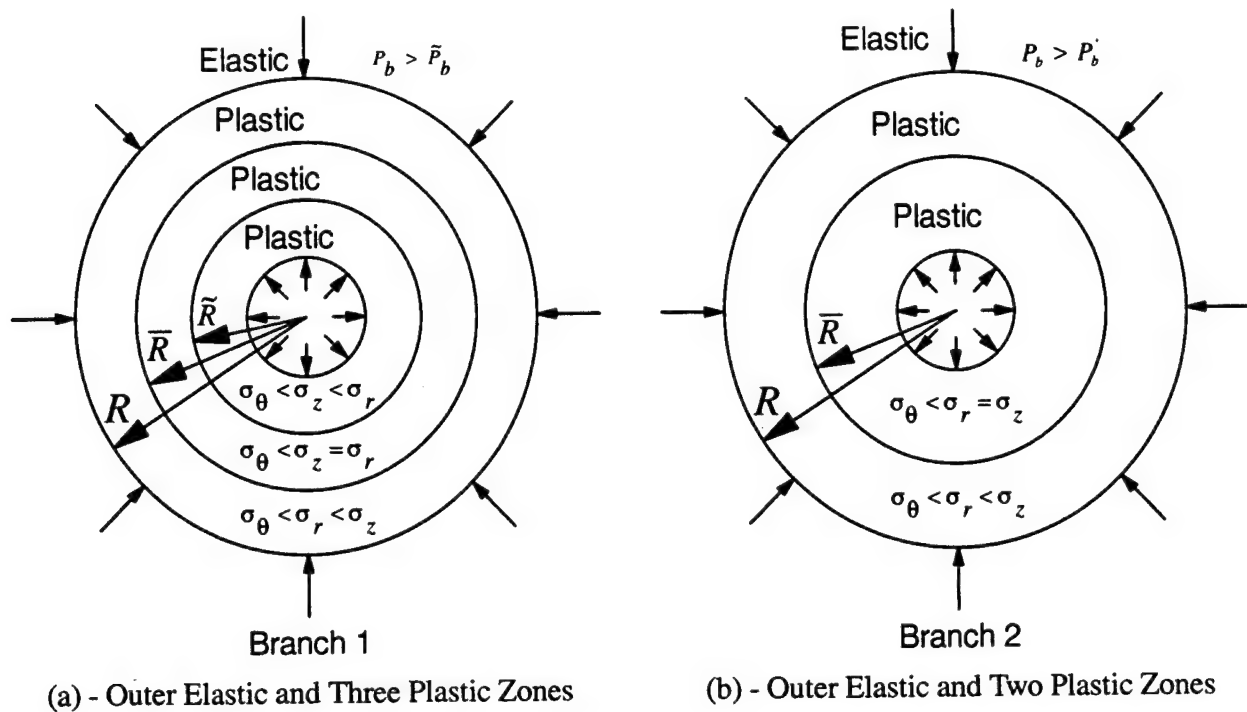


Figure 2-1. Analytical tunnel problem geometry: a) case 1 - outer elastic and three plastic zones, b) case 2 - outer elastic and two plastic zones.

## 2.3 EXPLICIT DYNAMIC FINITE ELEMENT MODEL.

PRONTO2D is a two-dimensional transient solid dynamics code for analyzing large deformations of highly nonlinear materials subjected to extremely high strain rates (Taylor and Flanagan, 1987). It is the latest in a series of transient dynamic finite element codes that have been developed at Sandia National Laboratories, beginning with HONDO (Key, *et al.*, 1978). As such, PRONTO2D contains a number of state-of-the-art numerical algorithms, including an adaptive timestep control algorithm, a robust hourglass control algorithm, a very accurate incremental rotation algorithm, and a robust surface contact algorithm. Four-noded, uniform-strain, quadrilateral elements with single-point integration are used in the finite element formulation. Beyond its general capabilities, PRONTO2D was chosen for the calculations because new constitutive models are readily added and because a three-dimensional derivative of the program is available (PRONTO3D).

The two features that make the deep tunnel calculations relatively unique among large-deformation solid dynamics problems are: 1) a jointed rock mass subject to loading conditions that could result in large relative motions (sliding) between adjacent rock blocks, and 2) loading conditions that could result in substantial tensile failure, plastic deformation, and dilation within the rock blocks. The joints also affect the elastic behavior of the rock mass by reducing its elastic moduli from the intact rock values. Further, the elastic moduli of jointed rock generally are nonlinear functions of the joint apertures.

The surface contact algorithm in PRONTO2D is directly applicable to modeling the slippage between adjacent rock blocks. It is designed to simulate smooth, cohesionless surfaces with shear strengths defined in terms of static and dynamic coefficients of friction. In the tunnel problems, the static coefficient of friction is the tangent of the joint friction angle. The friction coefficient does not decay during sliding, so the dynamic coefficient of friction is equal to the static coefficient.

The surface contact algorithm does not provide a means to model the elastic behavior of the joints. Consequently, the approach used is to superpose the nonlinear stress-displacement response of the joints and the linear stress-strain response of the intact rock. The result is a composite material whose elastic behavior is equivalent to a jointed rock mass. This approach has been developed and used successfully by other modelers (Labreche and Petney, 1987) and it is referred to as the Complaint Joint Model (CJM). Note that the elastic behavior of jointed rock masses and as simulated by the CJM is inherently anisotropic because the stress-strain response normal to a joint set is substantially different from the response tangential to the joint set.

### 2.3.1 Explicit Time Integration.

The equations of motion are integrated using a modified central difference scheme in PRONTO2D. The velocities are integrated with a forward difference and the displacements are integrated with a backward difference. This scheme is expressed as

$$\begin{aligned}\ddot{u}_t &= \frac{f_t^{EXT} - f_t^{INT}}{m} \\ \dot{u}_{t+\Delta t} &= \dot{u}_t + \Delta t \ddot{u}_t \\ u_{t+\Delta t} &= u_t + \Delta t \dot{u}_{t+\Delta t}\end{aligned}\tag{2.1}$$

where  $f_t^{EXT}$  is the external nodal force,  $f_t^{INT}$  is the internal nodal force,  $m$  is the nodal point lumped mass, and  $\Delta t$  is the time increment. This central difference operator is conditionally stable and the Courant stability limit is given by the highest eigenvalue  $\omega_{max}$  of the system (Bathe and Wilson, 1976)

$$\Delta t \leq \frac{2}{\omega_{max}}.\tag{2.2}$$

Flanagan and Belytschko (1984) provided eigenvalue estimates for the uniform strain quadrilateral used in PRONTO2D.

Numerical damping is introduced in the solution by adding artificial viscosity. This prevents high velocity gradients from collapsing an element before it has a chance to respond and to quiet truncation frequency ringing. The technique used in PRONTO2D is to add viscosity to the "bulk" response. This generates a viscous pressure in terms of the volume strain rate.



### 2.3.2 Four Node Uniform Strain Element.

PRONTO2D uses a four-noded two-dimensional uniform strain element in the finite element formulation. A one point integration of the element under-integrates the element but provides a large computational advantage over a two-by-two integration rule. However, this results in a rank deficiency for the element that may cause spurious zero energy (hourglass) modes.

The uniform strain element considers only a fully linear field. Any remaining nodal velocity field is the hourglass field. Possibly severe unrestricted mesh distortion can occur if these modes are excited. The method used in PRONTO2D isolates the hourglass modes so they may be treated independently of the rigid body and uniform strain modes (Flanagan and Belytschko, 1981). PRONTO3D, which also uses reduced integration elements, uses a similar approach to control hourglassing.

### 2.3.3 Material Behavior.

**2.3.3.1 Drucker-Prager.** Several classical yield surfaces defined in terms of the first stress invariant and the second deviatoric stress invariant have been used to model plasticity in rock. They include the linear Mohr-Coulomb and the Drucker-Prager yield criteria. The Drucker-Prager yield function is

$$f(\sigma_y) = \sqrt{J_2'} - \alpha J_1 - k \quad (2.3)$$

where  $\sigma_y$  are the components of the stress tensor,  $\alpha$  and  $k$  are material constants,  $J_1$  is the first invariant of the stress tensor, and  $J_2'$  is the second invariant of the deviatoric stress tensor. The yield surface is the locus of stress states at which the value of the yield function is zero ( $f = 0$ ). Consequently, the Drucker-Prager yield surface is a cone in principal stress space with the axis of the cone along the hydrostat.

The Drucker-Prager and the Mohr-Coulomb yield criteria are equivalent only at certain stress states, depending on how the Drucker-Prager material constants are evaluated. To match the Mohr-Coulomb criterion in triaxial compression, the material constants must be evaluated as follows:

$$\alpha = \frac{2 \sin \phi}{\sqrt{3}(3 - \sin \phi)} \quad (2.4)$$
$$k = \left( \frac{2\sqrt{3} \cos \phi}{3 - \sin \phi} \right) c_0$$

where  $\phi$  and  $c_0$  are the Mohr-Coulomb friction angle and cohesion, respectively. The resultant Drucker-Prager yield surface circumscribes the Mohr-Coulomb yield surface.

The stress state is elastic when the yield function is negative ( $f < 0$ ). When the stress state is on the yield surface ( $f = 0$ ) and the loading condition is such that it would result in  $f \geq 0$ , the

resulting deformation is plastic. The components of the resultant plastic strain tensor are defined in terms of the flow rule, which is classically stated as proportional to the gradient of a plastic potential function  $g(\sigma_y)$ . The proportionality constant is determined by the consistency condition which requires that the stress state remain on the yield surface during plastic deformation. When the plastic potential function and the yield function coincide for all stress states ( $g=f$ ) the flow rule is said to be associated with the yield function.

An incremental method using tangent stiffness (Chen and Han, 1988) is used to implement Drucker-Prager plasticity in the constitutive model that was added to PRONTO2D for the benchmark problems. The incremental stress-strain relationship can be expressed in the following general form:

$$d\sigma_{ij} = \left[ C_{ijkl} - \frac{C_{ijmn} \frac{\partial g}{\partial \sigma_{mn}} \frac{\partial f}{\partial \sigma_{pq}} C_{pqkl}}{\frac{\partial f}{\partial \sigma_{rs}} C_{rstu} \frac{\partial g}{\partial \sigma_{tu}}} \right] d\epsilon_{kl} \quad (2.5)$$

where  $d\sigma_{ij}$  and  $d\epsilon_{kl}$  are the components of the incremental stress and strain tensors, respectively,  $C_{ijkl}$  are the components of the elastic coefficient tensor, and repeated subscripts indicate summation. The coefficient tensor in the brackets represents the elastic-plastic tensor of tangent moduli for an elastic-perfectly plastic material. The quantities in the brackets, including  $C_{ijkl}$  for a nonlinear elastic material such as in the CJM, are evaluated at the current stress state.

For the Drucker-Prager yield surface, the partial derivatives of the yield function with respect to the stress components are

$$\frac{\partial f}{\partial \sigma_{ij}} = \frac{s_{ij}}{2\sqrt{J_2}} - \alpha \delta_{ij} \quad (2.6)$$

where  $s_{ij}$  are the components of the deviatoric stress tensor, ( $s_{ij} = \sigma_{ij} - \delta_{ij} J_1/3$ ) and  $\delta_{ij}$  is the Kronecker delta function. In the constitutive model added to PRONTO2D the following extended form of the plastic potential function associated with the Drucker-Prager yield function is used:

$$g(\sigma_y) = \sqrt{J_2} - \beta J_1 - k \quad (2.7)$$

where

$$\beta = \frac{2 \sin \psi}{\sqrt{3} (3 - \sin \psi)} \quad (2.8)$$

and  $\psi$  is the dilation angle. The plastic potential function results in an associated flow rule when the dilation angle equals the friction angle (so that  $\beta = \alpha$  and  $g = f$ ). The components of the flow rule (the partial derivatives of  $g$  with respect to  $\sigma_y$ ) are

$$\frac{\partial g}{\partial \sigma_y} = \frac{s_y}{2\sqrt{J_2'}} - \beta \delta_y \quad (2.9)$$

**2.3.3.2 Cap Model.** The Sandler-Rubin (SR) cap model proposed in Sandler and Rubin (1979) is an isotropic rate-independent elastic-plastic material model based on the classical incremental theory of plasticity. It has been used to model both high and low pressure mechanical behavior of many geologic materials such as sands, clays and rocks because of its ability to simulate the important characteristics of these materials: compaction, dilatancy, shear and hysteresis. The yield surface consists of a fixed failure envelope given by

$$F_F(J_1) = \sqrt{J_2'} = A - C \exp[B \cdot J_1] \quad \text{for } J_1 > L(\kappa) \quad (2.10)$$

and a hardening yield function (or cap) given by

$$F_C(J_1, \kappa) = \sqrt{J_2'} = \frac{1}{R} \sqrt{[X(\kappa) - L(\kappa)]^2 - [J_1 - L(\kappa)]^2} \quad \text{for } L(\kappa) \geq J_1 \geq X(\kappa) \quad (2.11)$$

where  $A$ ,  $B$ , and  $C$  are the parameters defining the shear failure surface,  $J_1$  is the first invariant of the stress tensor,  $J_2'$  is the second invariant of the deviatoric stress tensor,  $\kappa$  is a hardening variable related to the total plastic volumetric strain,  $X(\kappa)$  and  $L(\kappa)$  are the values of  $J_1$  at the intersection of the cap with the  $J_1$  axis and center of the cap respectively, and  $R$  is the ratio of the major to minor axes of the elliptical cap. In (2.11),

$$L(\kappa) = \begin{cases} \kappa & \text{if } \kappa < 0 \\ 0 & \text{if } \kappa \geq 0 \end{cases} \quad (2.12)$$

and

$$X(\kappa) = L(\kappa) - R\{A - C \exp[B \cdot L(\kappa)]\} = L(\kappa) - R \cdot F_F(L(\kappa)). \quad (2.13)$$

The hardening variable  $\kappa$  is related to the plastic volume strain  $\bar{\epsilon}_v^p$  (caused only by cap action) through the relationship

$$\bar{\epsilon}_v^p = W\{\exp[D(X(\kappa) - X_0)] - 1\} \quad (2.14)$$

Where  $X_0$  is the initial location of the cap, and to keep the cap from retracting (for rocks)

$$\bar{\epsilon}_v^p = \min(\epsilon_v^p, 0). \quad (2.15)$$

The original SR cap was generalized to accommodate the anisotropic elastic CJM model.

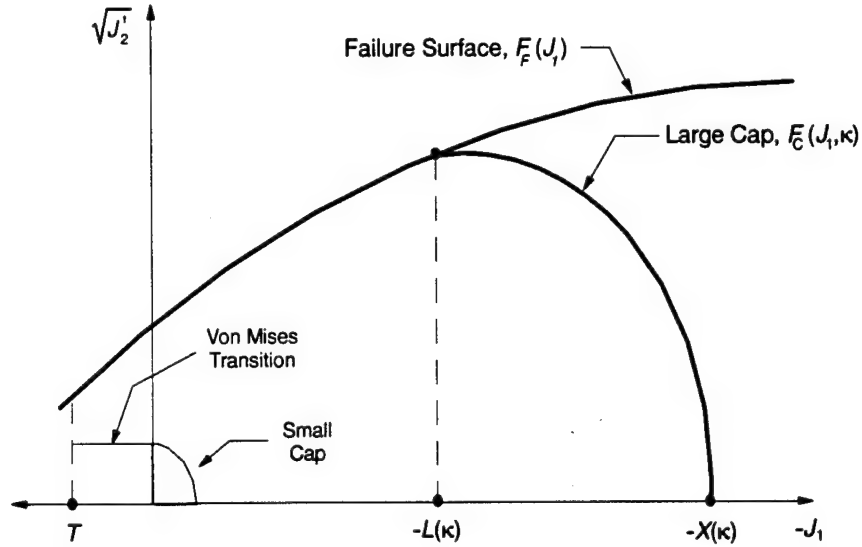


Figure 2-2. Sandler-Rubin cap model.

The failure surface of the SR cap model is also modified to account for different strengths in triaxial extension (TXE) and triaxial compression (TXC). Specifically, the failure surface defined by

$$f = \sqrt{J_2'} - \mathfrak{R} \cdot Y \quad (2.16)$$

is modified by  $\mathfrak{R}$  resulting in a smoothly-varying yield surface in the  $\pi$ -plane, as shown in Figure 2-3.  $\mathfrak{R}$  is given by

$$\mathfrak{R} = \frac{1}{2} [1 + K + (1 - K) \sin 3\theta] \quad (2.17)$$

where  $\theta$  is the Lode angle which is related to the third-invariant of the deviatoric stress tensor, and  $K = \text{TXE}/\text{TXC}$  limited to  $0.778 \leq K \leq 1.0$  to ensure a convex yield surface. Also shown in Figure 2-3 are the familiar Mises-Schleicher (MS) and Mohr-Coulomb (MC) failure surfaces. Note that the MS surface is obtained by fitting the model to TXC conditions and does not account for any reduced strength in TXE. MC, on the other hand, is defined by straight lines between TXE and TXC. Because some of the calculations performed by other DNA contractors (presented in Section 3) were performed using the Willam-Warnke (1975) function, it is also shown in Figure 2-3 to illustrate the differences between it and the failure surfaces just described.

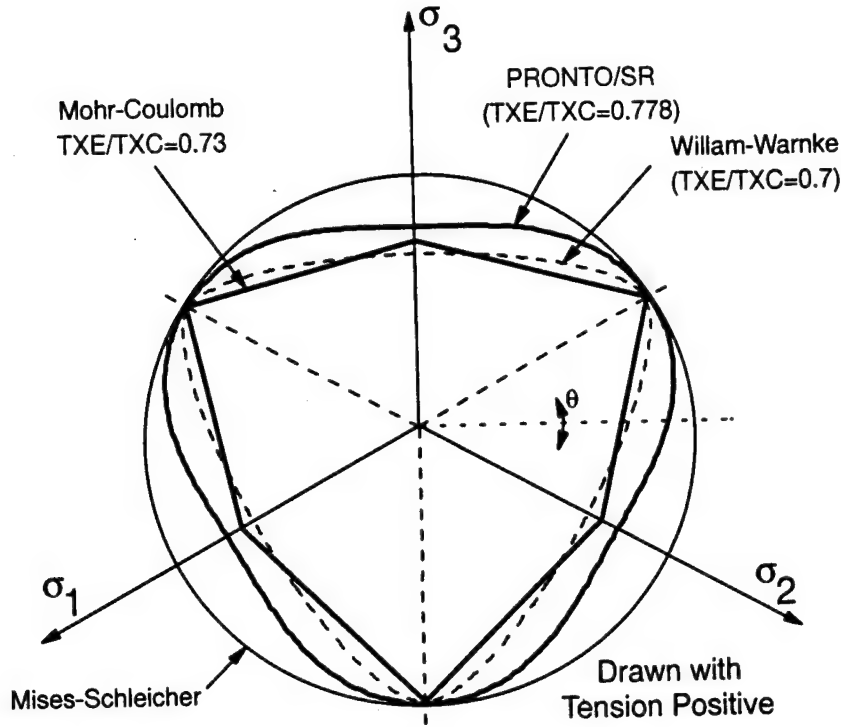


Figure 2-3. Yield surfaces in the  $\pi$ -plane.

It is well known that materials exhibit higher strengths when loaded at higher strain rates. Because shock-loaded tunnels involve strain-rates as high as  $10^4 \text{ sec}^{-1}$ , rate effects must be accounted for. Unfortunately, only a limited amount of data is available at these high strain-rates. Green and Perkins (1972) and others have measured a sharp increase (exponential) in strength for strain rates above about  $10^2 \text{ sec}^{-1}$ .

In the high compressive states associated with shock loadings, rock becomes an almost plastic material. Given the success of rate-independent cap models for representing this behavior, a number of researchers have used two approaches in developing viscoplastic versions of the cap model to represent rock under high loading rates. In the approach of Perzyna (1966), the viscoplastic strain rate is a function of the level of overstress and a fluidity parameter  $\lambda$ ,

$$\dot{\epsilon}_{ij}^p = \lambda (\phi(f)) \frac{\partial f}{\partial \sigma_{ij}} \quad (2.18)$$

In (2.18),  $\phi(f)$  can be chosen to match experimental data. In the Duvaut and Lions (1972) approach, the viscoplastic strain rate is a linear function of the overstress, and a material constant termed the relaxation time  $\tau$  that determines the rate at which the stress relaxes back to the inviscid solution. The Duvaut-Lions model is given by

$$\dot{\epsilon}_{ij}^p = \frac{1}{\tau} C_{ijkl}^{-1} (\sigma_{ij} - \bar{\sigma}_{ij}) \quad (2.19)$$

where  $C_{ijkl}$  is the elasticity tensor,  $\sigma_{ij}$  is the stress tensor and  $\bar{\sigma}_{ij}$  is the inviscid stress tensor. The Duvaut-Lions model is attractive because of its simplicity and ease of implementation.

**2.3.3.3 Limited Tension Algorithm.** A limited-tension algorithm developed by Callahan (1989) is used in the constitutive model to simulate tensile failure. In this algorithm the tensile strength at each integration point  $T_x$  is set initially to the intact tensile strength  $T_0$ . At each integration point at each time step, the principal stresses ( $\sigma_I \geq \sigma_{II} \geq \sigma_{III}$ ) and their unit direction vectors ( $n_I, n_{II}, n_{III}$ ) are calculated based on the trial stress state  $\sigma_{ij}^1$  at that location and time. Each principal stress component that exceeds the tensile strength at the integration point  $T_x$  is set to the residual tensile strength  $T_r$ . In addition, the tensile strength at the integration point is set to  $T_r$  if  $T_x$  is exceeded. (Recall that tension is negative according to the sign convention, so exceeding  $T_x$  implies that the stress is less than  $T_x$  and the stress is set to  $-T_r$ .) The resultant stress state is calculated by transforming the principal stress components back to the global coordinate system while maintaining the original principal stress directions. This transformation is accomplished according to the following equation:

$$\sigma_{ij} = n_{iI}n_{jI}\sigma_I + n_{iII}n_{jII}\sigma_{II} + n_{iIII}n_{jIII}\sigma_{III} \quad (2.20)$$

where  $n_{iI}$  is the  $i^{th}$  component of unit direction vector  $n_I$ .

**2.3.3.4 Implicit Rock Joint Modelling.** The compliant joint model (CJM) is a three-dimensional elastic model used to represent the mechanical response of a rock matrix with joints (Labreche and Petney, 1987). The model implemented in PRONTO2D is a two-dimensional version of the CJM. The CJM assumes that the deformation of a jointed rock mass is caused by the combination of the elastic response of the rock matrix and the elastic response of the joints. The unfractured rock matrix is modeled as an isotropic linear elastic solid and the joints as a nonlinear elastic layer. The model consists of up to four joint sets with various spacing and orientation. The response of the CJM is effectively anisotropic due to the presence of the joint sets.

The displacement behavior normal to the joint plane varies nonlinearly with stress and the response is governed by the physical characteristics such as joint aperture, roughness and contact between joint surfaces, strength of the wall rock, and presence or absence of filling. The response is also governed by the recent movement history of the rock joint. The aperture change of a well-mated joint without filling can be represented by a hyperbolic relationship between the stress normal to joint plane and the joint closure (Goodman, 1976; Bandis, *et al.*, 1983). The form used in the CJM is given by the equation

$$\sigma_n = a \left( \frac{v_n}{\delta + v_n} \right)^m \quad (2.21)$$

where,

- $\sigma_n$  - normal stress acting on the joint (compression positive)
- $a$  - half-closure stress (stress to reduce the aperture to  $\delta/2$ )

- $v_n$  - joint normal displacement (closure positive, zero when  $\sigma_n = 0$ )
- $\delta$  - maximum joint closure
- $m$  - exponent

The stiffness normal to the joint,  $k_n$ , is defined by

$$k_n = \frac{\partial \sigma_n}{\partial v_n} = am \frac{\delta v_n^{m-1}}{(\delta - v_n)^{m+1}} \quad (2.22)$$

which is the slope of the nonlinear joint closure. This hyperbolic function is used in the numerical formulation for the normal stress-displacement response when the normal stress is compressive. A constant value of  $10^{-4}$  times the dilatational modulus,  $\lambda - 2\mu$ , of the matrix is used for joint normal stiffness when the normal stress is tensile. This stiffness defines a linear, normal stress-normal displacement relationship for the joint in tension. This small but nonzero stiffness avoids numerical singularities in the computations. The transmission of small tensile stresses by elements having moduli four orders of magnitude lower than the matrix are accepted as insignificant relative to typical compressive stresses.

The compressive normal stress-displacement relation is nonlinear and elastic. Thus, there is no path dependence and all joint closure is fully recoverable in this model.

The shear response of joints generally consists of a nearly linear rise to peak shear strength, followed by softening behavior with continuing shear. However, it is acknowledged that joint size dependence may alter this. The peak shear strength response of joints is supported by studies such as Goodman (1976) and Bandis (1983). The shear stress of joints is known to be inelastic when the stress state approaches the peak shear strength. The CJM only models the elastic joint shear response. The shear stiffness, which is independent of the normal stiffness across the joint, relates the shear displacement to shear stress.

$$\tau = k_s v_t \quad (2.23)$$

where,

- $\tau$  - shear strength
- $k_s$  - joint shear stiffness
- $v_t$  - joint displacement tangent to plane of joint

The shear stiffness is defined by

$$k_s = \frac{\partial \tau}{\partial v_t} \quad (2.24)$$

The CJM introduces anisotropy by reducing the composite modulus of the modeled rock mass in the direction normal to the joint in an otherwise linear elastic material. Computation of effective moduli is used to implement the softening effects of the joints. Stress equilibrium is the underlying assumption in the combined response of the rock matrix and the joint sets. The normal stress across the joint is equal to the stress in the rock matrix normal to the joint plane. The shear stress on the joint is equal to the shear stress in the rock matrix parallel to the joint plane.

Correspondingly, the strains in the rock matrix are combined with the strains in the joints additively. That is, the effective compliance for the rock mass is the sum of the compliances of the unfractured rock and the joint sets. The effective Young's modulus,  $\hat{E}$ , normal to a joint and the effective shear modulus,  $\hat{G}$ , parallel to a joint, are

$$\begin{aligned}\frac{1}{\hat{E}} &= \frac{1}{E} + \frac{1}{k_n s} \\ \frac{1}{\hat{G}} &= \frac{1}{G} + \frac{1}{k_s s}\end{aligned}\tag{2.25}$$

where  $E$  and  $G$  are the elastic moduli of the rock matrix,  $k_n$  and  $k_s$  are the normal and shear stiffness of the joint set, and  $s$  is the spacing of the joints in the joint set.

**2.3.3.5 Explicit Rock Joint Modelling.** PRONTO treats contact as a kinematic constraint. That is, the algorithm modifies the accelerations of the nodes along the contact region such that the kinematic constraints are satisfied. The algorithm uses a partitioned approach to enforce compliance between two contact surfaces by allowing each surface to act as a master surface for a fraction of each time step and a slave for the remainder.

There are four steps involved in the contact algorithm. First, the contact surface geometry is recalculated at each time step and the predicted configuration is computed by integrating the motion without regard to the kinematic constraints required by the contact surfaces. The following quantities are calculated for each node:

$$\begin{aligned}\hat{a} &= f/m \\ \hat{v} &= v + \Delta t \hat{a} \\ \hat{x} &= x + \Delta t \hat{v}\end{aligned}\tag{2.26}$$

Where  $f$  is the residual force vector (sum of external forces minus the sum of internal forces),  $m$  is the nodal mass,  $v$ , is the current velocity, and  $\Delta t$  is the time increment. The predicted kinematic quantities are denoted by the hat.



The second step is surface tracking, or the process of matching nodes along one surface with the mating surface. The algorithm used is to locate the spatially nearest master node to the possible point of contact. This procedure can be the most time consuming portion of the analysis for this type of problem. To streamline the tracking algorithm, the nearest master node to a given slave node at one time step is assumed to be in the vicinity of the nearest master node at the next time step. Therefore, at each time step, the nearest master node is the starting point for the search along the surface.

The next step is to determine contact or penetration. The slave node is oriented with respect to the master segments connected to the tracked master node. The depth and position coordinates are calculated for both master segments connected to the nearest master node. From these quantities, if the depth is positive, the slave node is penetrating the segment and if the position is positive then the slave node is along the segment. When the master surface forms an outside corner, there may be penetration of both segments. In this case, the algorithm determines with which master segment the slave surface is more strongly in contact. One limitation of the algorithm is that it can not detect a contact surface contacting itself.

The final step in the contact algorithm is to calculate the penetration forces imposed on the master surface by the slave surface to restore kinematic compliance. These forces are calculated as a fraction of the forces that would be imposed by the slave nodes if the master surface was rigid. This fraction is based on the fraction of each time step for which the surfaces act as master and slave. The roles are reversed for the remaining fraction of the time step. The accelerations are calculated to predict the response of the master surface to these penetration forces such that the response of each contacting slave node is constrained by its master nodes. The principle of virtual work is employed to define the accelerations of the master nodes in response to the penetration forces. When friction is present, the relative tangential motion of the contacting slave nodes is resisted. The magnitude of the tangential force exerted on the master surface on a slave node cannot exceed the friction force. Thus friction adds a tangential acceleration to the nodes in contact.

#### 2.3.4 Transmitting Boundary Conditions.

A transmitting boundary is used to simulate a semi-infinite domain outside the boundary, where the wave speeds of the material on both sides of the boundary are the same. The region exterior to the boundary is replaced with an energy-absorbing boundary condition that behaves as if the energy is transmitted across the boundary. Thus, no energy is reflected back into the interior region.

The nonreflecting boundary is implemented in PRONTO according to a technique proposed by Lysmer (Lysmer and Kuhlemeyer, 1979). The basic idea is to apply tractions at the boundary that will exactly cancel the stresses that would be reflected from a free surface. Hence, the

numerical technique involves calculating and applying the following tractions to the surface of the nonreflecting boundary

$$\begin{aligned}\sigma_n &= \rho V_p \dot{u}_n \\ \tau_t &= -\rho V_s \dot{u}_t\end{aligned}\tag{2.27}$$

where  $\sigma_n$  and  $\tau_t$  are the normal and shear tractions;  $\rho$ ,  $V_p$ , and  $V_s$  are the current density, compressional wave speed, and shear wave speed of the material along the boundary; and  $\dot{u}_n$  and  $\dot{u}_t$  are the normal and tangential components of the current velocity at the boundary. At each time step, PRONTO updates the tractions at the boundary using the current density and effective dilatational and shear moduli in each element along the boundary.

In calculating the current wave speeds, PRONTO assumes that the wave speeds are isotropic and independent of the orientation of the boundary. Obviously, the joint sets in a rock mass yield an anisotropic medium in which the wave speeds depend on the incident direction. However, the anisotropy inherent in the CJM is not accounted for in the wave speed calculation in PRONTO. Consequently, the wave speeds used to calculate the tractions along the nonreflecting boundary are somewhat in error, the magnitude of which depends on the orientation of the boundary with respect to the principal directions of the anisotropy. This error results in a partial reflection of the incident stress.

## SECTION 3

### VERIFICATION AND VALIDATION OF DETERMINISTIC TUNNEL MODELS

#### 3.1 INTRODUCTION.

The quality of probabilistic predictions is highly dependent on the quality of the underlying deterministic model. For complex problems that have no analytical solution, the quality of the deterministic model can be measured qualitatively in terms of confidence gained by applying the model and comparing predicted results with test measurements for a variety of different configurations and loadings.

The process of obtaining confidence in the deterministic model can be termed verification and validation. Verification involves comparing predictions to either known solutions, or comparing predictions that have no known solution to independently made predictions using other methods. While the former is preferable, comparing to independently obtained solutions can be an effective way to augment the suite of verification problems. When a numerical model is said to be verified, it is assumed to be working as intended and be free from errors, bugs, and numerical inaccuracies.

The process of validating a numerical model involves comparing predictions made using the numerical model with experimental results. The process is much more difficult than verification, and in reality, can never be achieved completely. However, a model is usually accepted as being validated if it has been demonstrated to be able to predict all significant physical processes observed and measured in a similar test.

To establish confidence in the numerical models, SwRI participated in two large verification and validation programs, which are summarized in the following sections. The Benchmark Activity described in Section 3.2 focuses primarily on model verification and the Precision Test Modeling program described in Section 3.3 is concerned with model validation. Both of these models are then integrated with the probabilistic methods described in Section 4 and applied to several DNA selected problems in Section 5.

#### 3.2 BENCHMARK ACTIVITY.

The goal of the benchmark activity was to show the influence of calculational approach on the predicted response of a circular tunnel in a jointed rock mass subjected to ground shock loading. The benchmark problems were artificial problems that tested the modeling capabilities and limitations of the finite element and distinct element computer codes used by the participants. The final benchmark calculation was preceded by several preliminary calculations based on simpler but related problems. The common element in the calculations was the geometric and material description of the joints and intact rock. All but two of the problems solved had analytical solutions to compare calculational results to.

The participants in the Benchmark Activity were RE/SPEC (under subcontract to SwRI), R & D Associates (RDA), California Research and Technology (CRT, and now TRT), Weidlinger

Associates (WA), Itasca, and Lawrence Livermore National Laboratory (LLNL). The benchmark activity has been well documented, so only a brief summary will be presented in here. More information can be found in Simons (1993), Senseny and Simons (1994), and Osnes (1991).

To summarize the effort, several bugs and modeling errors were discovered and resolved by all of the participants during the course of working through the benchmark problems. The results for the final problem, which involved a deep tunnel in an explicitly-jointed rock mass subjected to stress wave loading, three of the participants (CRT, WA and Itasca) obtained (remarkably) similar tunnel deformation results. Using PRONTO, RE/SPEC obtained tunnel closures that were substantially higher than the "consensus" answer. It is believed that the larger deformations were due to the explicit joint modeling approach described in Section 2. However, because an analytical solution is not available combined with the fact that PRONTO performed extremely well on all of the other benchmark problems, some question remains as to which answer is actually correct.

### 3.3 PRECISION TEST MODELING.

#### 3.3.1 Static Tunnel Tests in Limestone.

In many model validation efforts, predictive models are simply "calibrated" to agree with experimental results. This is true both for constitutive models calibrated to laboratory data and for structural response models calibrated to structure test data. Because of this practice, the fidelity of the model is unknown when used to predict behavior of real-world problems. This necessarily reduces the confidence one should have in predictions made using calibrated models.

One way to assess the fidelity of a predictive model is to apply the model to a non-trivial laboratory problem that is representative of the real-world problem without any prior knowledge of the test results, and then critically assess the performance of the model against the experimental results. This approach is the one being taken in the Precision Test Modeling (PTM) program sponsored by the DNA. The goals of PTM are to reveal if and where more research and development is needed, explore the influence of computational approaches on the outcome of the numerical simulations, and identify where modeling approaches differed and the relevance of those differences. The motivation for such an effort is to validate the ability of current state-of-the-art predictive models to simulate real-world problems. The PTM program consists of laboratory material tests, small-scale structure tests, and numerical predictions. Only the numerical predictions are summarized here.

The PTM participants were: Schwer Engineering & Consulting Services (SE&CS under subcontract to Aptek), Southwest Research Institute (SwRI), Titan Research and Technology (TRT), and Weidlinger Associates (WA). The static and dynamic tunnel tests were performed by SRI (Simons, *et. al.*, 1993).

In the next two sections, the static and dynamic tests are described and the material property data used in the exercise tabulated. Next, the calculational methods and constitutive models used in the analysis are described followed by comparisons between calculations and experiments.

Finally, some interpretation from the comparisons and recommendations for further research are given.

**3.3.1.1 Description of Static Tests.** The static tests consisted of cylindrical test specimens containing lined and unlined tunnels. Several load paths were tested, and pressures, strains and tunnel deformations recorded. From the suite of tests, three were selected for analysis in the PTM program, herein referred to as ST1, ST2, and ST3. The general configuration is shown in Figure 3-1. The test specimens were all 30.5 cm diameter cylinders taken from a single block of Salem limestone. The specimen used in ST1 was 30.5 cm high with a 1.91 cm unlined tunnel spanning the diameter of the specimen at midheight. The ST2 and ST3 tests both used cylinders that were 45.7 cm high (to reduce end effects) with a lined tunnel also spanning the diameter of the specimen at midheight. The liners were fully annealed 3003 aluminum tubes with an inside diameter of 18.6 mm and a wall thickness of 0.89 mm.

The ST1 test subjected the unlined tunnel to a single uniaxial strain load-unload cycle. In ST2, the lined tunnel was also loaded in uniaxial strain, but two load-unload cycles were performed. The uniaxial strain path is of interest because it is similar to the loading on underground structures from detonations above ground level. In ST3, the loading approximated a spherically-divergent strain path similar to that from a spherical wave propagated by an explosion at or below ground level. The ST1, ST2 and ST3 loadings are shown in Figure 3-2 (described in subsequent sections).

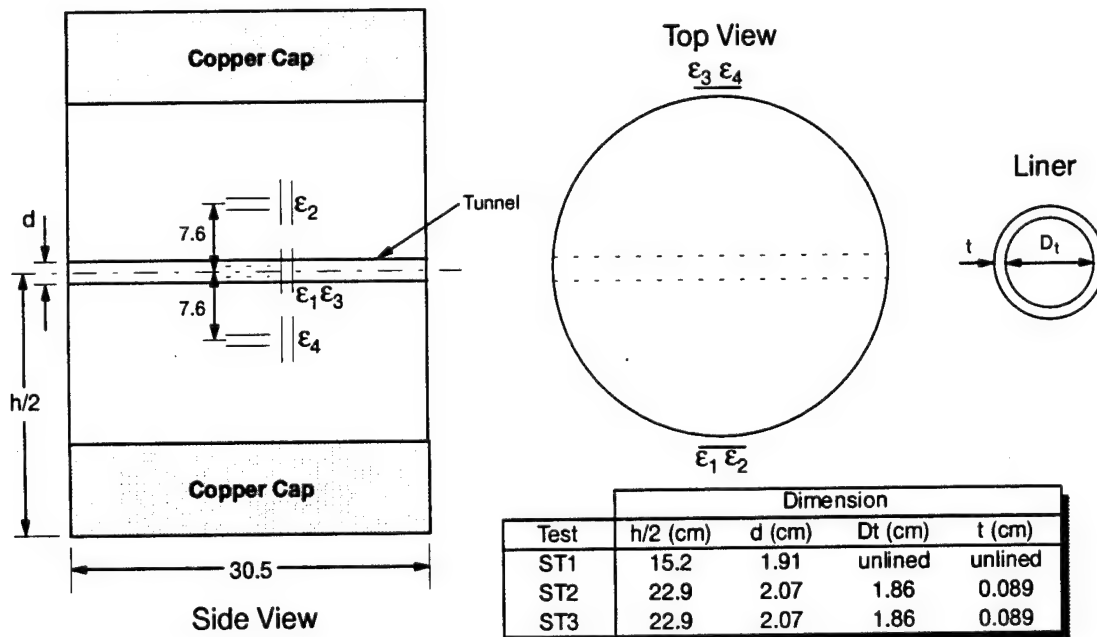


Figure 3-1. SRII static test configuration.

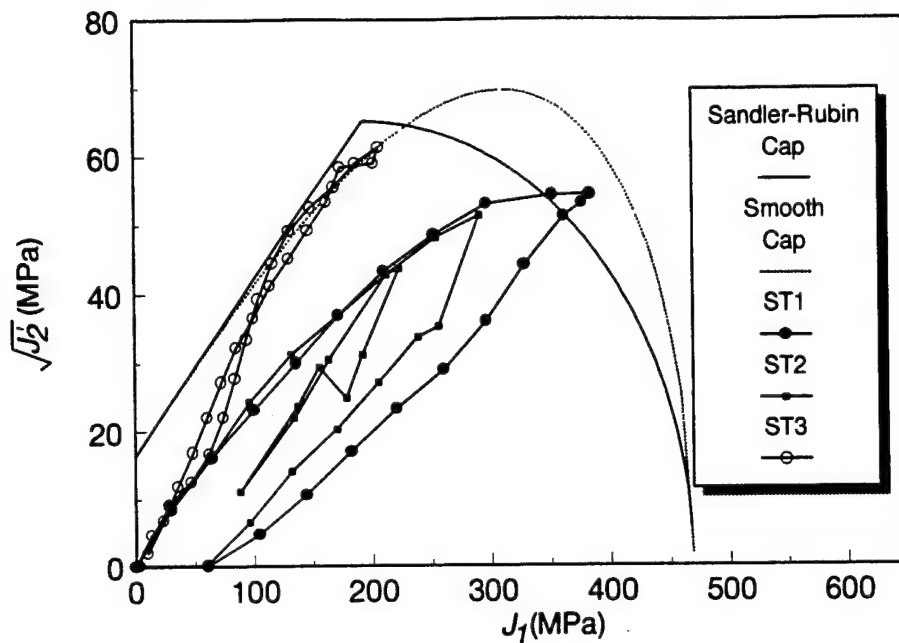


Figure 3-2. Sandler-Rubin cap model. Also shown are the load paths from the SRI static tunnel tests and the smooth cap model.

**3.3.1.2 Material Properties.** A significant amount of test data for Salem limestone has been amassed by several laboratories working independently (ARA, SRI and RE/SPEC Inc.). RE/SPEC was tasked with performing specific tests needed to characterize the parameters in the Sandler-Rubin cap model; thus, the PTM participants were directed to use the RE/SPEC data (Fossum, *et. al.*, 1995) for the cap model parameters. RE/SPEC performed a large number of hydrostatic compression, triaxial compression and uniaxial strain tests on Salem limestone samples taken from the same blocks SRI used to construct the static and dynamic specimens. RE/SPEC performed two different fits to their data. The first, denoted RE/SPEC-93, was provided to the PTM participants at the start of the PTM program. The second fit, denoted RE/SPEC-94, included lateral strain measurements and ultimate shear data, presumably to improve the fit. The RE/SPEC-93 data was used for this study because the RESPEC-94 data was not available until late in the program. For completeness, Table 3-1 lists both sets of properties.

The lined static and dynamic tunnel tests used aluminum liners. From pressure tests performed on the liners, SRI measured Young's modulus and Poisson's ratio to be 75.9 GPa and 0.28 respectively. Since significant inelastic deformation on the liners is expected in the tunnel tests, SRI also measured and reported the effective stress-effective strain response of the aluminum. The experimental and predicted stress-strain curves are shown in Figure 3-3.

Table 3-1. Sandler-Rubin cap model properties for Salem limestone.			
Parameter	Description	RE/SPEC-93	RE/SPEC-94
$K$ (MPa)	Bulk Modulus	15725	16214
$G$ (MPa)	Shear Modulus	9112	9531
$A$ (MPa)	Failure Surface Parameter	689.5	199.43
$B$ (MPa <sup>-1</sup> )	Failure Surface Parameter	3.9e-4	1.922e-3
$C$ (MPa)	Failure Surface Parameter	673.2	185.77
$D$ (MPa <sup>-1</sup> )	Hardening Parameter	1.44e-3	8.616e-4
$W$	Hardening Parameter	0.08266	0.108
$R$	Cap Shape Parameter	4.215	5.63
$X_o(L_o)$ (MPa)	Cap Location Parameter	-468.1 (-193.323)	-441.26 (-131.217)

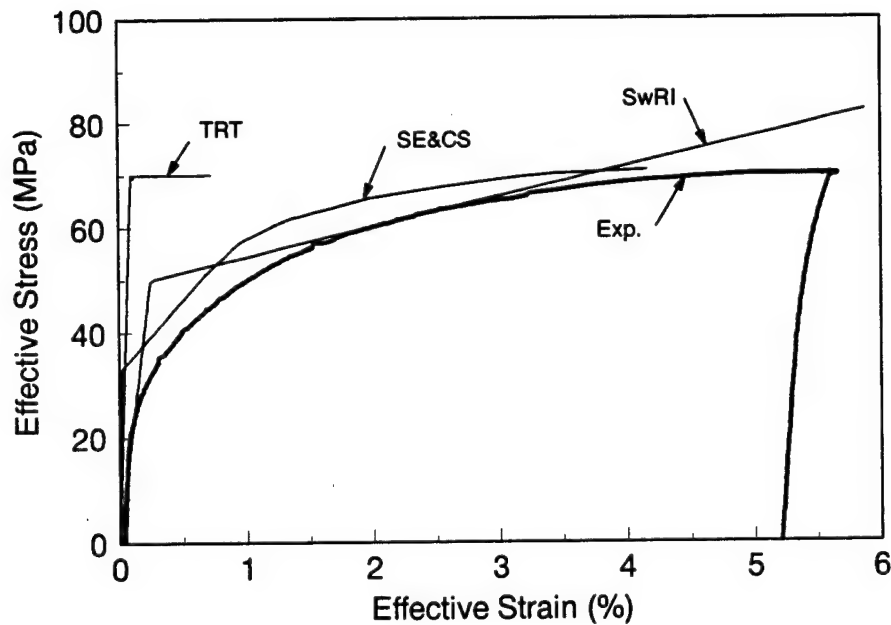


Figure 3-3. Comparison of experimental and predicted aluminum liner response.

**3.3.1.3 Calculations.** Various finite element discretizations were used to model the static tunnel tests. SwRI and WA used full three-dimensional 1/8 symmetry models. TRT and SE&CS used "slab" models, which neglected the outer curvature of the cylinder. Since the tunnel responses of interest were at the center of the cylinder, the error in neglecting the outer curvature was believed to be small. For ST2 and ST3, frictionless contact was assumed between the liner and the rock.

Responses compared included axial and circumferential strains at  $\epsilon_1$  and  $\epsilon_2$  (see Figure 3-1) and springline and crown-invert tunnel closures.

All four calculators obtained static solutions using their dynamic codes: SE&CS, SwRI and TRT applied the loading at a very slow rate (quasi-static), and WA used dynamic relaxation. The calculations were initially performed using a two-invariant cap model, and comparisons between calculators made. Since all except SE&CS used exactly the same two-invariant model, this allowed a consensus check to be made before employing three-invariant models. The quasi-static simulation time varied by calculator; SwRI used 20 ms.

**3.3.1.4 Results and Discussion.** Predicted closures from the ST1 static tunnel simulations are shown in Figures 3-4 and 3-5. Using the two-invariant models (Figures 3-4a and 3-4b), relatively good agreement between participants is seen for crown-invert and springline closures. The fact that SwRI, TRT and WA obtained similar results is because they used the same two-invariant model. SE&CS, on the other hand, used a different model (see Figure 3-2) and obtained different results. Comparisons between experiment and predictions in Figures 3-4a and 3-4b show considerable disagreement. The crown-invert closures are about 2%-3% higher than experimental and the springline closures are about 13% lower than experimental.

In an attempt to improve the closure predictions, three-invariant yield surface models were employed. The results are shown in Figures 3-4b and 3-5b. As seen, the desired effect was obtained — the springline closures increased. However, the scatter in the predictions also increased. Since WA and TRT results compare very well, and also since they both used the same three-invariant model, the scatter between all participants appears to be due to the use of different 3-invariant models. This indicates that closure, or more generally structure behavior, is very sensitive to the shape of the yield surface.

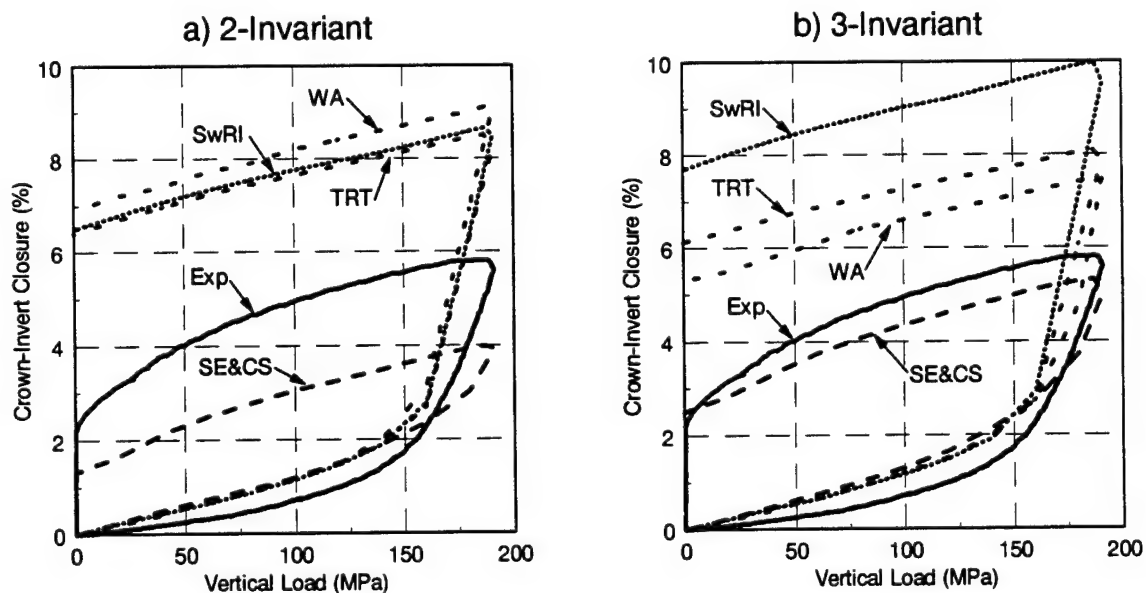


Figure 3-4. ST1 Crown-invert closures: a) 2-invariant, b) 3-invariant.



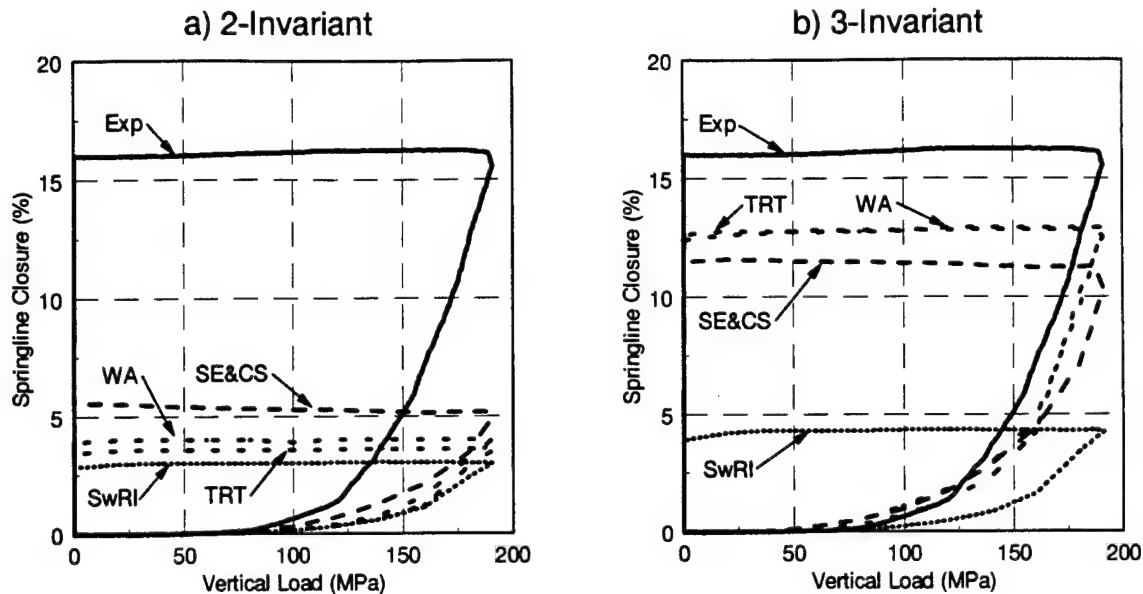


Figure 3-5. ST1 Springline closures: a) 2-invariant, b) 3-invariant.

Results for the ST2 and ST3 tests, both of which include liners, are shown in Figures 3-6 to 3-9. Figure 3-6a shows good agreement between the predictions and the experimental results. The effect of including the third-invariant was small as shown in Figure 3-6b. It is interesting to note that SE&CS predicted very little recovery during unloading (nearly horizontal lines), which closely resembles the test data. None of the other participants predicted this. Explanations for this were postulated to be due to different liner constitutive models and/or closures being measured on the rock versus the liner. Side studies performed by the participants did not support these theories; thus, other factors may be to blame, such as the use of continuum vs shell elements to model the liner.

Springline closures for ST2, unlike the crown-invert, showed much larger variation in prediction when the third-invariant was included. As seen from Figure 3-7a, predictions made using a two-invariant model were in reasonable agreement with experimental results. The inclusion of the third-invariant had the same overall effect that it did for ST1 — springline closures were much larger and the scatter between predictions increased. Again, this scatter is due to the use of different three-invariant models.

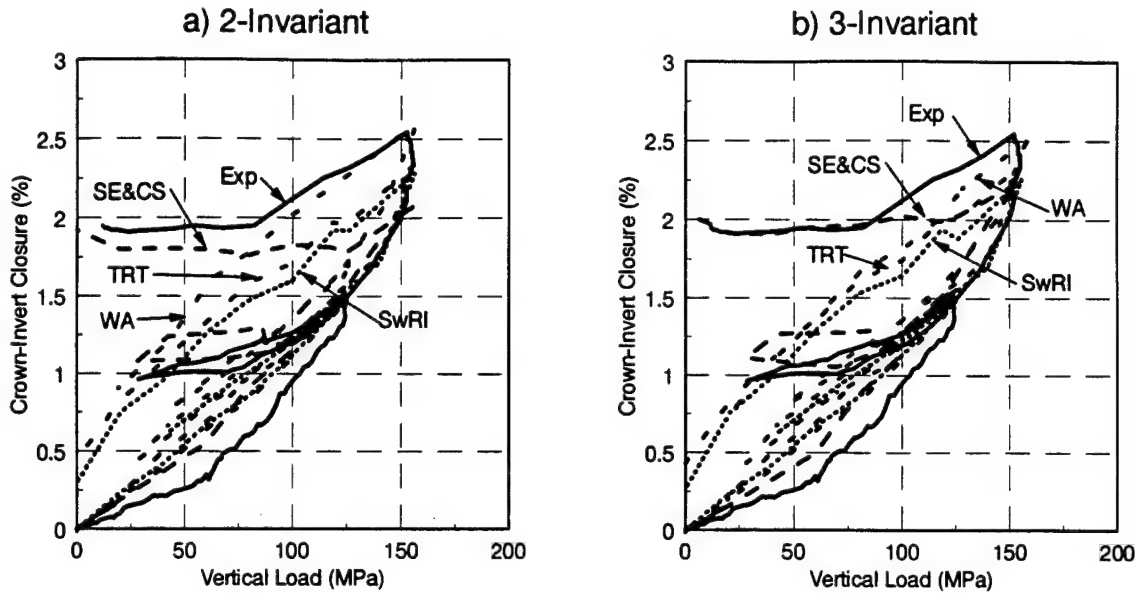


Figure 3-6. ST2 Crown-invert closures: a) 2-invariant, b) 3-invariant.

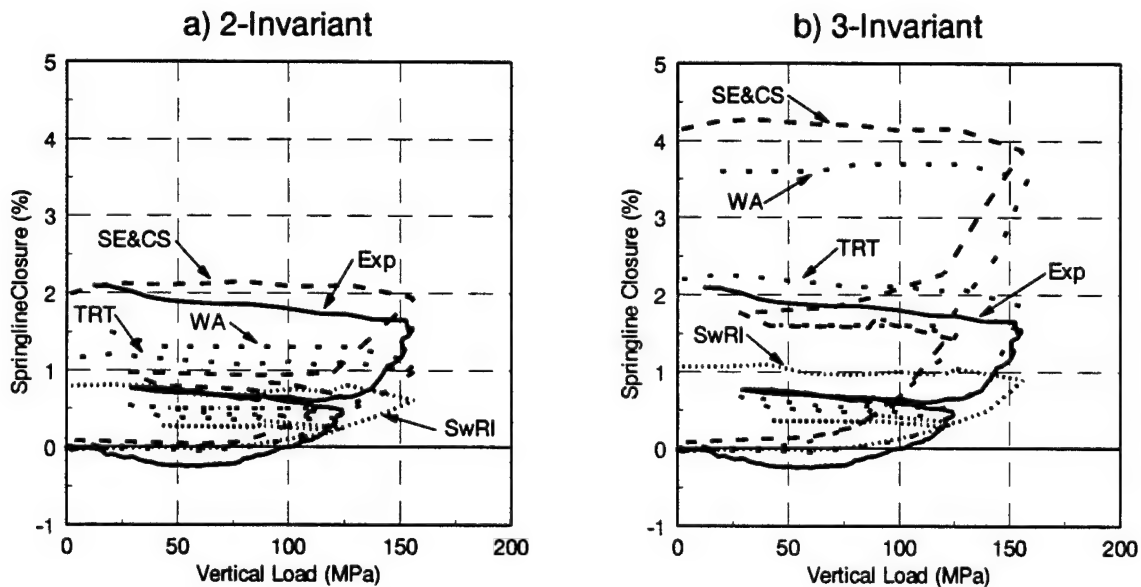


Figure 3-7. ST2 Springline closures: a) 2-invariant, b) 3-invariant.

Crown-invert and springline closures for ST3 are shown in Figures 3-8 and 3-9 respectively. Two-invariant models greatly underpredict both the crown-invert and springline closures. Similar to ST1 and ST2, the crown-invert closure was relatively unaffected while the springline closures generally increased upon inclusion of the third invariant. SE&CS's closure results grew very large because their calculation predicted that stresses in the free-field (i.e., the entire

specimen) reached the failure surface. That this is the case can be seen in Figure 3-2, where the ST3 load path contacts the Smooth Cap (SM) cap failure surface. Their closure results, however, should be simply taken as qualitatively "large" since complete closure and specimen failure will occur due to the fact that the failure surface is perfectly plastic. The fact that the ST3 load path comes *very* near to the Sandler-Rubin (SR) failure surface indicates that SwRI's, TRT's and WA's closures may be very sensitive to small changes in input parameters.

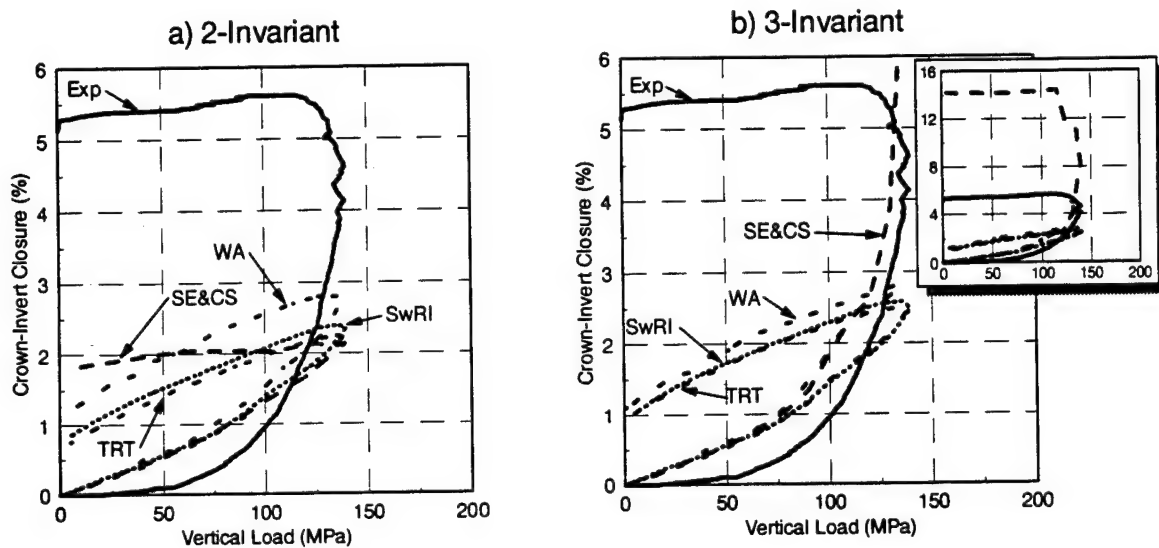


Figure 3-8. ST3 Crown-invert closures: a) 2-invariant, b) 3-invariant.

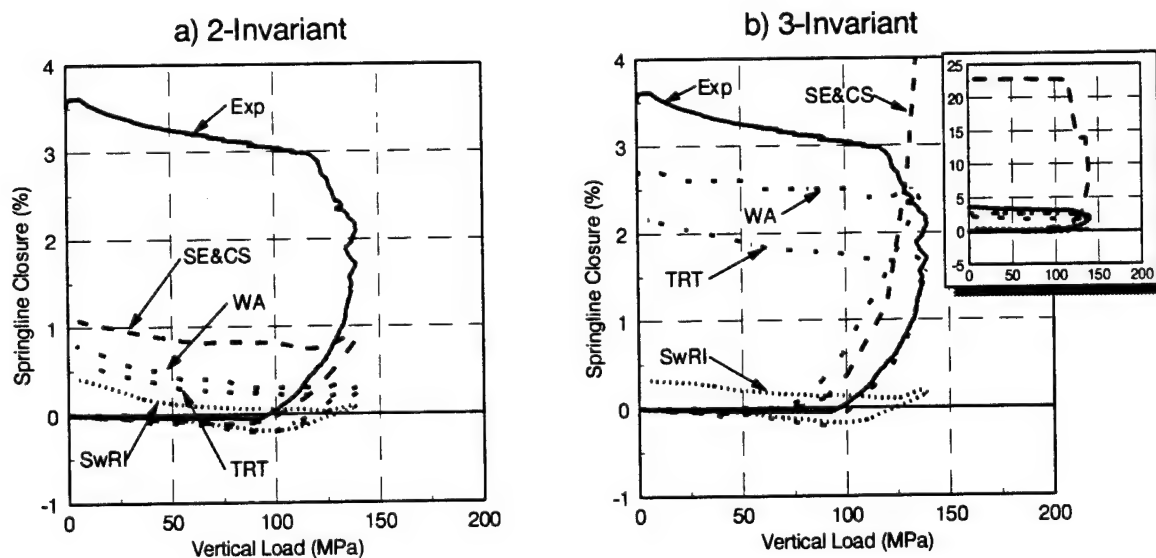


Figure 3-9. ST3 Springline closures: a) 2-invariant, b) 3-invariant.

Also worthy of note is the fact that in no case was the initial slope of the closure-load curve predicted well by the models. At both the crown-invert and springline location, the closures are overpredicted by the models. Although including the third-invariant did increase the final closure, it had little effect on the initial closures. This suggests that material property data may be incorrect, or other mechanisms not included in the models may be involved, such as hardening.

Two observations are made based on the static tunnel simulations:

1. Load-control quasi-static problems can be extremely sensitive to small changes in the material model or other inputs. Close attention has to be paid to loading rate and mesh discretization.
2. Static problems are useful for verifying dynamic response computer models, but they can be highly-sensitive to small changes in material parameters, and can introduce additional error if true quasi-static conditions are not achieved.

### 3.3.2 Dynamic Tunnel Tests in Limestone.

**3.3.2.1 Description of Dynamic (SWAT-II) Tests.** In the spherical wave tunnel (SWAT) test under consideration, a spherical explosive charge was detonated in a block of limestone containing five tunnels. Recorded data from the experiment included particle velocities and stress histories at several locations, and post-test tunnel deformations. The general configuration is shown in Figure 3-10. The specimen is an octagonal block of limestone  $1.2 \times 1.2 \times 1.67$  m with a 111-g spherical charge of pentaerythritol tetranitrate (PETN) at the center of the block. The two tunnels selected for analysis were both lined and located at distances of 14.5 cm and 19.2 cm from the center of the PETN charge. The tunnels were of the same diameter and liner material as those in the static tests. Stress and particle velocity gages were located as indicated in Figure 3-10.

Calibration to test data is required to determine either the modified material properties used by TRT or the Duvaut-Lions relaxation parameter  $\tau$  used by SE&CS and SwRI. Two approaches were taken: 1) fitting to an "average" strength increase of 40%, and 2) fitting to the SWAT-II free-field velocity or stress measurements. The 40% "average" strength increase was taken from limited testing performed by ARA on Salem limestone. For the remainder of this report, the first approach will be referred to as "uncalibrated" and the second approach as "calibrated." The term "calibrated" is used because a portion of the SWAT-II experiment (free-field response) is used to predict the tunnel behavior, i.e., the predictions using "calibrated" viscoplastic models were not made completely independent from the test data. The values for  $\tau$  estimated by SE&CS and SwRI are given in Table 3-2.

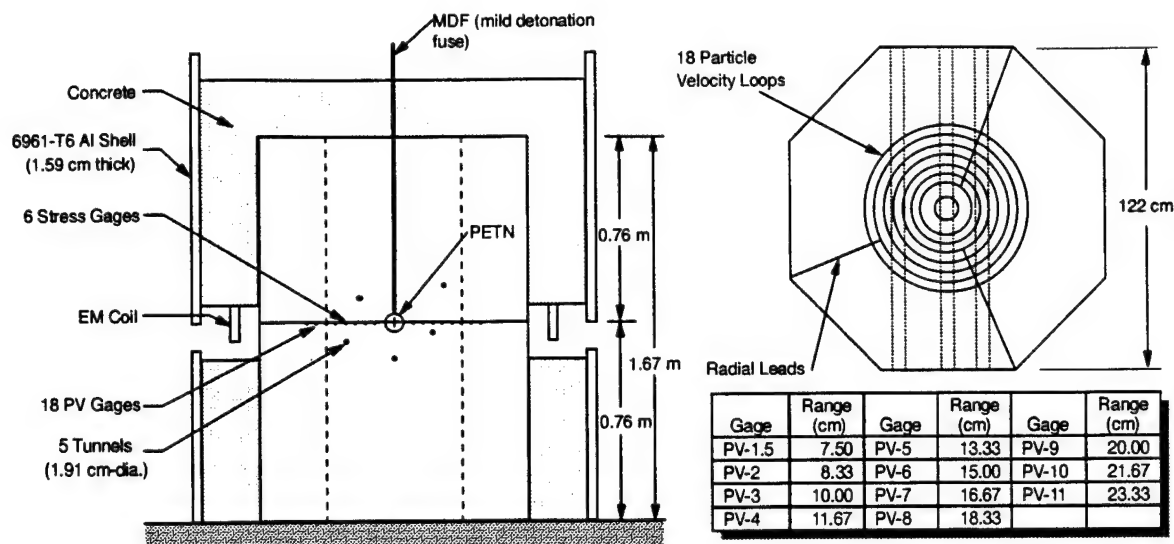


Figure 3-10. SWAT-II test configuration.

Table 3-2. Duvaut-Lions viscoplastic parameter values.		
Relaxation Parameter $\tau$		
Participant	Calibrated	Uncalibrated
SE&CS	5.e-6	5.e-6
SwRI	6.e-6	12.e-6

**3.3.2.2 Calculations.** As in the static tests, various finite element meshes were used to model the dynamic tunnel test. SE&CS and WA used full three-dimensional models. SwRI, while originally using a full three-dimensional model, eventually switched to a "wedge" mesh to reduce the number of elements and speed up the calculations, shown in Figure 3-11. TRT also used a wedge-shaped grid. Frictionless contact was assumed between the liner and the rock.

Mesh refinement studies were performed by the participants. Consensus reached was that at least five rings of 32 elements around the circumference of the tunnel were required to adequately model the complex tunnel wall deformations and stress gradients. Beyond this, each participant was free to mesh the remainder of the model.

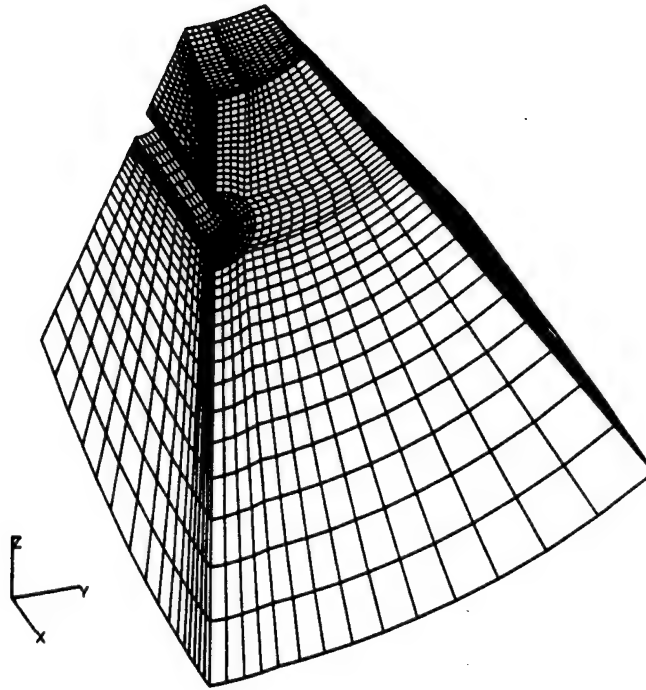


Figure 3-11. SwRI SWAT-II wedge mesh.

In Figure 3-10, the charge cavity radius is 7.5 cm, which is the location of the PV-1 velocity gage. Thus, the detonation of the PETN was not simulated in the calculations. Instead the recorded velocity transient at PV-1 is used as the driver for the calculations.

Responses from the calculation include velocities and stresses at the gage locations, and springline and crown-invert tunnel closures. The free-field (no-tunnel) environment was computed first to facilitate comparison between calculators, and to compare with the free-field measurements taken in the experiment. The simulation time is  $250\mu s$ .

**3.3.2.3 Results and Discussion.** Predictions of free-field velocities were computed and compared at gage locations PV-2, 5, 8 and 11. Using rate-independent models, the predictions agree with each other and with experimental results very well. The only exception is that from PV-5 through PV-11 the predicted peak velocity is truncated. However, the time-of-arrival, loading slope, positive phase and negative phase all agree quite well. Employing rate models, SE&CS, SwRI and TRT were able to improve the correlation with test data. The same general conclusions can be made with stresses, which were computed and compared at  $R=14.5$  (see Figures 3-12 and 3-13) and 19.2 cm. In general, the free-field velocities and stresses were found to be much less sensitive to the material model than the static test cases.

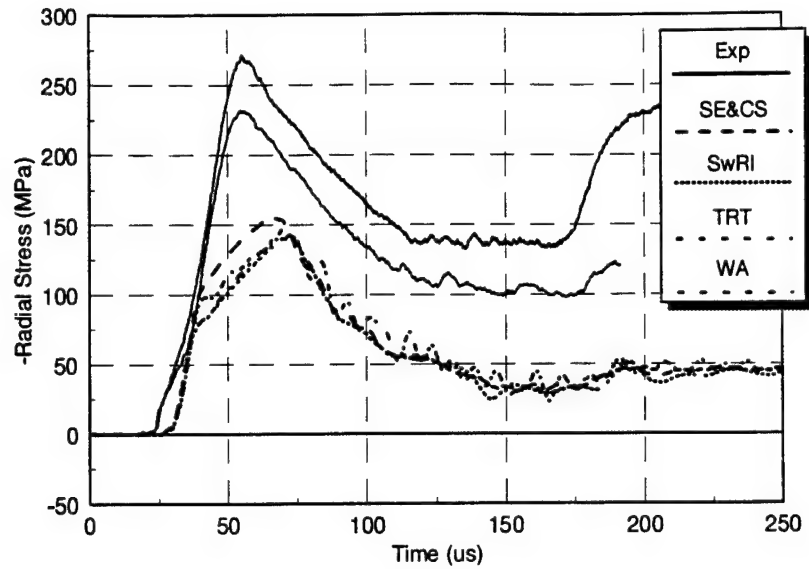


Figure 3-12. Free-field radial stresses at  $R=14.5\text{cm}$ . Predictions based on rate-independent model.

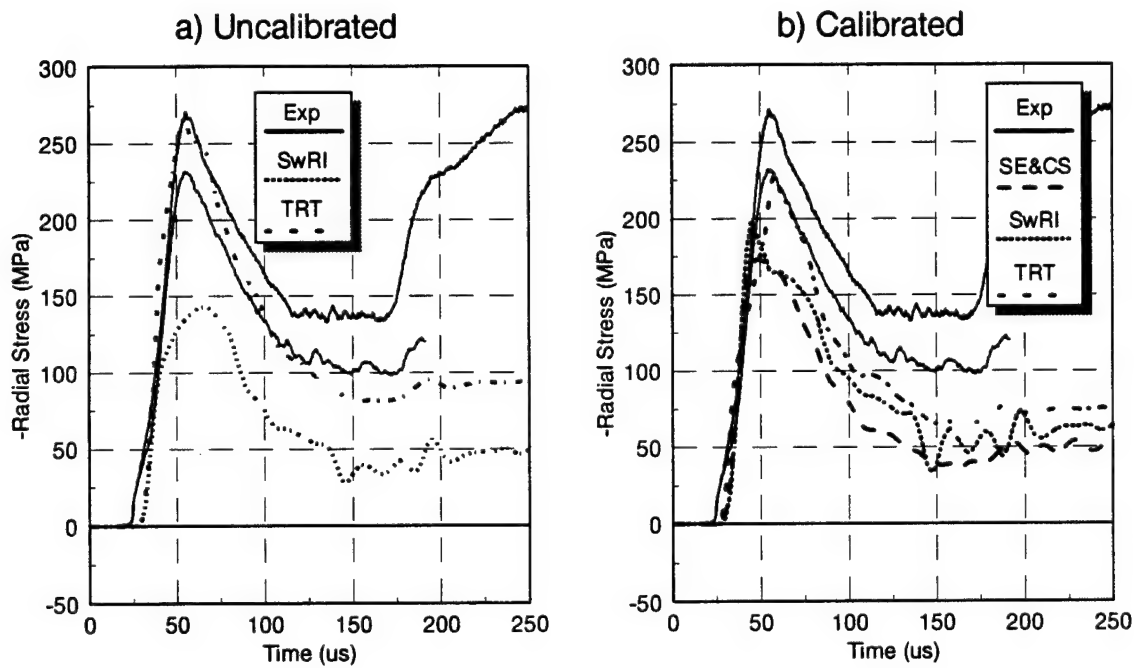


Figure 3-13. Free-field radial stresses at  $R=14.5\text{cm}$ . Predictions based on rate-dependent models:  
a) uncalibrated, b) calibrated.

While rate-dependent models did introduce additional scatter in the predicted results, this was outweighed by the much better correlation with test data. As will be discussed in the following, this was not generally the case with tunnel closures.

Tunnel closures for the R=14.5 cm and R=19.2 cm tunnel are shown in Figures 3-14 to 3-17. For the R=14.5 cm tunnel, the rate-independent models were in rough agreement (within 2%) with experimental data at the crown-invert, and although to a lesser degree, also at the springline. Except for SwRI's results, which agreed with experimental results, the rate-independent models underpredicted crown-invert closure and agreed fairly well at the springline for the R=19.2 cm tunnel.

Both SE&CS and SwRI saw very little change in their crown-invert closure predictions when rate-dependence was included for both the R=14.5 cm and 19.2 cm tunnels. However, springline closures changed dramatically. The inclusion of rate-dependence changed SE&CS' and SwRI's closures from 2.5% to -1.5% for the R=14.5 cm tunnel and from 1% to -1% for the R=19.2 cm tunnel. These predictions actually agree with the experimental (negative) closures during early times (i.e., springline openture is measured). Unlike the rate-dependent predictions, however, the experimental springline opentures quickly reverse and become closure. Using their rate-dependent model, TRT predicted higher closures at both the crown-invert and springline locations for both tunnels.

SwRI's and TRT's results for "uncalibrated" and "calibrated" rate-dependent models are also shown in Figures 3-14b to 3-17b. As expected, predictions made using calibrated rate models were closer to experimental results; however, the overall quality of the prediction is not improved by much.

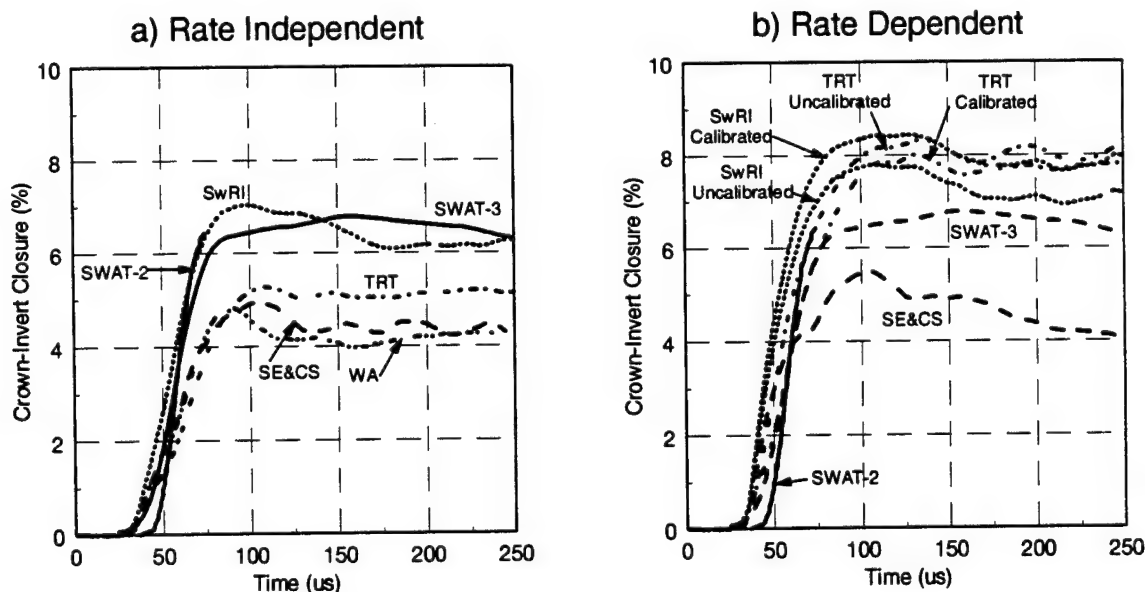


Figure 3-14. SWAT-II crown-invert closures for R=14.5 cm tunnel: a) rate-independent, b) rate-dependent.



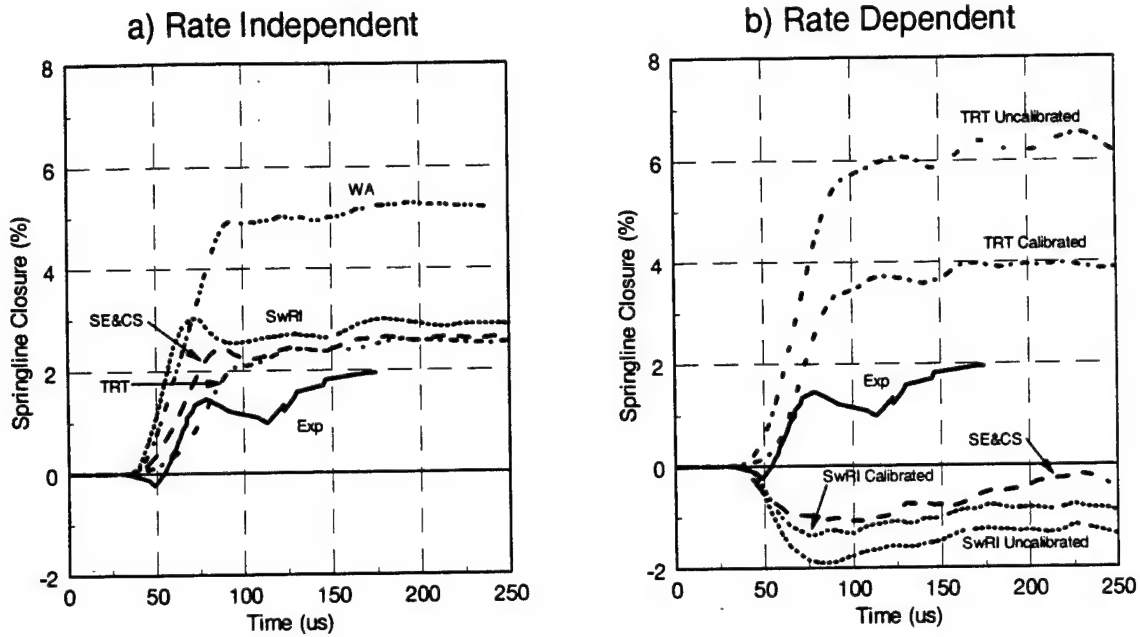


Figure 3-15. SWAT-II springline closures for R=14.5 cm tunnel: a) rate-independent, b) rate-dependent.

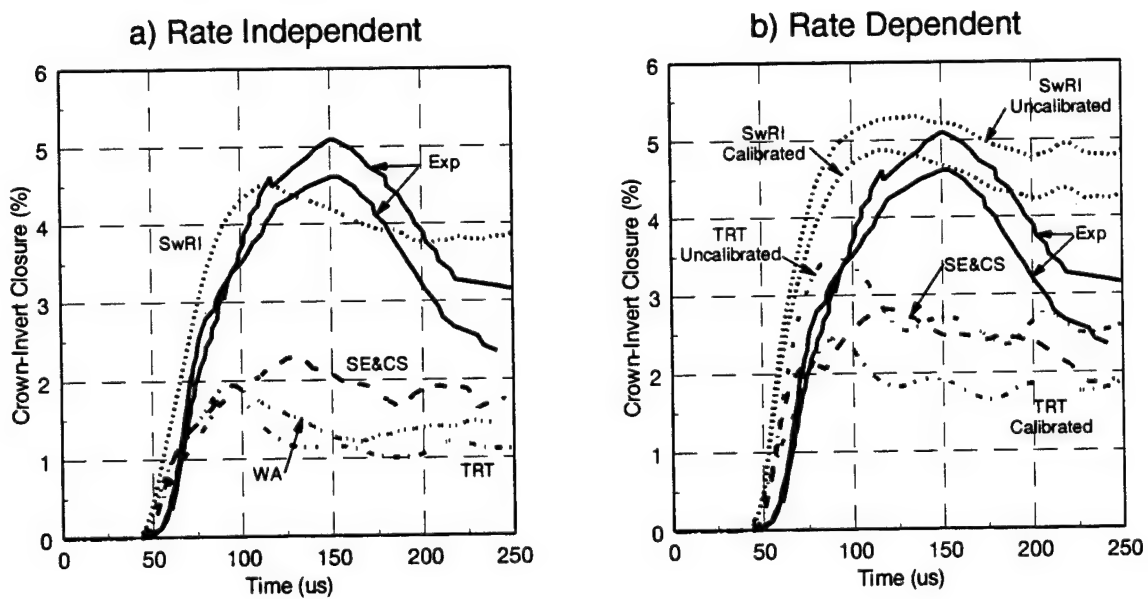


Figure 3-16. SWAT-II crown-invert closures for R=19.2 cm tunnel: a) rate-independent, b) rate-dependent.

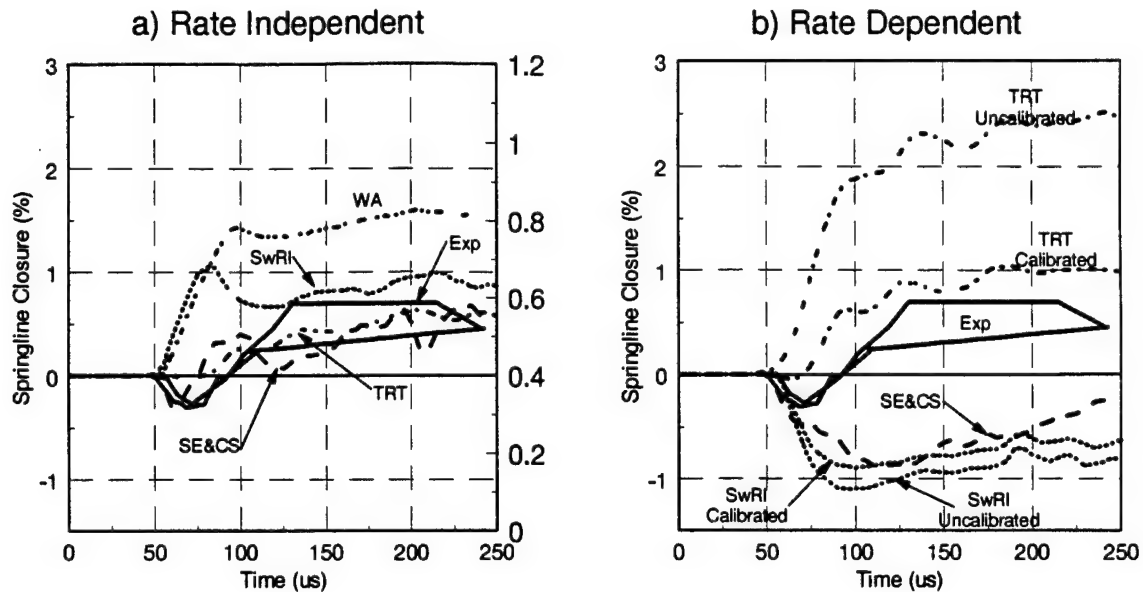


Figure 3-17. SWAT-II springline closures for R=19.2 cm tunnel: a) rate-independent, b) rate-dependent.

By including rate-effects, TRT predicted fundamentally different behavior than did either SE&CS or SwRI. TRT used independent rate-enhancement relations for the failure surface, cap hardening, and three-invariant yield surface relations. SwRI and SE&CS used the Duvaut-Lions linear overstress model. Since the Duvaut-Lions model is implemented within the constitutive model, it accounts for the spatial and temporal variation in strain-rate. In the Duvaut-Lions model, the yield surface is effectively moved outward (actually the viscid solution lies between the elastic and inviscid cases), which explains why stresses are higher (less yielding) and deformations are lower (material is stronger). Since both SE&CS and SwRI qualitatively agree, their models appear to be consistent. While the specific details of how TRT modified their cap parameters to reflect dynamic effects is unknown, this approach is probably what sets TRT apart from SE&CS and SwRI.

### 3.3.3 Summary of PTM Exercise.

It is clear from this exercise that more research is needed to develop "fully-defined" material models for large-deformation high strain-rate loading of geologic materials. For instance, calculations agreed fairly well with each other when the stress states were predominately triaxial compression, but differed significantly otherwise, indicating a large sensitivity to the shape of the yield surface in the  $\pi$ -plane. Upon further investigation, an equally large sensitivity was found in the details of how the shear failure and cap (crush) surface intersection was handled. Large variations in predictions also occurred when strain rate effects were accounted for.

Comprehensive testing programs should be carried out in conjunction with numerical modeling efforts to determine which effects are important and which are not. For example, standard

material tests on geologic materials primarily probe the compressive meridian of the failure surface. Through comparisons of numerical predictions in the current study, it was found that a significant portion of the structural response was due to yielding closer to triaxial extension than compression; however, the test data available to the modelers provided little guidance for defining the model in this regime. The next logical step is to take the lessons learned from the numerical predictions back to the laboratory and obtain more test data and repeat the modeling exercise. Beyond characterizing the location and shape of the failure surface, test data is also needed to characterize joint behavior, material damage, and flow direction.

Several conclusions from the PTM study can be made:

1. The constitutive models capture the main effects in large-deformation high strain-rate loading of geomaterials; however, predictions made using these models were sensitive to small changes in the model. This suggests that further research and model development is needed.
2. More comprehensive and possibly non-standard testing is needed to fully define the material behavior. The testing must be performed in conjunction with the modeling effort, as opposed to being performed once before the modeling effort begins.
3. Close attention must be paid to the modeling details such as loading rates, grid refinement and boundary conditions. An experienced and knowledgeable analyst is perhaps the key factor in obtaining high-quality solutions to complex highly-nonlinear numerical simulations.

The objective of SwRI's participation in the verification (Benchmark Activity) and validation (Precision Test Modeling) programs was to develop an accurate deterministic numerical model for predicting tunnel deformation under high stress wave loading and establish confidence with the DNA in our ability to apply the model. The approach taken was to enhance the PRONTO solid dynamics program for modeling geomaterials and apply it to realistic problems by participating in verification and validation exercises. The results indicate that solutions obtained using the enhanced PRONTO model are quite good overall, and at least as good as most other numerical models currently in use. This provides confidence in probabilistic predictions made using the enhanced PRONTO model.

## SECTION 4

### PROBABILISTIC ANALYSIS METHODS

#### 4.1 INTRODUCTION.

The fundamental problem faced in probabilistic structural analysis is that of propagating input parameter uncertainties through a numerical model to compute the response uncertainty. Once the response uncertainty is known, the probability of failure is quantified and can be used to make decisions regarding design changes, etc. Since the numerical model is usually computationally-intensive to evaluate, the challenge is then to develop a probabilistic analysis methodology that can obtain solutions nearly as accurate as Monte Carlo simulation, but at a much more reasonable cost.

Most of the probabilistic algorithms described in this Section are based on a class of methods known as fast probability integration (FPI), which have been shown to be extremely efficient relative to Monte Carlo simulation with comparable accuracy. For probabilistic finite element analysis, the Advanced Mean Value (AMV) method is recommended. Two simulation methods—Latin hypercube and Adaptive Importance Sampling—are also found to be useful for verifying other approximate methods.

#### 4.2 UNCERTAINTY MODELING.

##### 4.2.1 Random Variables and Systematic Errors.

Input uncertainties arise as a result of naturally occurring variations, called randomness, in quantities such as material properties, joint spacing, or loading. Another form of uncertainty can be identified as modeling or systematic error, which includes errors introduced into the calculations by the use of simplified models (deterministic and probabilistic), human error, and bias. Randomness is intrinsic to nature and beyond our ability to control, as compared to systematic error which can be reduced by some degree.

Random variables are modeled using a joint probability density function (pdf). The joint pdf provides a mathematical relation for describing how the input parameters vary. Definition of a marginal pdf (i.e., for a single variable) is typically made using a mean value  $\mu$ , a standard deviation  $\sigma$ , which is a measure of the scatter, and a distribution type, which defines how the scatter is distributed. As an illustration, Figure 4-1 shows the pdf for a variable with the same mean (30,000) and standard deviation (3000), but with different distributions (normal and extreme value).

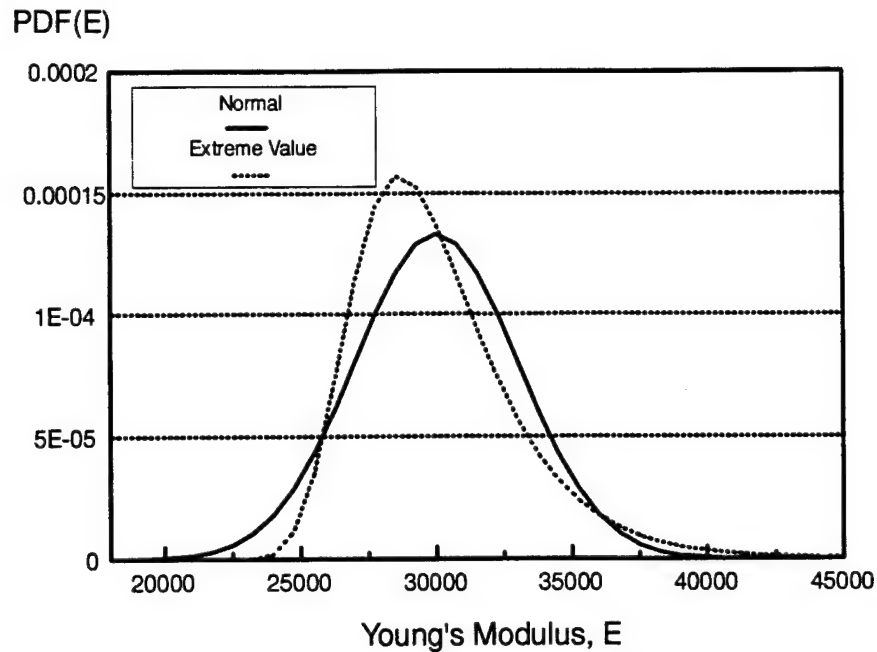


Figure 4-1. Normal and extreme value pdf.

To determine the parameters of the random variables, statistical tools such as the graphical method, method of moments, method of maximum likelihood, least squares estimators, and Bayes' estimators can be used (Ang and Tang, 1984). However, in most cases the accuracy of the selection is not clear, especially for the selection of the distribution type. Therefore, methods have been developed to test the quality of these parameters such as hypothesis testing and goodness of fit tests.

Approaches for modeling random variables and systematic error in geomechanics problems are discussed in Torng and Thacker (1992b). The various types of uncertainties discussed are broadly classified as being either reducible or irreducible, corresponding to systematic error and randomness respectively. The approach taken is to use a probabilistic approach to treat both types of uncertainties. Irreducible uncertainties are modeled as random variables, which results in a corresponding uncertain response. Reducible uncertainties, on the other hand, are treated by assuming that the mean and standard deviation of the reducible random variables are random, which results in a confidence bound on the calculated probability. Another option for treating reducible uncertainties is to perform two (or more) probabilistic calculations to bound the true solution. Although the form of the result from bounding analyses bear some resemblance to confidence bounds, the manner in which the underlying uncertainty is reflected in the bounds is different. More discussion on confidence bounds is given in Section 4.8.

#### 4.2.2 Random Fields and Spatial Variability.

In geomechanics, spatial variability can be a large source of uncertainty. Variables possessing spatial or temporal variability in addition to inherent randomness are modeled as random fields. An example of a random field is the spatial variation of a random material property within a layer of soil or rock. Because the material property between two points  $\{i, j\}$  are likely to have similar values if they are located close to each other, the property is said to be spatially correlated. A fully correlated random field implies that if the material property at one point in the layer is known, all other points in the layer are also known. At the other extreme, fully uncorrelated random field implies that the material property at point  $i$  is independent of point  $j$  regardless of how near point  $i$  is to point  $j$ . In most cases, the random field is partially correlated.

Since the true correlation is difficult to measure between every point  $i$  and  $j$ , correlation functions are usually used that describes the manner in which the correlation decays with distance or time. A typical correlation function is

$$\rho_{i,j} = e^{-\frac{\Delta}{l}} \quad (4.1)$$

where  $\Delta$  is the distance between points  $i$  and  $j$  and  $l$  is the characteristic length. The characteristic length is estimated, measured, or related to other characteristics such as the scale of fluctuation. Given the mean and standard deviation at all points within the field (usually but not necessarily the finite element nodes for spatial fields) and the correlation matrix, a new set of uncorrelated random variables can be obtained by transformation. This new set of random variables are then used in the probabilistic analysis. The transformation is exact if the original variables are normally distributed. Further details on modeling random fields in probabilistic finite element calculations are given in (SwRI, 1991).

#### 4.3 LIMIT STATE FUNCTION.

Given a deterministic tunnel response model such as those described in Section 2, tunnel response can be represented in the form of a response function such as:

$$Z(X) = Z(X_1, X_2, \dots, X_n) \quad (4.2)$$

where  $Z(X)$  represents the tunnel response (e.g., closure) and  $X_i$  are random design variables such as material properties, geometry, or loading. To indicate failure, a limit state function can be written in terms of Eqn. (4.2) as

$$g(X) = Z(X) - Z_0 = 0 \quad (4.3)$$

where  $Z_0$  is a value of  $Z(X)$  such that  $g(X) = 0$  denotes the boundary between failure and non-failure. Thus, Eqn. (4.3) separates the design space into "fail" and "safe" regions. The probability of failure  $p_f = P[g(X) \leq 0]$  is defined as the cdf value of  $Z$  at  $Z_0$ , or

$$p_f = \int_{\Omega} \dots \int f_X(X) dX \quad (4.4)$$

where  $f_X(X)$  is the joint probability density function for  $X$  and  $\Omega$  is the failure region given by  $g \leq 0$ . The complete cumulative distribution function (cdf) (ranging from 0% to 100% probability) can be constructed by simply varying  $Z_0$  and re-evaluating Eqn. (4.4).

Except for a few trivial cases, Eqn. (4.4) has no closed-form solution. Thus, numerical methods such as simulation or numerical integration must be used. In the following sections, several of these methods are briefly described.

#### 4.4 SIMULATION METHODS.

Simulation methods repeatedly evaluate the deterministic model to generate a sample of the response, from which the statistics (e.g., mean, standard deviation, etc.) are approximated. A major advantage of simulation is that the deterministic model does not have to be simplified or approximated to perform the analysis. Also, most simulation methods are exact as the number of simulations approaches infinity, which makes it attractive for checking or verifying an approximate method of probability calculation. The main disadvantage to simulation is that the probabilistic analysis can become quite costly if the deterministic model is complex. Even if the deterministic model is simple to evaluate, the analysis can get time consuming if small failure probabilities are to be estimated, which is usually the case. This can be demonstrated using the relation,

$$\% \text{ error} = 200 \sqrt{\frac{1 - p_f}{N p_f}} \quad (4.5)$$

where  $p_f$  is the failure probability and  $N$  is the sample size (Shooman, 1968). There is a 95% chance that the percent error in the estimated probability will be less than that given in Eqn. (4.5). Table 4-1 gives the total analysis time for various probability levels and deterministic function evaluation times based on 5% error.

Table 4-1. Monte Carlo simulation analysis times based on 5% error.				
		Analysis Time if 1 function evaluation takes:		
$p_f$	$N$	1 s	1 m	1 hr
0.5	1,600	27 m	27 hr	67 days
0.1	14,400	4 hr	10 days	1.6 years
0.01	158,400	44 hr	110 days	18 years
0.001	1,598,400	19 days	3 years	182 years
0.0001	15,998,400	185 days	30 years	1826 years

Because of the extremely long analysis times that can result as illustrated in Table 4-1, many efficient sampling methods have been developed. Two such methods are described in the following sections after a brief review of the direct, or Monte Carlo method.

#### 4.4.1 Monte Carlo Simulation.

Monte Carlo simulation is the most straightforward simulation method. For independent random variables, the steps involved are:

1. Generate an input vector by sampling from the input variable pdf's,

$$x_i = F_{x_i}^{-1}(u) \quad (4.6)$$

where  $u$  is a random selection from a uniform distribution,  $U[0,1]$ , and  $F_{x_i}^{-1}$  is the inverse cdf function of  $x$ .

2. Calculate the deterministic response,  $Z(X)$ .
3. Evaluate whether or not failure has occurred,  $g(X) = Z(X) - Z_0 \leq 0$ ?
4. Repeat steps 1-3  $N$  times.
5. Calculate  $p_f = N_f/N$ , where  $N_f$  is the number of samples resulting in  $g(X) \leq 0$ .

More details on the generation of independent or dependent random numbers, mapping from uniform to other distributions, and the calculation of response statistics are given in (Ang and Tang, 1984).

#### 4.4.2 Latin Hypercube Simulation.

Monte Carlo simulation can yield accurate failure probabilities provided the number of simulations is sufficiently large. Because failure probabilities are typically small, however, the required number of simulations and the calculational time required to perform a single simulation render this method impractical for most structural reliability applications (see Table 4-1).

Accuracies commensurate to that of standard Monte Carlo but with fewer required simulations can be achieved with constrained sampling schemes. One such scheme is Latin Hypercube simulation (LHS) (McKay, *et al.*, 1979). The basic idea in LHS is to distribute the samples such that the range of each variable is efficiently covered. In LHS, each of the  $k$  random variables is divided into  $n$  non-overlapping intervals based on equal probability, thereby creating  $k \times n$  subregions in the probability space. One sample is taken from each subregion based on the probability density in that region. Next, the  $n$  values for the first random variable are paired with the  $n$  values for the second random variable, and so on for all of the random variables. The  $n$  random vectors of length  $k$  are then used to perform the simulation.



The pairing of the variables in LHS can be performed in such a manner to induce a user-specified correlation between any two random variables (Iman and Conover, 1982). The induced correlations are based on the non-parametric technique known as rank correlation, which remain meaningful in the presence of non-normal distributions. LHS was used by Thacker and Senseny (1994) to verify a probabilistic cap model simulation involving correlated non-normal variables. This will be discussed further in Section 4.7.

#### 4.4.3 Adaptive Importance Sampling.

The approximate response function around the MPP (see Section 4.5) developed using the AMV+ (see Section 4.6) method provides only approximate probability without error estimates. It might be necessary to confirm the solution with minimal extra computations. One approach is to use an importance sampling method that performs sampling only in the region close to the MPP. There are several ways to develop importance sampling regions. In the adaptive approach proposed in (Wu, 1994), the initial sampling region is generated based on the AMV+ function and gradually increased by moving the sampling boundary until the sampling region covers the failure region sufficiently.

Figure 4-2 illustrates a curvature-based adaptive sampling method, in which the sampling boundary for a limit state is a parabolic surface that is rotationally symmetric about the vector  $OP$  that passes through the origin  $O$  and the MPP,  $P$ . The sampling region is increased by increasing or decreasing the curvature of the parabolic surface until there are no more failure points in the increased sampling region. Assuming a common curvature, the samples in the sampling region are generated first. Subsequently, extra samples are generated only in the increased region introduced by the curvature change. The probability increment for each curvature change can be evaluated and used as a basis for generating the probability-consistent number of samples. The details on how to generate samples and compute the failure probability are given in Wu (1994).

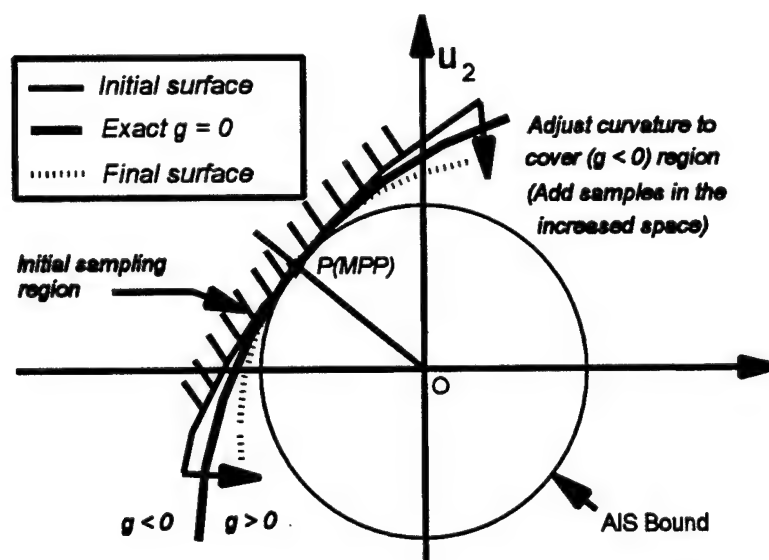


Figure 4-2. Illustration of the adaptive importance sampling (AIS) method.

The generated AIS samples can further be used to compute the probability sensitivities with respect to the probability distribution parameters (i.e., mean and standard deviation) of the input random variables. The computed sensitivities are accurate because the AIS-based sensitivities are based on the "exact" failure regions. Details on how to compute probabilistic sensitivities are discussed further in Section 4.9, Wu (1994), and Thacker and Wu (1995).

#### 4.5 FAST PROBABILITY INTEGRATION.

$Z(X)$  is oftentimes difficult to evaluate requiring a computationally intensive methods such as finite elements. Thus, the key to an efficient probabilistic analysis is one that minimizes the number of times  $Z(X)$  must be evaluated. As an alternative to Monte Carlo simulation, described in Section 4.4.1, more efficient numerical integration methods such as FPI can be used (Wu and Wirsching, 1987; Cruse, *et al.*, 1988; Wu and Burnside, 1988). The entire cdf can be efficiently constructed using the AMV+ (Section 4.6), which employs the FPI algorithm. A summary of the basic steps involved in FPI are as follows:

1. Obtain an approximation to the exact  $g$ -function using, for example, by finite differencing or perturbation methods.
2. Transform the original, non-normal random variables  $X$  into independent, standardized normal random variables (Ang and Tang, 1984),  $u$ .
3. Calculate the minimum distance,  $\beta$ , from the origin of the joint pdf (jpdf) to the limit state surface,  $g \leq 0$ . This point,  $u^*$ , on the limit state surface is the most probable point (MPP) in the transformed  $u$  space because it is the most probable combination (maximum jpdf) of the standardized normal random variables on the  $g \leq 0$  surface. Figure 4-3 shows a jpdf for two random variables, the limit-state, and the MPP.
4. Approximate the  $g$ -function  $g(u)$  at  $u^*$  or  $g(X)$  at the corresponding  $X^*$  using a first- or second-order polynomial function.
5. Calculate  $p_f = P[g \leq 0]$  using available analytical solutions (Madsen, *et al.*, 1986; Tvedt, 1990).

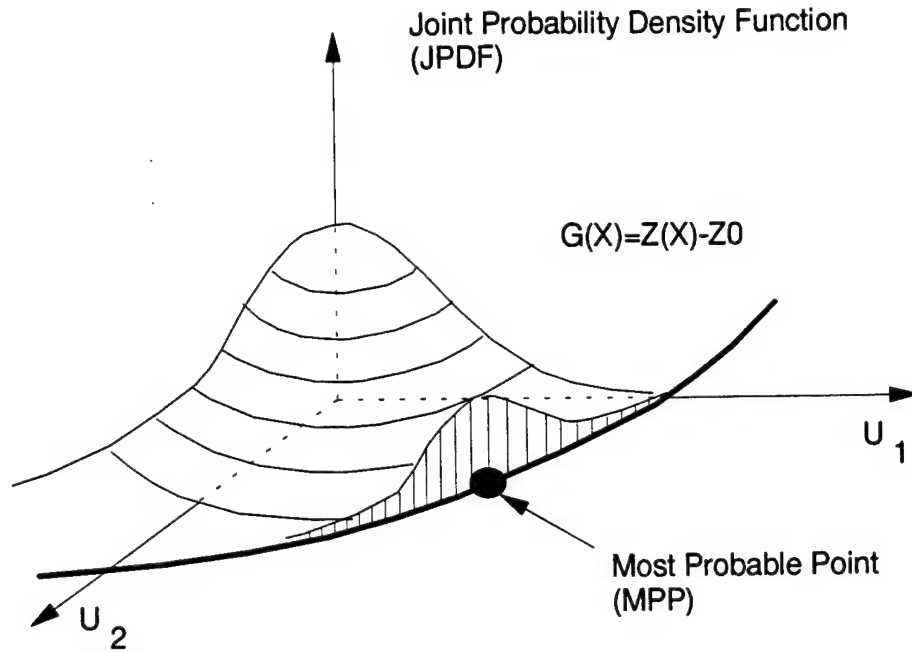


Figure 4-3. Joint pdf and MPP for two random variables in standard normal (u) space.

#### 4.6 ADVANCED MEAN VALUE METHOD.

The Advanced Mean Value iteration method (AMV+) was developed specifically for performing probabilistic finite element analysis (Wu, *et al.*, 1990). The algorithm couples the finite element code with an FPI code. Two different AMV+ algorithms have been developed: One algorithm is used when the value of the cdf is prescribed (i.e., when the probability level  $p$  is specified) and the corresponding response value  $z$  is to be computed. This algorithm is termed the  $p$ -level procedure. The other algorithm is used when the  $z$  value is prescribed and the corresponding probability is to be computed and is termed the  $z$ -level procedure.

The  $p$ -level procedure is used to compute the response corresponding to a specified probability, or  $p$ -level. The method is primarily used when points along the entire range of the cdf are to be computed (i.e., a "cdf analysis"). Table 4-2 gives the number of finite element solutions that are required to perform a first-order probabilistic analysis using AMV+. In Table 4-2,  $N$  is the number of input random variables and  $M$  is the number of  $p$ -levels. MVFO refers to "mean value first order" and AMVFO refers to "advanced" MVFO. In an MVFO analysis,  $(N+1)$  structural sensitivities are computed and used to construct a linear performance function ( $g$ -function) about the mean values of the random variables.

$$\begin{aligned} Z(X) &= Z(\mu) + \sum_{i=1}^N \frac{\partial Z}{\partial X_i} \bigg|_{\mu_i} (X_i - \mu_i) + H(X) \\ &= Z_1(X) + H(X) \end{aligned} \quad (4.7)$$

In step 2, a response update (or "move") is performed, which entails a finite element solution to update the response value at each of the  $M$  probability levels. This effectively approximates  $H(X)$  in Eqn. (4.7) with a simplified function  $H(Z_1)$ . If the change in  $Z$  from step 1 to step 2 is larger than the user-specified tolerance, Eqn. (32) is re-computed about the new MPP and step 2 repeated. This iteration procedure is the AMV+ method.

Table 4-2. Finite element solutions required to compute a CDF using the AMV+, p-levels, procedure.

Iteration	Step	Analysis	Number of Finite
0	1	MVFO	$N + 1$
0	2	AMVFO (Move)	$+ M$
1	3	First Order	$+ (N + 1) \times M$
1	4	Move	$+ M$
2	5	First Order	$+ (N + 1) \times M$
2	6	Move	$+ M$
.	.	.	.
.	.	.	.

The AMV+ z-level procedure is used to compute the response corresponding to a specified probability, or z-level. The method is primarily used for reliability analysis, where  $p$  must be calculated for a specific value of  $z$ . A more detailed description of both the p-level and z-level AMV+ procedures can be found in (Wu, *et al.*, 1990; Thacker, *et al.*, 1991).

#### 4.7 CORRELATED NON-NORMALS.

If the original random variables  $\mathbf{X}$  are dependent, a transformation must be made to a space in which the variables are independent before proceeding with the FPI calculations. If the joint pdf is available, the Rosenblatt (1952) transformation can be used:

$$\begin{aligned}
 u_1 &= \Phi^{-1}[F_1(x_1)] \\
 u_2 &= \Phi^{-1}[F_2(x_2|x_1)] \\
 &\vdots \\
 u_n &= \Phi^{-1}[F_n(x_n|x_1, x_2, \dots, x_{n-1})]
 \end{aligned} \tag{4.8}$$

where  $\Phi^{-1}$  represents the inverse standard normal cdf and  $F_i(\cdot|\cdot)$  denotes the conditional cdf. Typically, the complete joint pdf (jpdf) is very difficult to obtain based on either theory or experiment. In addition, the Rosenblatt transformation requires the inversion of the conditional distribution functions, which can be difficult to evaluate.

A less rigorous but more practical method of dealing with dependant non-normal variables is to approximate the jpdf by using the marginal pdf's and associated correlation matrix (Hohenbichler, *et al.*, 1981). An advantage of this model is that the required information is relatively easy to obtain from experimental data. The first step in the procedure is to transform the dependent non-normal variables  $\mathbf{X}$  to standard normal  $\mathbf{u}$ ,

$$\mathbf{u} = \Phi^{-1}[F_{\mathbf{X}}(\mathbf{X})] \quad (4.9)$$

Next, the correlation coefficients in the  $\mathbf{u}$ -space are computed using:

$$\rho_{x_i x_j} = \int_{-\infty}^{\infty} \int_{-\infty}^{\infty} \left( \frac{X_i - \mu_{x_i}}{\sigma_{x_i}} \right) \left( \frac{X_j - \mu_{x_j}}{\sigma_{x_j}} \right) \phi(u_i, u_j) du_i du_j \quad (4.10)$$

where,

$$\phi(u_i, u_j) = \frac{1}{2\pi \sqrt{1 - \rho_{u_i u_j}^2}} \exp \left[ \frac{-(u_i^2 - 2\rho_{u_i u_j} u_i u_j + u_j^2)}{2(1 - \rho_{u_i u_j}^2)} \right] \quad (4.11)$$

and  $\rho_{u_i u_j}$  is the unknown to be determined. This model, originally proposed by Nataf (1962), assumes that the  $\mathbf{u}$ -space variables are jointly normal. As a result, the maximum correlation assigned in the  $\mathbf{X}$ -space can be limited based on the input marginal distributions (e.g., two non-normal distributions in  $\mathbf{X}$ -space cannot be fully correlated and also be jointly normal). This is discussed further by Liu and Der Kiureghian (1986), who also present approximate solutions to Eqn. (4-10) for several different distribution combinations.

For use in a general computational framework in which any two variables may be correlated regardless of distribution type, a more general solution procedure than the one proposed by Liu and Der Kiureghian (1986) is needed. The method employed here approximates Eqn. (4-10) using a high-order polynomial expansion and the normal characteristic function (Wu, *et al.*, 1989; Harren 1990).

Next, an orthogonal transformation matrix is constructed using  $\rho_{u_i u_j}$  and applied to transform the correlated normal random variables,  $\mathbf{u}$ , to uncorrelated normal random variables,  $\mathbf{v}$ ,

$$\mathbf{v} = \mathbf{A}^T \mathbf{u} \quad (4.12)$$

In Thacker and Senseny (1994), this model is used to demonstrate the importance of including correlations in probabilistic calculations. A limestone test specimen is subject to a spherically-divergent strain path. The SR cap constitutive model is used to model the material response in terms of nine material parameters. Probability distributions for each parameter and the associated correlation matrix were measured from 20 repeat laboratory tests (Fossum, *et al.*, 1995). Probabilistic calculations were performed using the proposed model and verified using

Latin hypercube (correlated) sampling. The results show the approximate method described here to be very accurate relative to Latin hypercube sampling. The results also show significant differences in the computed probabilities between assuming no correlation and the measured correlation, thereby indicating the importance of including correlations in the probabilistic calculations.

#### 4.8 CONFIDENCE BOUNDS.

The methods for probabilistic analysis described in the previous sections all assume that the parameters of the random variables (mean, standard deviation, etc.) are all known with "high-confidence." Statistically, this implies that a large amount of data were available to characterize the random variables. In most applications, however, sufficient data is not available. Thus, some uncertainty will exist in the parameters of the random variables themselves.

As a precursor to developing an efficient procedure for constructing confidence bounds, a survey of methods for uncertainty modeling in geomechanics is given in Tornø and Thacker (1992b). This work proposes a scheme to construct confidence bounds for structural problems containing uncertainties due to inherent variability, estimation error, modeling error, and human error. The effect of the inherent variability is reflected in the calculated reliability, i.e., the cdf, whereas the effect of estimation error, modeling error, and human error are reflected in a confidence bound on the calculated reliability. Strictly speaking, then, the bounds should not be termed "confidence bounds," which is normally used to denote the uncertainty due to sampling error only. For lack of a better name, however, "confidence bounds" will be used here.

The proposed nested iteration procedure in Tornø and Thacker (1992a) is improved by Tornø and Thacker (1993) to utilize the probabilistic sensitivity factors ( $\alpha$ ) computed during the AMV+ probabilistic analysis. The basic idea is to construct a first-order Taylor series at the point of interest in the cdf

$$g(\mathbf{Y}) = \beta + \sum_{i=1}^n \frac{\partial \beta}{\partial \mu_{x_i}} (\mu_{x_i} - \mu_{x_{ip}}) + \sum_{j=1}^n \frac{\partial \beta}{\partial \sigma_{x_j}} (\mu_{x_j} - \mu_{x_{jp}}) - \Phi^{-1}(1 - p_f^*) \quad (4.13)$$

and compute the derivatives as discussed in Section 4.9. To demonstrate the efficiency of the new method, the procedure is applied to a limestone test specimen subject to divergent strain path loading. Of the six random variables considered in the problem, the unconfined compressive strength and joint spacing were assumed to have uncertain mean and standard deviation. Excellent results are obtained using very few g-function calculations.

To further illustrate the method, the procedure is applied to the analytical tunnel closure model described in Section 2. In this problem, only the mean of the external pressure is assumed to be a random variable with its own mean and standard deviation. The COV for the mean is defined as 2%, and is assumed to follow a normal distribution. None of the other random variables' parameters are modeled as random variables.

Figure 4-4 shows the cdf and confidence bounds for the 50% and 95% confidence levels computed using Monte Carlo and the method described here. Any confidence level can be

chosen; these are selected only to demonstrate the type of result obtained. As shown in Figure 4-4, the proposed method obtains excellent results at a fraction of the cost of using Monte Carlo.

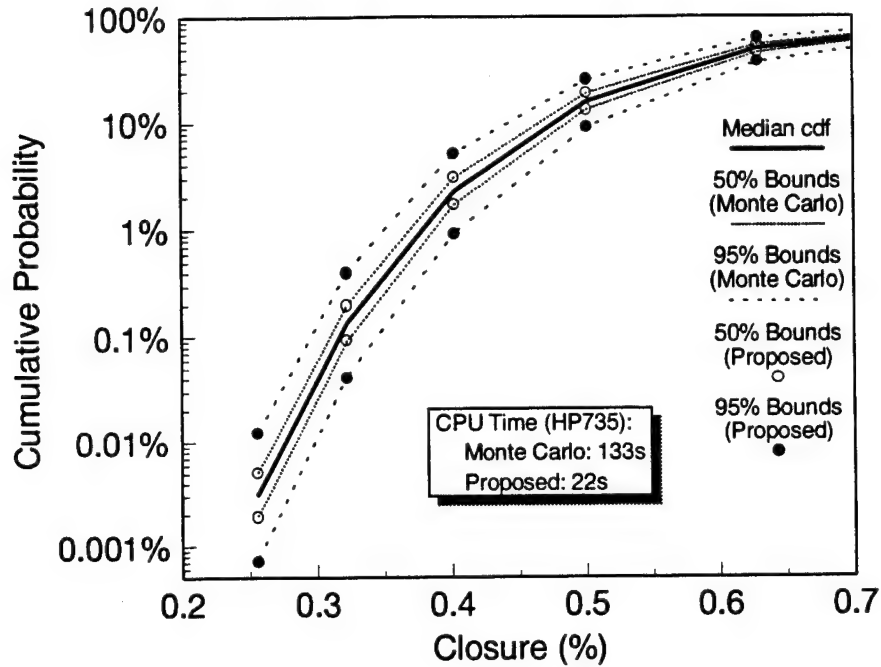


Figure 4-4. 50% and 95% confidence bounds for the analytical tunnel closure model.

#### 4.9 SENSITIVITY ANALYSIS.

For planning and design purposes, it is important to know which problem parameters are the most important and the degree to which they control the design. This can be accomplished by performing a sensitivity analysis. In a deterministic analysis where each problem variable is single-valued, design sensitivities can be computed that quantify the change in some performance measure due to a change in the parameter value.

In a probabilistic analysis each variable is usually characterized by a mean value, a standard deviation, and a distribution type, i.e., three parameters instead of one. The performance measure is usually the failure probability or the safety index  $\beta$ , which is closely related to the failure probability. Sensitivity measures can be defined with respect to each of these probabilistic parameters or a change in any of the deterministic parameters. In the following sections, the calculation of deterministic and probabilistic sensitivities are summarized using both sampling and numerical probability integration methods.

#### 4.9.1 Design Sensitivities.

Design sensitivities measure the change in response due to a change in an input parameter. Denoting the response as  $Z$  and the input variables as  $X_i$ , the response function can be written as

$$Z = Z(X_1, X_2, \dots, X_n) = Z(\mathbf{X}) \quad (4.14)$$

where  $n$  is the total number of input parameters. From this the  $i$ -th design sensitivity is given by

$$\frac{\partial Z}{\partial X_i} \quad (4.15)$$

#### 4.9.2 Probabilistic Sensitivities.

Design sensitivities only reflect the deterministic importance of the problem variables. In a probabilistic analysis, meaningful sensitivity measures are how  $p_f$  changes with respect to changes in input parameters. The input parameters in a probabilistic analysis generally include the mean, standard deviation and distribution type for each problem variable.

The limit-state function

$$g = Z(\mathbf{X}) - z = 0 \quad (4.16)$$

is written such that for a specific response  $z$ ,  $\{g: g \leq 0\}$  denotes the failure set. Probabilistic analysis methods such as FPI, FORM, SORM, etc., use an optimization algorithm to locate the minimum distance from the limit-state to the origin, denoted  $\beta$ . Calculations are typically performed in standard normal space, or  $u$ -space. For normally distributed variables, the transformation from  $\mathbf{X}$  to  $\mathbf{u}$  is given by  $u_i = (X_i - \mu_i) / \sigma_i$ . For non-normal variables, the transformation is usually nonlinear and must be performed numerically, as described later. Once the minimum distance point  $u_i^*$  is located, a first-order approximation to  $p_f$  can be computed from

$$p_f = \Phi(-\beta). \quad (4.17)$$

where  $\Phi$  is the standard normal cdf. Thus, sensitivity measures in terms of  $\beta$  can also be calculated in terms of  $p_f$  by applying Eqn. 4.17. In the  $u$ -space,  $\beta$  is given by

$$\beta = \sqrt{\sum (u_i^*)^2} \quad (4.18)$$

so

$$\frac{\partial \beta}{\partial u_i^*} = \frac{u_i^*}{\sqrt{\sum (u_i^*)^2}} = \frac{u_i^*}{\beta} = \alpha_i^* \quad (4.19)$$



where the  $\alpha_i^*$  are the probabilistic sensitivity factors. FPI methods compute  $\alpha_i^*$  as a by-product of the optimization algorithm from the g-function gradient calculation,

$$\alpha_i^* = -\frac{\nabla g(u^*)}{|\nabla g(u^*)|} = \frac{\left(\frac{\partial g}{\partial u_i^*}\right)}{\sqrt{\sum_i \left(\frac{\partial g}{\partial u_i^*}\right)^2}} \quad (4.20)$$

which show that the  $\alpha_i^*$  are proportional to  $\partial g/\partial u_i^*$ . For normally distributed variables, transforming to  $X$ -space gives,

$$\frac{\partial g}{\partial u_i^*} = \frac{\partial g}{\partial X_i^*} \frac{\partial X_i^*}{\partial u_i^*} = \frac{\partial g}{\partial X_i^*} \cdot \sigma_i \quad (4.21)$$

which shows that  $\alpha_i^*$  are proportional to the design sensitivity  $\partial g/\partial X_i^*$  and standard deviation of the  $i$ -th variable. For non-normal variables,  $\partial g/\partial u_i^*$  will generally also be a function of the mean. From Eqn. 4.21 and 4.19, it is seen that  $\alpha_i^*$  reflects the  $i$ -th variable's contribution to  $p_f$ .

The magnitude of  $\alpha_i^*$  can be used to rank the random variables in order of importance. The sign of  $\alpha_i^*$  can be used to determine how to change  $p_f$  by adjusting  $\alpha_i^*$ . Since  $\alpha_i^*$  is a function of several basic parameters, it is more useful to know how  $p_f$  (or  $\beta$ ) changes with respect to a change in the mean or standard deviation. For normally-distributed variables, these are easily derived as

$$\frac{\partial \beta}{\partial \mu_i} = \frac{\partial \beta}{\partial u_i^*} \frac{\partial u_i^*}{\partial \mu_i} = -\frac{\alpha_i^*}{\sigma_i} \quad (4.22)$$

$$\frac{\partial \beta}{\partial \sigma_i} = \frac{\partial \beta}{\partial u_i^*} \frac{\partial u_i^*}{\partial \sigma_i} = -\frac{\alpha_i^*}{\sigma_i} u_i^*$$

For non-normal variables,  $\partial u_i^*/\partial \mu_i$  and  $\partial u_i^*/\partial \sigma_i$  are computed numerically as follows. First the mapping function from  $X$ -space to  $u$ -space is defined

$$u_i = \Phi^{-1}[F_x(x_i, \theta)] = T(x_i, \theta) \quad (4.23)$$

where  $F_x$  is the cdf of  $x$ , and  $\theta$  are the parameters of  $F_x$ . Next,  $\partial u_i^*/\partial \theta_i$  is approximated as

$$\frac{\partial u_i^*}{\partial \theta_i} \approx \frac{T(x_i^*, \theta) - T(x_i^*, \hat{\theta})}{\theta_i - \hat{\theta}_i} \quad (4.24)$$

where the "^^" signifies a perturbation.

So the procedure is to perturb  $\theta_i$  to  $\hat{\theta}_i$ , compute  $T(x_i^*, \hat{\theta})$  and substitute into (4.24). Although approximate, only the mapping is changed, so no further g-function calculations are required.

#### 4.9.3 Sampling Based Probabilistic Sensitivities.

The samples used in the AIS (or Monte Carlo) analysis can be used to compute sensitivity measures. Since no further g-function calls are required, the sampling-based sensitivities can be computed quite economically. The basic idea is presented in (Wu, 1994) and summarized here. The analysis is extended to include lognormal variables and applied to a tunnel closure problem in Thacker and Wu (1995).

By definition

$$p = \int_{\Omega} \dots \int f_x dx \quad (4.25)$$

where  $\Omega$  is the failure region and  $f_x$  is the pdf of  $x$ . The nondimensional sensitivity of  $p$  with respect to a parameter  $\theta$  in  $f_x$  is then

$$\frac{\partial p/p}{\partial \theta/\theta} = \int_{\Omega} \dots \int \left[ \frac{\theta}{f_x} \frac{\partial f_x}{\partial \theta} \right] f_x dx = E \left[ \frac{\theta}{f_x} \frac{\partial f_x}{\partial \theta} \right]_{\Omega} \quad (4.26)$$

where  $E[\cdot]$  is the expectation operator. The sensitivity coefficients  $S$  with respect to the mean and standard deviation are thus

$$S_{\mu_i} = \frac{\partial p/p}{\partial \mu_i/\sigma_i} = E \left[ \frac{\partial f_{x_i} \sigma_i}{\partial \mu_i f_{x_i}} \right]_{\Omega} \quad (4.27)$$

$$S_{\sigma_i} = \frac{\partial p/p}{\partial \sigma_i/\sigma_i} = E \left[ \frac{\partial f_{x_i} \sigma_i}{\partial \sigma_i f_{x_i}} \right]_{\Omega}$$

In (Wu, 1994),  $S_{\mu_i}$  and  $S_{\sigma_i}$  are derived for the case where  $x_i$  is normally distributed,

$$S_{\mu_i}^{normal} = E \left[ u_i^2 - 1 \right]_{\Omega}$$

$$S_{\sigma_i}^{normal} = E \left[ u_i \right]_{\Omega} \quad (4.28)$$

The sensitivities can also be computed analytically when  $x_i$  are lognormal. The lognormal pdf is given by

$$f_x = \frac{1}{\sqrt{2\pi} \xi x} \text{Exp} \left[ -\frac{1}{2} \left( \frac{\ln(x) - \lambda}{\xi} \right)^2 \right] \quad (4.29)$$

where  $\xi = \sqrt{\ln(1 + \sigma^2/\mu^2)}$  and  $\lambda = \ln\mu + \xi^2/2$ . Computing  $\partial f_x / \partial \mu_i$  and  $\partial f_x / \partial \sigma_i$  and substituting into (4.27) gives

$$S_{\mu_i}^{\text{lognormal}} = \frac{\sigma_i e^{-(\lambda + \xi^2/2)}}{\xi} \left\{ (e^{-\xi^2} - 1) \left[ \left( \frac{u_i^2 - 1}{\xi} \right) - u_i \right] + u_i \right\} \quad (4.30)$$

$$S_{\sigma_i}^{\text{lognormal}} = \frac{\sigma_i}{\xi} \frac{1 - e^{-\xi^2}}{\sqrt{(e^{\xi^2} - 1)e^{\xi^2 + 2\lambda}}} \left( \frac{u_i^2 - 1}{\xi} - u_i \right)$$

where  $u_i = (\ln(x) - \lambda)/\xi$ . For other  $f_x$ ,  $\partial f_x / \partial \mu_i$  and  $\partial f_x / \partial \sigma_i$  are computed numerically.

#### 4.9.4 Sensitivity to Distribution Type.

Another important sensitivity is how  $p_f$  changes with respect to the distribution type, e.g., normal, lognormal, or Weibull. The question is important because oftentimes the available experimental data is adequate to characterize the mean and standard deviation, but inadequate to select the proper distribution type with a commensurate level of confidence. The choice of distribution type becomes increasingly important for low  $p_f$ .

The sensitivity measure used is the ratio of perturbed  $\hat{\beta}$  to the original  $\beta$

$$\gamma = \frac{\hat{\beta}}{\beta} \quad (4.31)$$

$\hat{\beta}$  can be computed by re-running the probabilistic analysis with the distribution type changed for one of the random variables, or estimated using an approximate procedure. The approximate procedure involves the following steps: (i) change the distribution type for the  $i$ -th random variable, (ii) compute a perturbed  $u_i^*$  using the new distribution type and (4.23), (iii) compute a perturbed  $\hat{\beta}$  using  $u_i^*$  and (4.18), and (iv) compute  $\gamma$  using (4.31). There are some situations where the approximate procedure breaks down. For example, switching from normal to lognormal with a negative variate will cause the procedure to fail. However, since no g-function evaluations are required, the approximate procedure can be an effective and simple method for estimating the distribution sensitivity.

## SECTION 5

### NUMERICAL EXAMPLES

#### 5.1 ANALYTICAL TUNNEL CLOSURE MODEL.

A probabilistic analysis and sensitivity study is performed using the analytical tunnel closure model. This model describes the closure of a circular opening in a Mohr-Coulomb medium subject to uniform internal and external pressure acting on the opening as described in Section 2.2. The problem variables are listed in Table 5-1. More detail on the probabilistic analysis can be found in Thacker and Senseny (1992).

Table 5-1. Random variables used in the probabilistic analysis.			
Variable	Mean	COV	Distribution Type
Young's Modulus, $E$	30,000 MPa	10%	Extreme Value
Poisson's Ratio, $\nu$	0.20	10%	Weibull
Unconfined Comp. Strength, $\sigma_u$	25 MPa	20%	Extreme Value
Friction Angle, $\phi$	30°	10%	Normal
Dilation Coefficient, $\chi$	0.75	5%	Truncated Normal $0 \leq \chi \leq 1.0$
External Pressure, $P_b$	90 MPa	10%	Lognormal
Internal Pressure, $P_a$	20 MPa	5%	Lognormal

Using the AMV+ procedure, the cdf (Figure 5-1) and  $\alpha_t$  (Figure 5-2) were calculated. As an example, for vulnerability assessments, a probability of kill  $p_k$  greater than 0.85 is desired. This probability corresponds to a cdf value of 15%. In this region of the cdf, two variables are dominate: Young's modulus and external pressure.

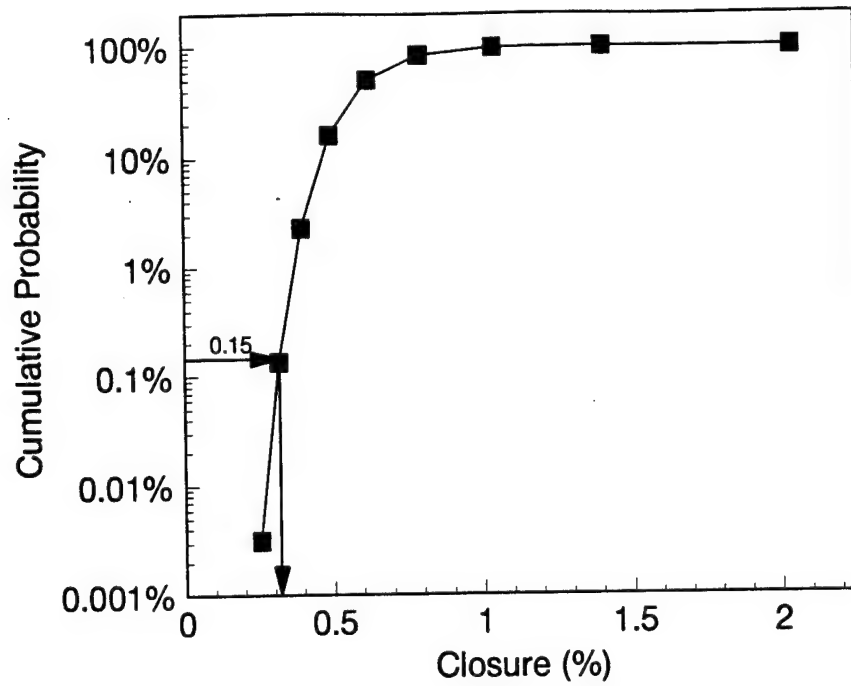


Figure 5-1. Cumulative distribution function for the analytical tunnel closure model.

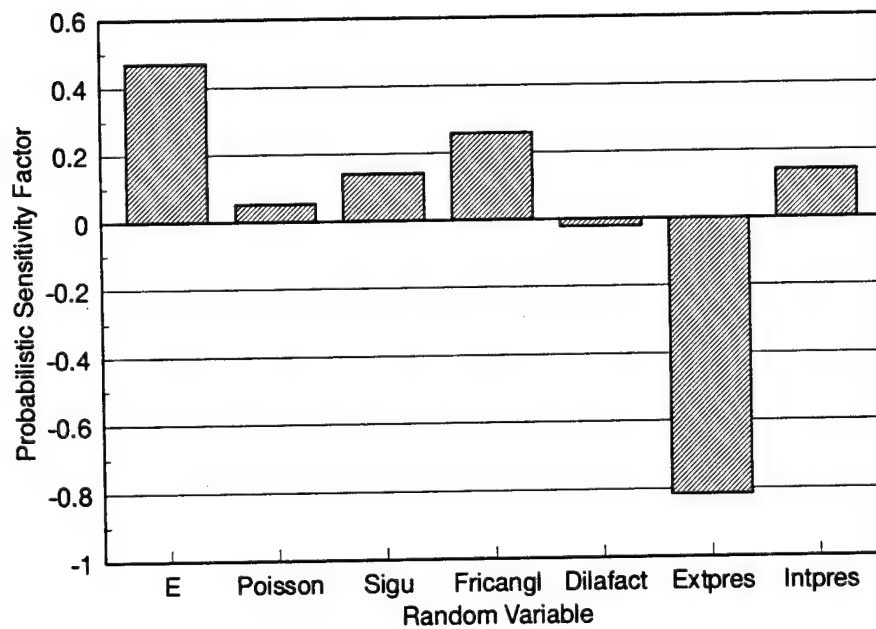


Figure 5-2. Probabilistic sensitivity factors ( $\alpha$ ) at  $cdf=15\%$  or  $p_k=0.85\%$ . As shown, Young's Modulus and external pressure are dominate.

Nondimensionalized design sensitivities computed as part of the AMV+ probabilistic analysis are shown in Figure 5-3.  $E$  and  $P_b$  are clearly dominate; however, the friction angle and internal pressure are also significant.

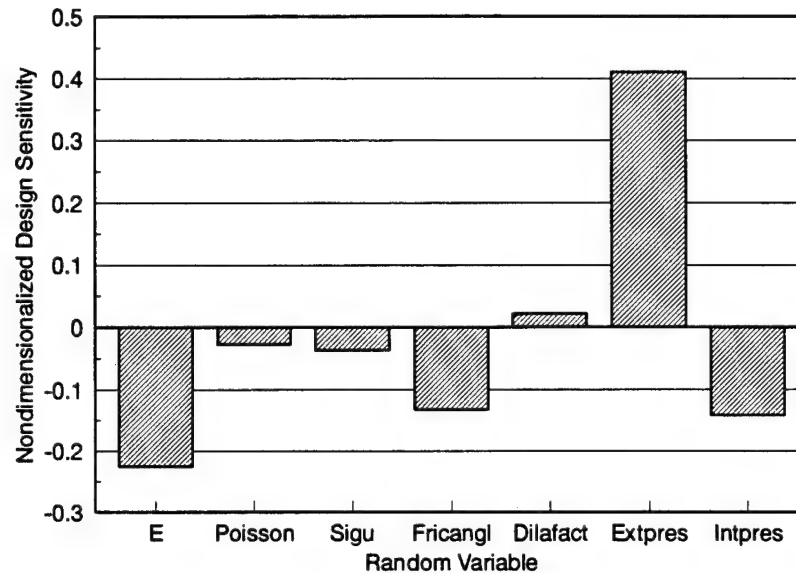


Figure 5-3. Design sensitivities at approximately  $p_k=0.85$ .

In Figure 5-4, the probabilistic sensitivity with respect to the mean ( $\partial\beta/\partial\mu$ ) is shown. Since  $\beta$  is directly related to probability, Figure 5-4 indicates that a change in the mean value of the dilation factor  $\chi$  would have the most impact on the probability.

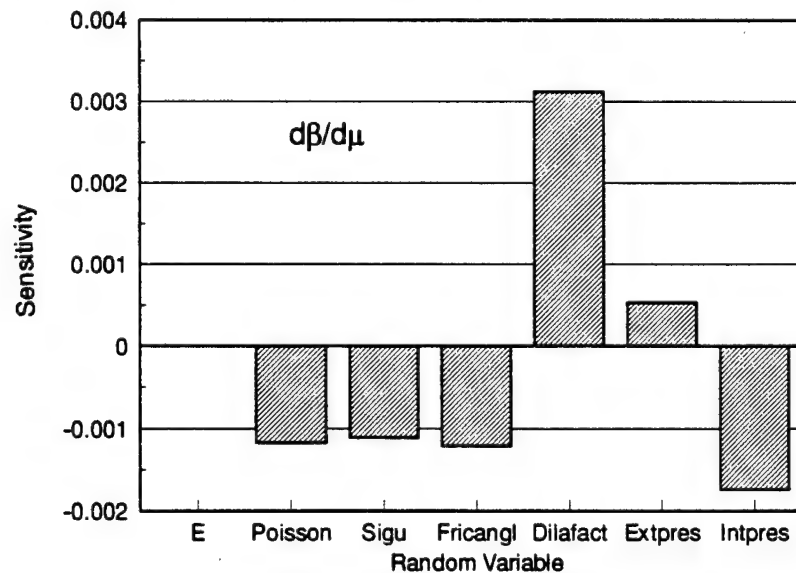


Figure 5-4. Probabilistic sensitivity with respect to mean.

The probabilistic sensitivity with respect to the standard deviation ( $\partial\beta/\partial\sigma$ ) is shown in Figure 5-5. Here it is seen that a change in the standard deviation of Poisson's ratio would have the most impact on the probability.

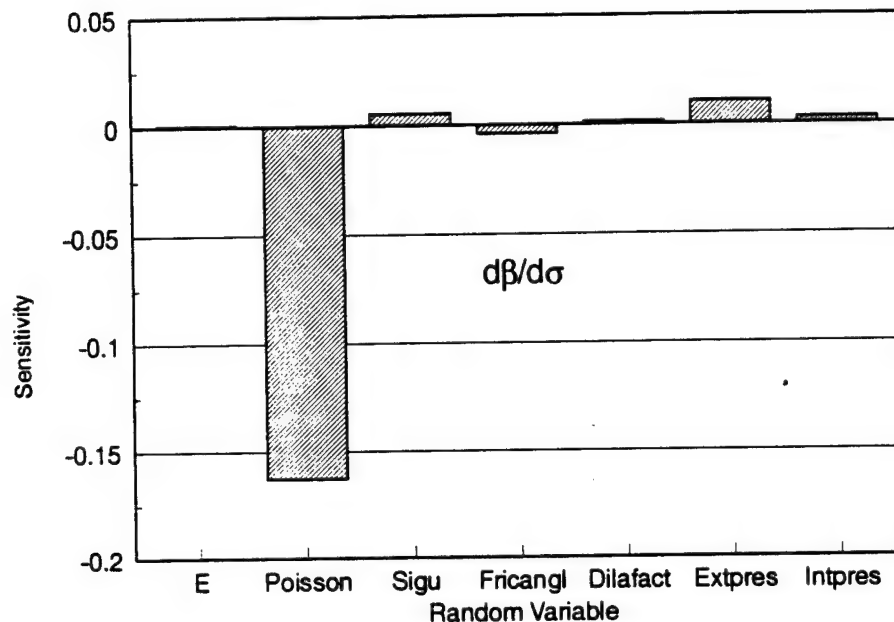


Figure 5-5. Probabilistic sensitivity with respect to standard deviation.

The potential error in assuming the wrong distribution type for the random variables is shown in Figure 5-6. The sensitivity measure used is  $\gamma = \hat{\beta}/\beta$  where  $\hat{\beta}$  is the perturbed beta corresponding to a change in distribution type. Four distributions for each variable are tested. The case where  $\gamma = 1$  indicates that no change in  $\beta$  was seen when the distribution type was changed. As shown, changing the distribution of E from its initial value (Extreme Value) to any of the other three distributions results in the largest change in  $\beta$ . Poisson's ratio, friction angle, external pressure and internal pressure are also sensitive to changing to the extreme value distribution in particular. In an actual design situation, however, certain distributions would be ruled out based on physical arguments and/or statistical goodness-of-fit.

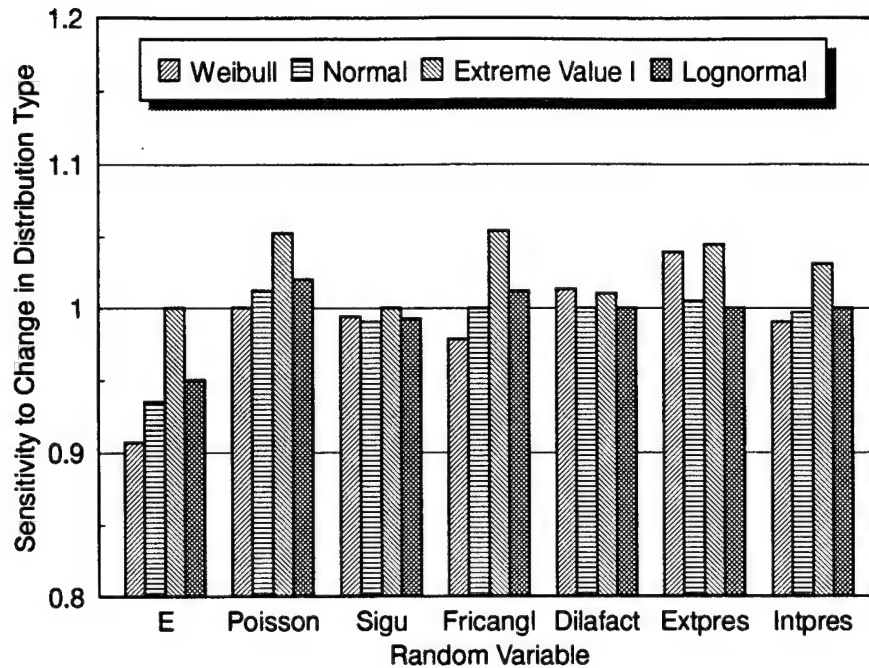


Figure 5-6. Sensitivity to change in probability distribution type.

Several points can be made regarding the probabilistic sensitivity results. First, more information is made available for decision making and planning than is available from a deterministic analysis. Only certain parameters of certain variables are actually controllable so it is important to know which controllable parameters will have the greatest impact on the design or plan. Second, the probabilistic sensitivities can reflect a much different picture than design (deterministic) sensitivities. Because of this, decisions based only on deterministic analysis results should be used with caution. Finally, from a computational standpoint, all of the sensitivity results derived earlier and illustrated here are very economical to calculate; most are obtained during the course of the probabilistic analysis. For those that must be computed after the probabilistic analysis, efficient methods as described earlier have been developed and implemented.

## 5.2 PROBABILISTIC DEEP TUNNEL ANALYSIS.

The probabilistic response of a deep buried tunnel subjected to a short-duration stress pulse is demonstrated. The problem is highly dynamic, involves nonlinear material behavior, and includes large uncertainties in the material properties, geometry, and loadings. An enhanced version of PRONTO2D is used to calculate the deterministic tunnel response. The failure mode considered is excessive closure. The AMV+ method is used to establish the cdf of tunnel closure with relatively few finite element re-solutions. Monte Carlo and AIS methods are used to verify the probabilistic solution. The results show the AMV+ method to be highly accurate and efficient.



The problem geometry and loading are shown in Figure 5-7. The analysis considers a steel-lined tunnel in a jointed rock mass subjected to a cylindrically-divergent stress wave. Plane strain conditions are assumed. The response of interest is maximum tunnel closure at any point in time.

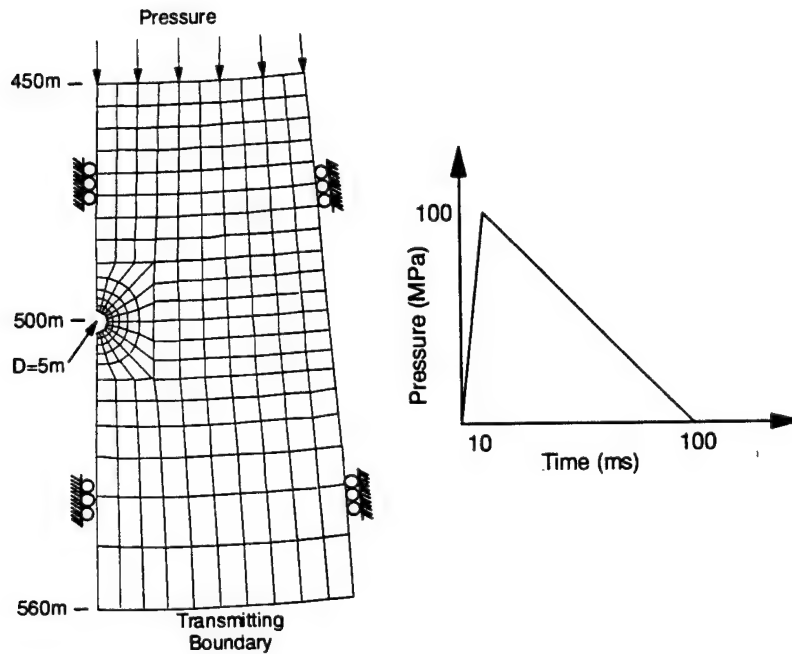


Figure 5-7. Problem description, finite element mesh, and loading.

The elastic jointed rock mass is modeled using the compliant joint model and the inelastic response is modeled using the Drucker-Prager model, described in Section 2.3.3.1. The joint spacing is 1 m and the orientation of the joint sets are horizontal and vertical with each set being perpendicular to the plane of the problem. The steel tunnel liner is 0.05 m thick and is modeled using an elastic-perfectly plastic material model. A frictionless contact surface is assumed at the rock-liner interface. The problem variables and corresponding values are listed in Table 5-2. A preliminary study of this problem using fewer random variables is given in (Riha, *et al.*, 1992). The rock properties are typical values for medium-strength rock.

The deterministic response is shown in Figure 5-8, where deformed shape plots of the tunnel liner and adjacent elements for several times through the analysis are shown. All tunnel closures are calculated at the outer surface of the liner. As the stress wave arrives at the tunnel, the tunnel takes on an oval shape with closure at the crown-invert and opening at the springline. Then, as the wave passes by the tunnel, the crown-invert closure decreases, causing the springline to begin to close. This is evidenced in Figure 5-8 by the liner pulling away from the rock on the sides as it is allowed to open at the crown-invert.

Table 5-2. Problem variables and inputs.				
Variable	Mean	Units	COV	Distribution
Young's Modulus	13,200	MPa	5.64	Extreme Value
Poisson's Ratio	0.23	-	10	Weibull
Peak Load	100	MPa	10	Lognormal
Density (2)	2420	kg/m <sup>3</sup>	0.2	Normal
Unconfined Comp. Strength (2)	51	MPa	8.6	Extreme Value
Friction Angle (1)	35	Degrees	14.3	Lognormal
Dilatation Angle (1)	35	Degrees	14.3	Lognormal
Tensile Strength	2	MPa	0.00	-
Density (liner)	7500	kg/m <sup>3</sup>	0.00	-
Young's Modulus (liner)	200	GPa	0.00	-
Poisson's Ratio (liner)	0.3	-	0.00	-
Yield Strength (liner)	400	MPa	0.00	-

(1) Fully correlated. (2) Dropped for AMV+ analysis.

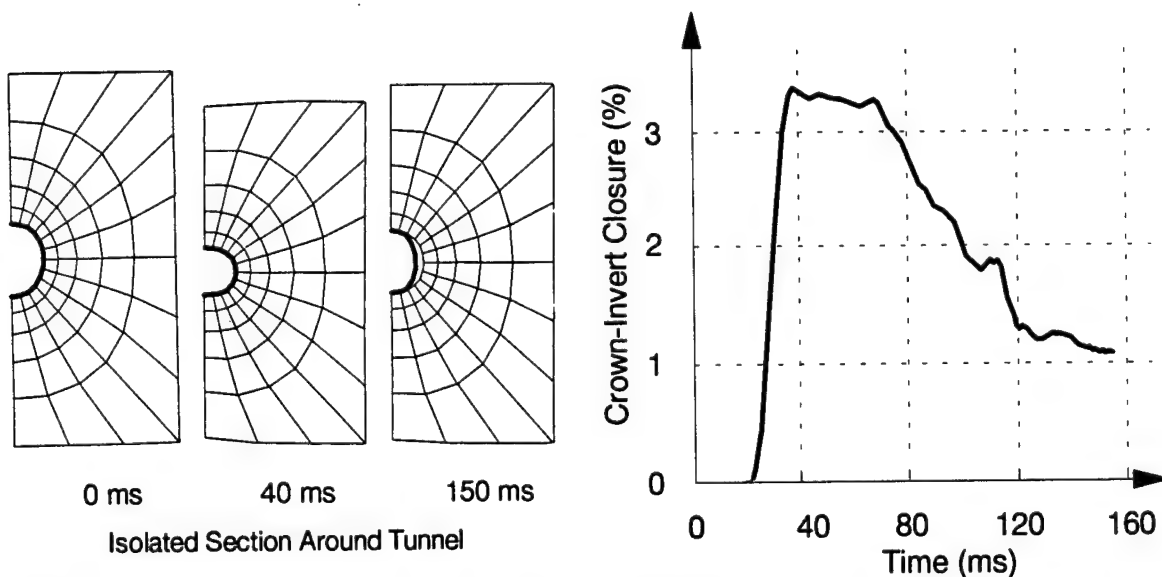


Figure 5-8. Deformed shape plots magnified 10X for several times during the analysis and the time history of crown-invert closure.

To save computation time in the probabilistic analysis, the deterministic analysis is stopped at 150 ms, when the loading portion of the stress wave had passed the tunnel. In addition to an analysis with the random variables at their mean values, two perturbations ( $\pm 0.5\sigma$ ) of each random variable are analyzed for a total of 15 deterministic analyses. The additional perturbations beyond that needed to construct a linear response function are performed to verify that the sensitivities were accurate and not being adversely effected by the unavoidable noise associated with transient direct integration solutions. The MV cdf based on these 15 FE solutions is shown in Figure 5-9.

To further save computation time, a sensitivity analysis was performed based on the MV solution. From this analysis, density and unconfined compressive strength were found to contribute only a small amount to the variation in crown-invert closure. Thus, these two variables were dropped (i.e., held at their deterministic mean value) during the AMV+ analysis.

To calculate converged probabilistic results (MPP locus), the AMV+ procedure is used. Since the primary goal of the analysis is to verify the probabilistic analysis approach, the convergence tolerance for the AMV+ iterations is set to 1%, which is smaller than what is typically required. The total number of FE solutions to compute the converged cdf using AMV+ (including the MV solutions) is 133. After confidence is gained, the convergence tolerance is usually relaxed and only single perturbations are used thereby greatly reducing the number of FE calculations required.

The cdf of tunnel closure is shown in Figure 5-9. The MV cdf is accurate at the 50% probability level where the approximate linear response function was initially constructed. However, in the tail regions the difference between the MV and AMV+ cdf's are more significant. Even though convergence was obtained using the AMV+ procedure, the probability calculation is still approximate because an approximate response function is used. To check quality of the probability calculation, Monte Carlo simulation is used. As shown in Figure 5-9, the results verify the AMV+ solution from about  $-2\sigma$  to  $+2\sigma$ . To verify the solution further out in the tails, the AIS method is used, which requires on the order of 100 FE solutions per point shown in Figure 5-9. To verify these regions of the cdf with Monte Carlo would have required thousands of FE calculations. It should be noted that the AIS analysis was performed only to verify the AMV+ solution; in practice a larger error tolerance for AIS would be used resulting in significantly fewer FE solutions.

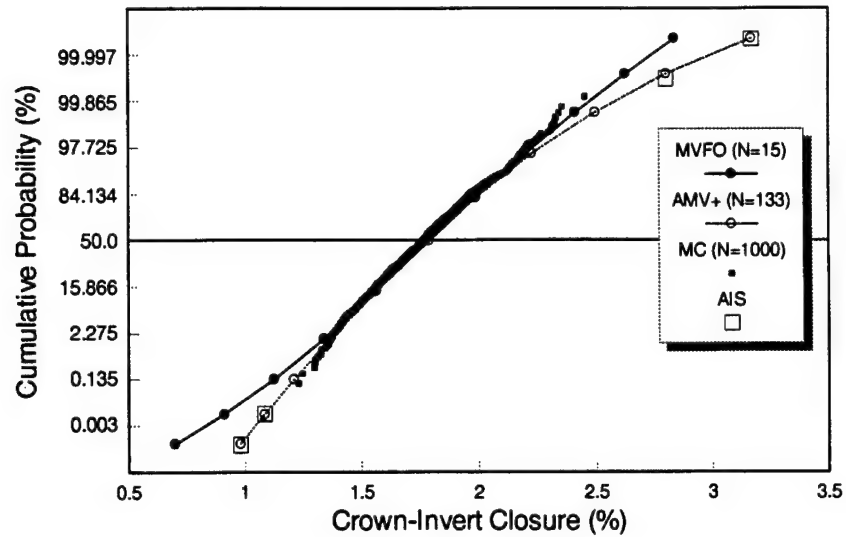


Figure 5-9. Cumulative distribution function for crown-invert tunnel closure.

The probabilistic sensitivity factors at a point in the lower and upper tails are shown in Figure 5-10. At low closure levels, Young's modulus contributes the most to the closure variation, whereas at higher closure levels the load becomes more important.

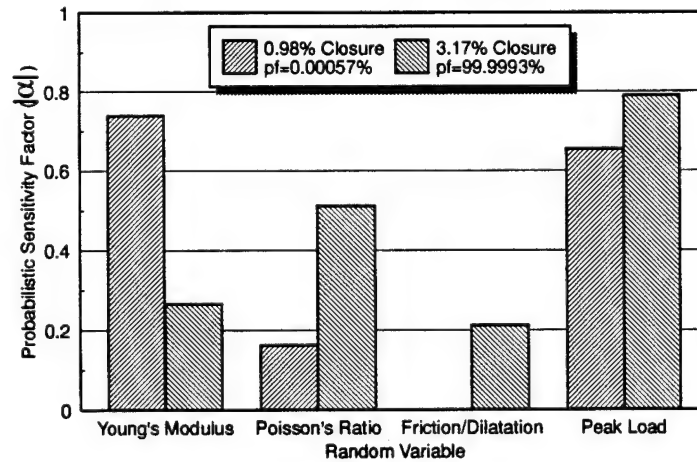


Figure 5-10. Probabilistic sensitivity factors for the deep tunnel problem.

This analysis demonstrates that advanced probabilistic algorithms employing fast probability integration methods can be used to predict the uncertain structural response of underground structures requiring nonlinear dynamic calculations.

### 5.3 TUNNEL VULNERABILITY ANALYSIS.

The problem studied is a shallow tunnel built into a sloped, multi-layered, geology. The conceptual model is shown in Figure 5-11. The tunnel is of size  $2R$  and has a retaining wall of height  $h$  at the adit. The geology considered has six layers of varying thickness (constant within each thickness) and S-number intersecting the tunnel at slope  $\theta$ . A weapon of mass  $M_p$  hits the hillside at velocity  $V_p$  at a distance  $X$  measured up from the retaining wall and a distance  $Y$  off the axis of the tunnel and penetrates until the velocity of the weapon reaches zero.

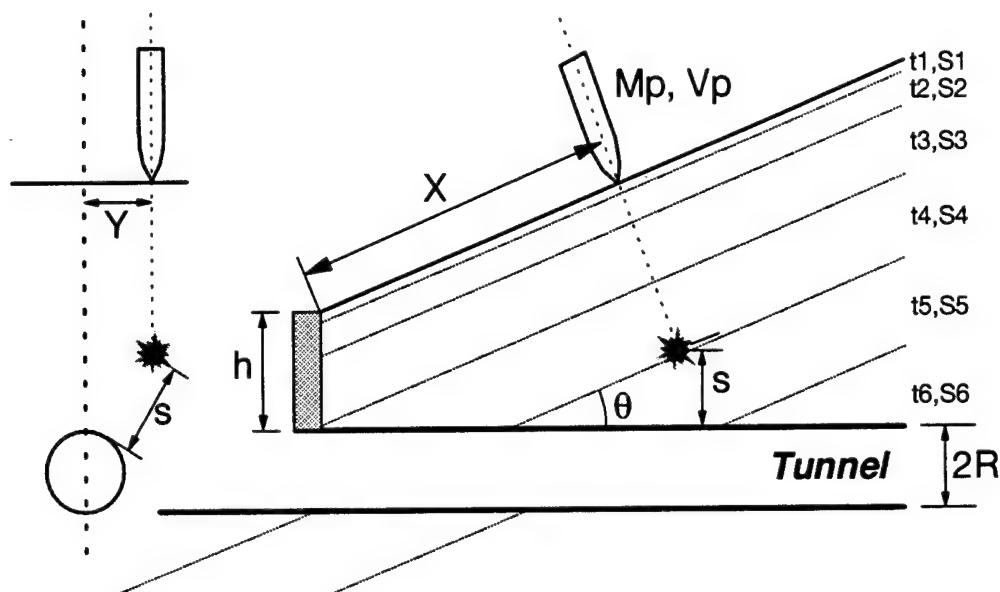


Figure 5-11. Conceptual tunnel vulnerability model.

The following assumptions and/or observations are made: 1) the layers are parallel to the surface of the hillside and do not change in thickness, 2) the weapon impacts the hillside at a right angle and does not change direction while penetrating, 3) the standoff to the tunnel is the absolute distance from the tunnel wall to the center of gravity of the weapon after the weapon reaches zero (effective) velocity, 4) the weapon can travel through the tunnel and into the layers underneath the tunnel, 5) and the weapon may not intersect the tunnel if  $Y > R$ .

A table of the model inputs is given Table 5-3. The mean and standard deviation for  $s_i$ ,  $t_i$ , and  $\theta$  were provided by Chitty (1995). Data for the remaining problem variables, including probability distribution types, were assumed. The modeling error  $B$  listed in Table 5-3 is a multiplier on the damage function in the probabilistic calculation.

Table 5-3. Model variables used in the tunnel targeting problem.				
Random Variable	Identifier	Mean Value	COV	Probability Distribution
Layer 1 Thickness	$t_1$	0.5 m	25%	Lognormal
Layer 1 S-number	$s_1$	10	20%	Lognormal
Layer 2 Thickness	$t_2$	1.0 m	25%	Lognormal
Layer 2 S-number	$s_2$	6	20%	Lognormal
Layer 3 Thickness	$t_3$	2.0 m	25%	Lognormal
Layer 3 S-number	$s_3$	2	20%	Lognormal
Layer 4 Thickness	$t_4$	5.0 m	25%	Lognormal
Layer 4 S-number	$s_4$	1.5	20%	Lognormal
Layer 5 Thickness	$t_5$	7.0 m	25%	Lognormal
Layer 5 S-number	$s_5$	1	20%	Lognormal
Layer 6 S-number	$s_6$	0.8	20%	Lognormal
Slope Angle	$\theta$	33.81 degrees	21%	Lognormal
Weapon Initial Velocity	$V_p$	335 m/s	10%	Lognormal
Transverse Aimpoint Error	$Y$	0.0 m	( $s = 1$ m)	Normal
Modeling Error	$B$	1	10%	Normal
Aimpoint	$X$	Variable	0%	-
Retaining Wall Height	$h$	3 m	0%	-
Tunnel Radius	$R$	2 m	0%	-
Weapon Mass	$M_p$	8.9 kN	0%	-
Damage Function Curve-fit Coeffs.	$C_i$	Variable	0%	-

A summary of the deterministic calculational procedure is given in Figure 5-12. For a given aimpoint, the first step is to compute the location of the layer interfaces. The tunnel is considered as an air layer, which offers no resistance to the weapon should it be encountered during penetration. As shown in right side of Figure 5-12, the presence of the tunnel could eliminate a layer, or the tunnel may not lie on the penetration path for some values of  $Y$ . Next, the penetration depth  $z_p$  (measured normal from the surface of the hillside with inward being positive) is computed using the PENCURV penetration program (Adley, *et al.*, 1994). After the penetration depth is computed, the standoff from the weapon center of gravity (cg) to the tunnel wall is computed. Finally, the damage (rubblized volume) is computed using the damage function, which is assumed to be a curve-fit to several known data points.

1. Calculate interface locations ( $z_i$ ) along line of penetration

- $z_i = f(X, t_i, \theta, h, R, Y)$
- Layers extend below tunnel
- Layers may be completely masked by tunnel
- Tunnel may not lie on penetration path

2. Calculate penetration depth

- $Z_p = \text{PENCURV}(z_i, S_i, V_p, M_p)$

3. Calculate Standoff

- $S_v = \text{Abs}[R + h + X \sin(\theta) - Z_p \cos(\theta)] - R$
- $S = \text{Sqrt}[(S_v + R)^2 + Y^2] - R$

4. Calculate Damage

- $V_r = C_0 + C_1(S) + C_2(S)^2 + \dots + C_m(S)^m$

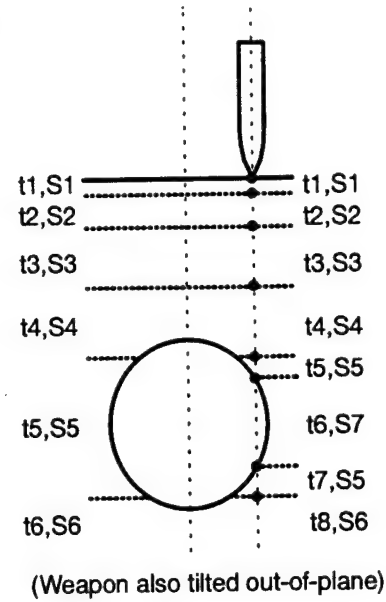


Figure 5-12. Deterministic calculation procedure.

Two damage functions (Figure 5-13) are considered, herein referred to as either the "long-tail" or "short-tail" damage functions, or  $f_1$  and  $f_2$  respectively. The short-tail function represents an exact fit through the three data points whereas the long-tail function represents a regression fit through the three data points and another point at  $\{11,0\}$ . Both functions pass through  $\{0,0\}$  and are given by:

$$f_1 \equiv V_r = \begin{cases} 61.25 s - 9.7 s^2 + 0.38 s^3 & 0 < s < 11.454 \\ 0 & \text{otherwise} \end{cases} \quad (5.1)$$

$$f_2 \equiv V_r = \begin{cases} 34.76 s + 1.67 s^2 - 0.71 s^3 & 0 < s < 8.24 \\ 0 & \text{otherwise} \end{cases}$$

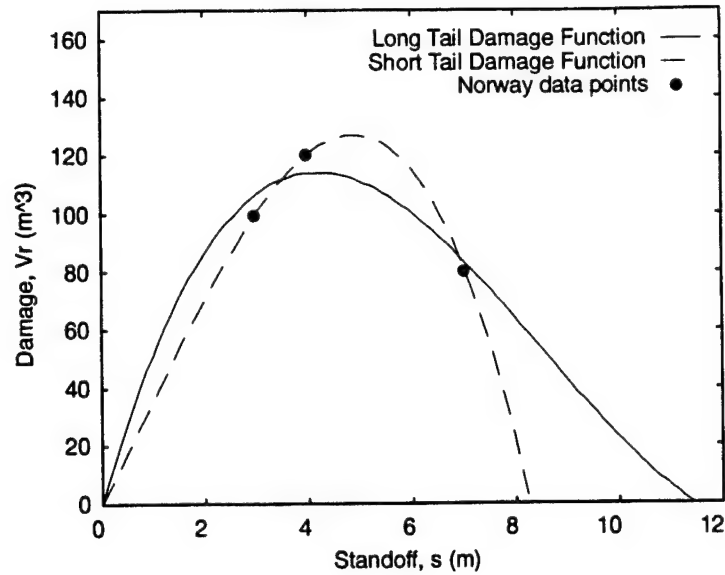


Figure 5-13. Damage functions.

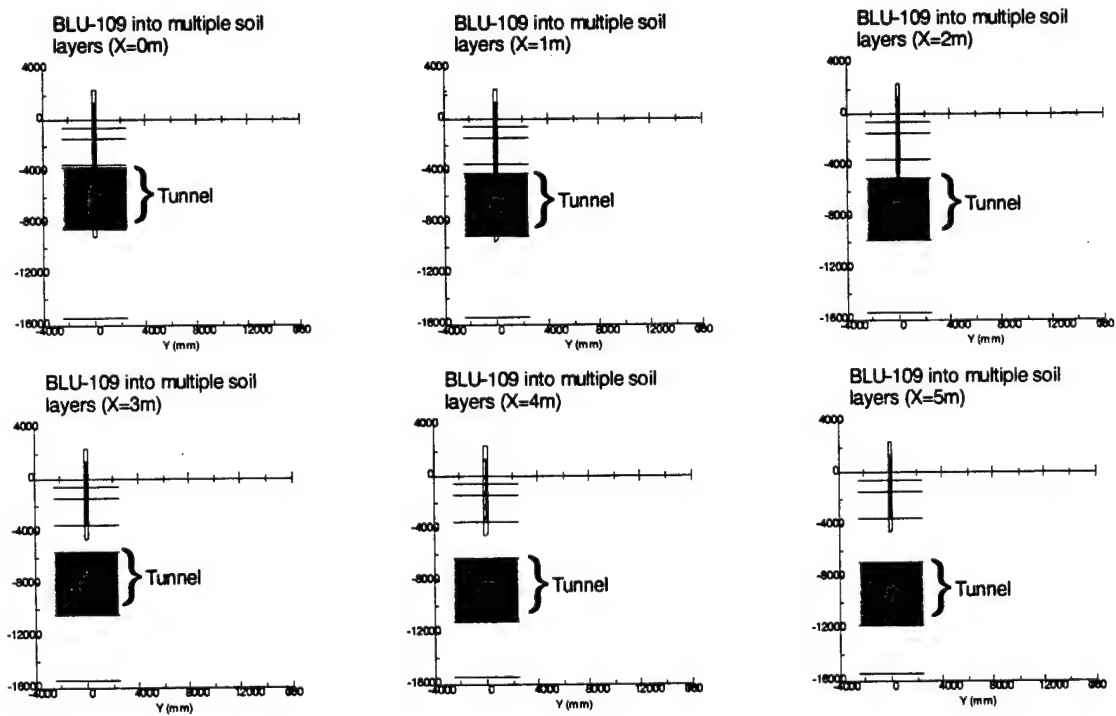


Figure 5-14. Sequence of penetration calculations at different aimpoints, X.

As an illustration of the deterministic calculations, Figure 5-14 shows the weapon penetration at six different aimpoints. As  $X$  increases, the distance from the surface of the hillside to the tunnel



increases. Thus, in the plots in Figure 5-14, the tunnel gets further away from the hillside surface for increasing  $X$ . Of interest is that for  $X < 3\text{m}$ , the weapon passes through the tunnel and stops shortly after reaching the other side. Since the cg of the weapon is still inside the tunnel, no damage is done as modeled by the functions given in (5.1).

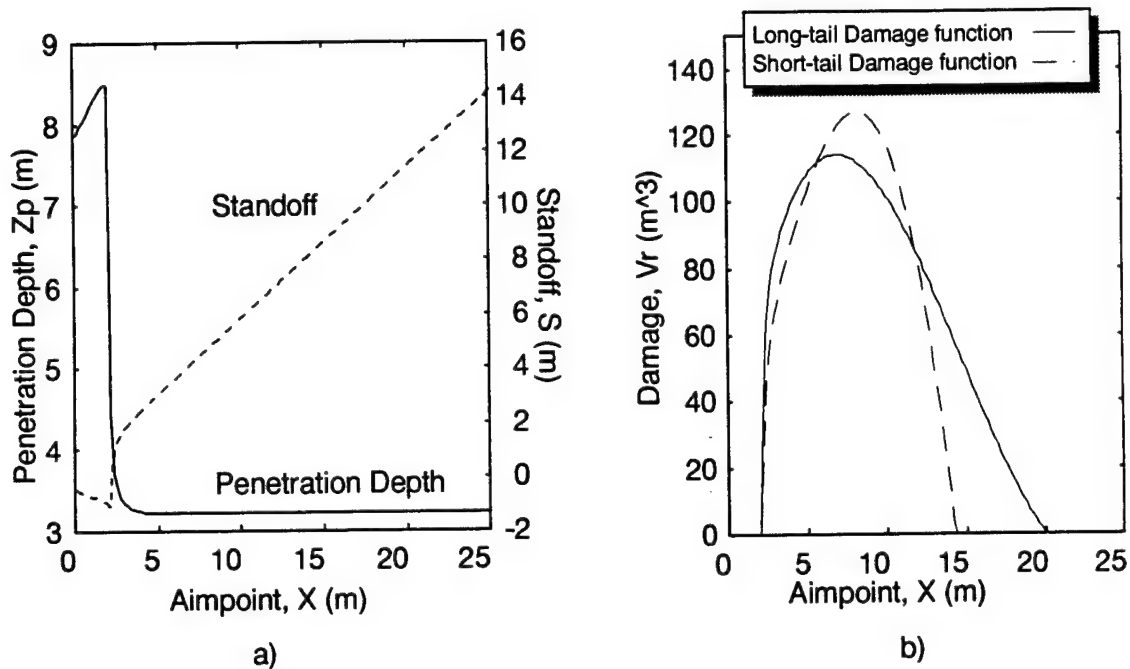


Figure 5-15. Deterministic calculational results: a) variation of penetration depth (left scale) and standoff (right scale) with aimpoint; b) variation in damage with aimpoint.

A series of aimpoints were run and the results plotted in Figure 5-15. Figure 5-15a shows the variation in penetration depth and standoff with aimpoint. The penetration depth increases initially due primarily to the slope of the hillside. At  $X \approx 2\text{m}$ , the penetration depth drops abruptly due to the fact that the weapon no longer penetrates through the tunnel. For  $X > 2\text{m}$ , the penetration depth is constant and the standoff increases linearly as expected. In Figure 5-15b, the variation in damage is plotted. For both either the long and short tail damage functions, the optimum aimpoint is around 8 to 10m.

A probabilistic analysis is performed using the deterministic tunnel vulnerability model, the inputs listed in Table 5-3, and the short-tail damage function. The cdf of damage represents the probability that the damage will be less than a given damage value; thus the vulnerability function is defined as  $1\text{-cdf}$  such that vulnerability denotes the same meaning as probability of kill ( $p_k$ ). For example, using Figure 5-16 it is seen that  $p_k$  is approximately 90% if the attack point is 8m and the kill criteria is a damage level of  $100\text{ m}^3$ . In other words, the probability that the damage will be greater than or equal to  $100\text{ m}^3$  is 90%, which also equals  $p_k$ .  $p_k$  can always be increased by decreasing the failure criteria; however, as shown in Figure 5-16,  $p_k$  cannot go above 90% if kill is assumed to occur at a damage level of  $100\text{ m}^3$ . From Figure 5-16 it is also seen that  $p_k$  goes down very quickly as the aimpoint varies from 8 m.

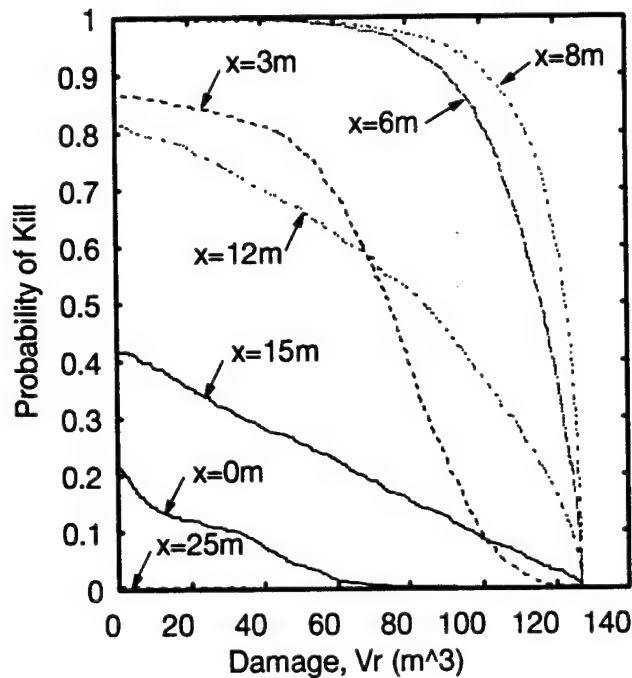


Figure 5-16. Vulnerability function ( $=1\text{-cdf}$ ).

The sensitivity to aimpoint is also seen in Figure 5-17, where  $p_k$  is plotted for many aimpoints. The maximum  $p_k$  is found (as in the deterministic calculation) to be around 8 m, but the probabilistic results also shows that  $p_k$  drops off severely as the aimpoint varies from 8 m. The initial peak seen in Figure 5-17 corresponds to a local maximum corresponding to the weapon detonating below the tunnel. This peak was not found in the deterministic calculation. To see the effect of choosing different kill criteria, two kill levels in addition to the  $100\text{ m}^3$  level are plotted. As shown, the range in  $p_k$  is about 20% for  $X=8\text{ m} \pm 5\text{ m}$ .

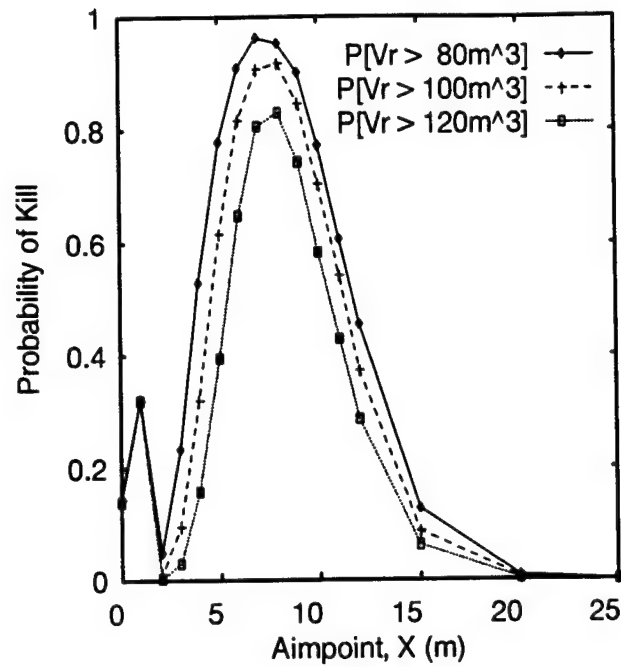


Figure 5-17. Variation in probability of kill with aimpoint.

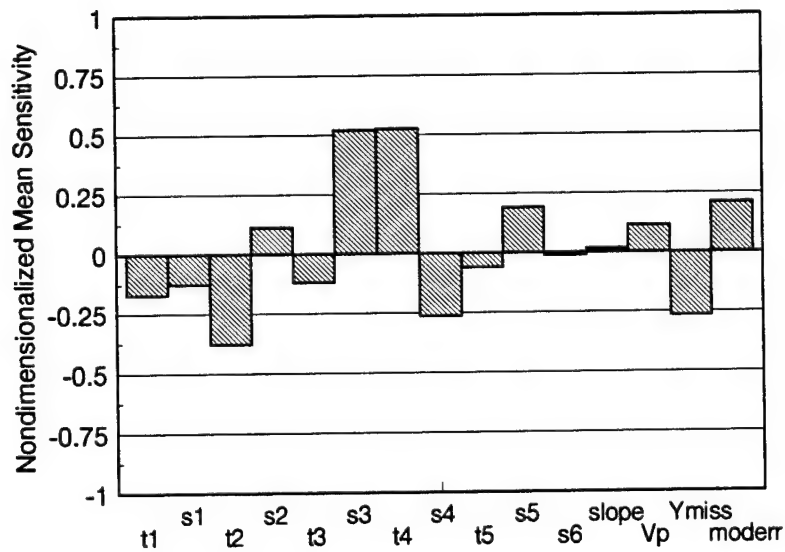


Figure 5-18. Nondimensionalized sensitivity of  $p_k$  with respect to the mean of each parameter.

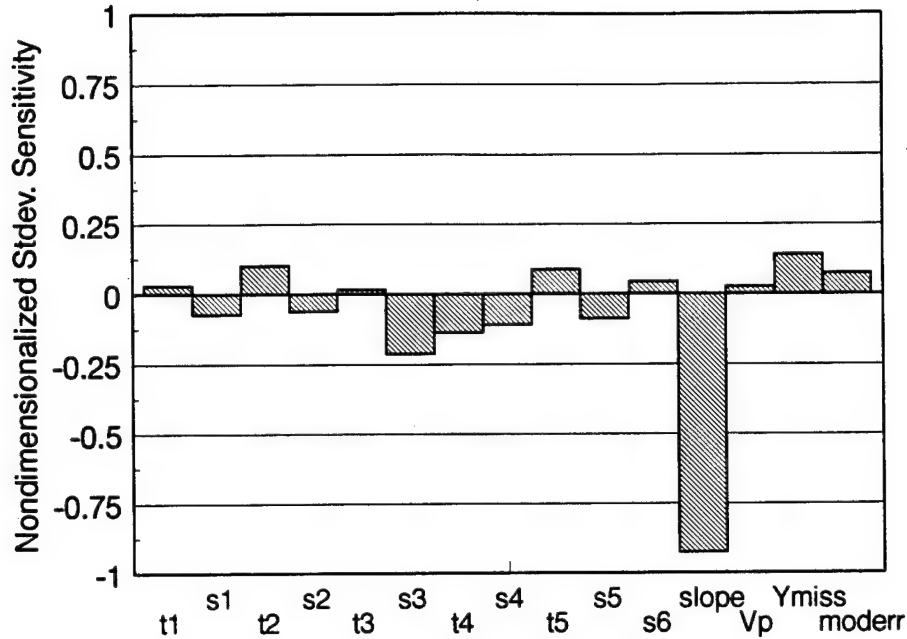


Figure 5-19. Nondimensionalized sensitivity of  $p_k$  with respect to the standard deviation of each parameter.

In Figures 5-18 and 5-19, the nondimensionalized sensitivity coefficients  $S_\mu$  and  $S_\sigma$  are plotted (see Section 4.9.3 for the definition).  $S_\mu$  measures the sensitivity of  $p_k$  with respect to the mean value of each random variable, and  $S_\sigma$  measures the sensitivity of  $p_k$  with respect to the standard deviation of each random variable. Thus, it is seen that changing the mean value of the S-number for layer 3 ( $S_3$ ) and thickness of layer 4 ( $t_4$ ), or the standard deviation of the slope angle will have the largest impact on  $p_k$ .

#### 5.4 PROBABILISTIC SWAT-II ANALYSIS.

The refined model of the SWAT II dynamic test was analyzed probabilistically. The mesh is shown in Figure 5-20. The deterministic model inputs and loading are the same as those given in Section 3.3.2. The refined model used here was created after the verification and validation exercise reported in Section 3.3.2 was completed. The purpose of this analysis is to explore which problem variables are the most important with respect to tunnel failure. The random variables are defined in Table 5-4 along with the correlation matrix in Table 5-5. These probabilistic inputs were obtained by Fossum, *et al.*, (1995) and used by Thacker and Senseny (1994) to explore the significance of correlations on the computed cdf results. The load scale factor term listed in Table 5-4 acts as a multiplier on the velocity time history used as input to the SWAT-II calculation; therefore, it is given a mean of 1.0. The standard deviation and distribution were selected arbitrarily to be 0.1 and normal respectively. There is no correlation between the load scale factor and the other random variables.

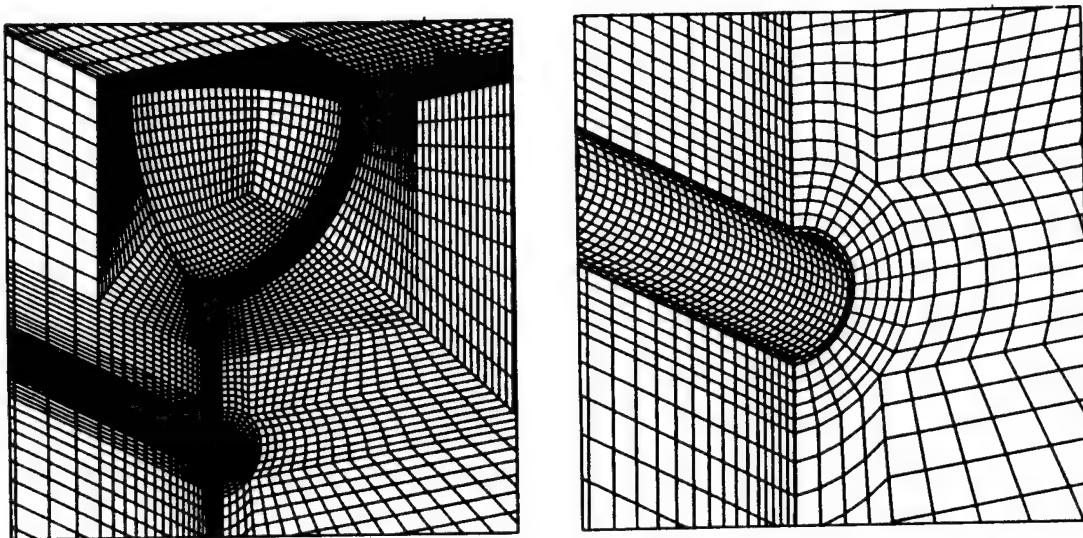


Figure 5-20. Refined mesh used for the probabilistic SWAT-II analysis.

Table 5-4. Parameter summary.			
Parameter	Mean Value	Std. Deviation	Prob. Distribution
K (MPa)	15725	761	Lognormal
G (MPa)	9112	290	Lognormal
A (MPa)	689.5	2.5	Normal
B (MPa <sup>-1</sup> )	3.90E-04	4.70E-06	Lognormal
C (MPa)	673.2	2.6	Normal
D(MPa <sup>-1</sup> )	1.4EE-03	8.49E-05	Weibull
W	0.08266	0.00424	Weibull
R	4.215	0.215	Weibull
X <sub>0</sub>	-468.1	4.5	Normal
Load scale factor	1.0	0.1	Normal

Table 5-5. Correlation matrix.									
	K	G	A	B	C	D	W	R	X <sub>0</sub>
K	1.00								
G	-0.0302	1.00							
A	0.1582	-0.0606	1.00						
B	-0.1677	0.0594	-0.0966	1.00					
C	0.1351	-0.0519	0.9901	0.0411	1.00				
D	-0.0101	0.0141	-0.6683	-0.6094	-0.7470	1.00			
W	-0.0082	-0.0397	0.5596	0.4821	0.6168	-0.8446	1.00		
R	-0.0319	0.0395	-0.7899	-0.4051	-0.8485	0.8356	-0.8755	1.00	
X <sub>0</sub>	0.0629	0.0172	0.4839	0.2867	0.5347	-0.4802	-0.0302	-0.2752	1.00

The cdf is shown in Figure 5-21 along with the 50% and 80% confidence intervals. The AMV+ analysis procedure is used to compute the cdf and required 33 model solutions. The confidence bounds are computed based on the coefficient of variation (COV) of the mean and the standard deviation using 20 test samples following the procedures described in Section 4.8. The COV of the mean and standard deviation for each variable is shown in Table 5-6.

Table 5-6. COV for the random variable mean and standard deviation.		
Parameter	Mean COV	Standard Deviation COV
K (MPa)	0.019	0.16
G (MPa)	0.017	0.16
A (MPa)	0.019	0.16
B (MPa <sup>-1</sup> )	0.428	0.16
C (MPa)	0.016	0.16
D (MPa <sup>-1</sup> )	0.131	0.16
W	0.131	0.16
R	0.017	0.16
X <sub>0</sub>	0.012	0.16
Load scale factor	0.100	0.10

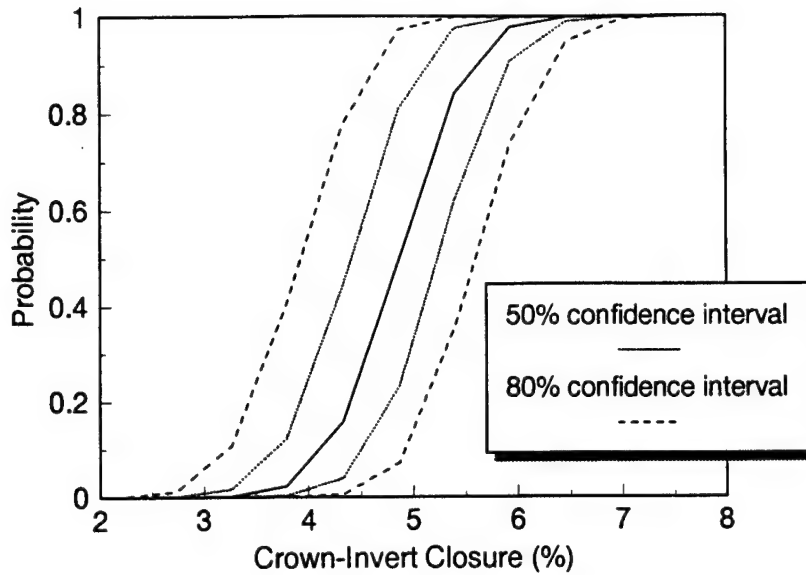


Figure 5-21. CDF of crown-invert closure showing 50% and 80% confidence bounds.

The sensitivity measures are the change in Beta with respect to the mean and standard deviation. These sensitivities are shown in Figures 5-22 and 5-23. The results indicate that the mean value of A and C contribute significantly to the variations in tunnel closure. With respect to the standard deviation, the load is completely dominate.

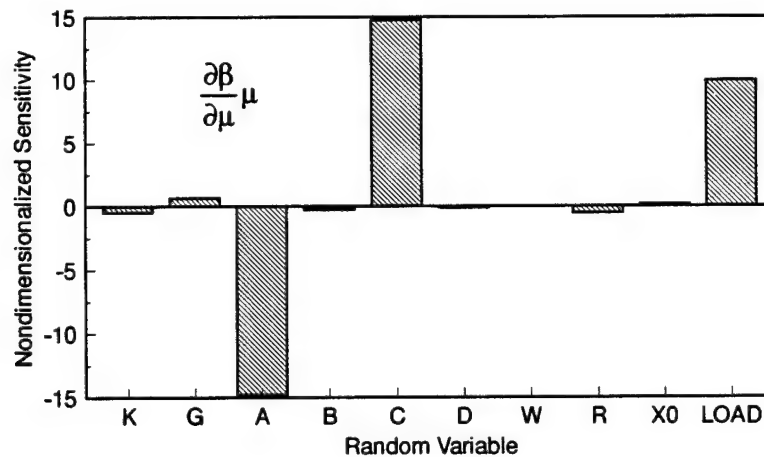


Figure 5-22. Nondimensionalized sensitivity of  $\beta$  with respect to the mean.

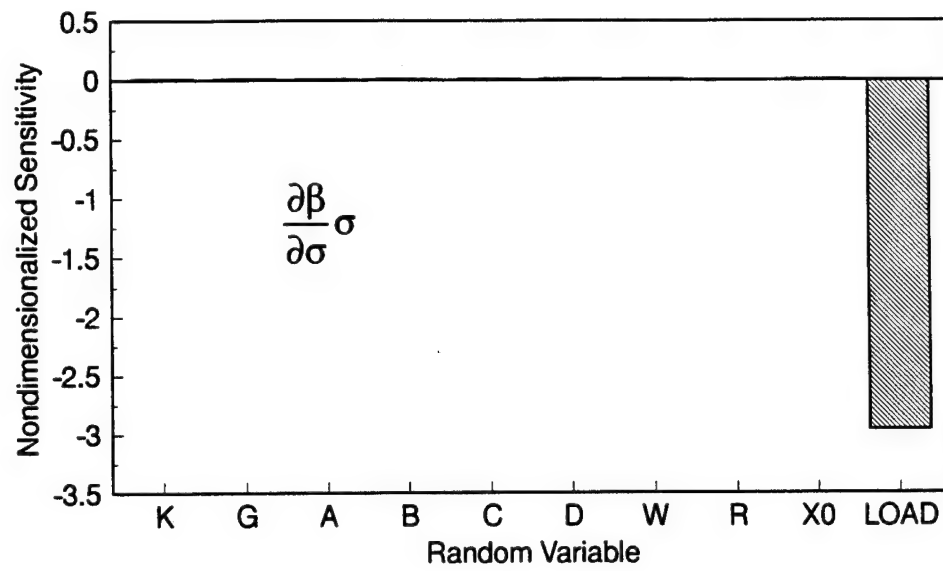


Figure 5-23. Nondimensionalized sensitivity of  $\beta$  with respect to the standard deviation.



## SECTION 6

### REFERENCES

Adley, M.D., R.P. Berger, and D.C. Creighton, "Two-Dimensional Projectile Penetration into Curvilinear Geologic/Structural Targets: User's Guide for PENCURV-PC," Version 1.5, Instruction Report SL-94-1, U.S. Army Corps of Engineers Waterways Experiment Station, 1994. (UNCLASSIFIED)

Ang, A.H.-S., and W.H. Tang, "Probability Concept in Engineering Planning and Design," Volume II: Decision, Risk, and Reliability, New York, John Wiley & Sons, Inc., 1984. (UNCLASSIFIED)

Bandis, S.C., A.C. Lumsden, and N.R. Barton, "Fundamentals of Rock Joint Deformation," *Int. J. of Rock Mech. and Mining Sciences and Geomechanics Abstracts*, Vol. 20, No. 6, pp. 249-268, 1983. (UNCLASSIFIED)

Bathe, K.J., and E.L. Wilson, Numerical Methods in Finite Element Analysis, Prentice-Hall, NJ, 1976. (UNCLASSIFIED)

Callahan, G.D., A.F. Fossum, and D.K. Svalstad, "Documentation of SPECTROM-32: A Finite Element Thermomechanical Stress Analysis Program," DOE/CH/10378-2, prepared by RE/SPEC Inc., Rapid City, SD for the U.S. Department of Energy, Chicago Operations Office, 1989. (UNCLASSIFIED)

Chen, W.F., and D.J. Han, "Plasticity for Structural Engineers," Springer-Verlag, New York, 1988. (UNCLASSIFIED)

Chitty, D., "Site Properties for Tunnel Vulnerability Calculations," Applied Research Associates, FAX memorandum dated March 13, 1995. (UNCLASSIFIED)

Cruse, T.A., O.H. Burnside, Y.-T. Wu, E.Z. Polch, P.K. Find, J.B. Dias, and K.R. Rajagopal, "Probabilistic Structural Analysis Methods for Select Space Propulsion System Structural Components (PSAM)," *Computers & Structures*, Vol. 29, No. 5, pp. 891-901, 1988. (UNCLASSIFIED)

Duvant, G., and J.L. Lions, Inequalities in Mechanics and Physics, (Translated from the original French version), Springer-Verlag, New York, 1972. (UNCLASSIFIED)

Flanagan, D.P., and T. Belystchko, "A Uniform Strain Hexahedron and Quadrilateral with Orthogonal Hourglass Control," *Int. J. Numer. Meth. Eng.*, Vol. 16, pp. 679-706, 1981. (UNCLASSIFIED)

Flanagan, D.P., and T. Belytschko, "Eigenvalues and Stable Time Steps for the Uniform Strain Hexahedron and Quadrilateral," *Jour. Appl. Mech.*, 84-APM-5. Transactions of the ASME, 1984. (UNCLASSIFIED)

Florence, A.L., and L.E. Schwer, "Axisymmetric Compression of a Mohr-Coulomb Medium Around a Circular Hole," *International Journal for Numerical and Analytical Methods in Geomechanics*, Vol. 2, pp. 367-379, 1978. (UNCLASSIFIED)

Fossum, A.F., T.W. Pfeifle, and K.D. Mellegard, "Experimental Determination of Probability Distributions for Parameters of a Salem Limestone Cap Plasticity Model," RE/SPEC Inc., DNA-TR-94-39, 1995. (UNCLASSIFIED)

Goodman, R.E., Methods of Geological Engineering in Discontinuous Rocks, West Publishing Company, New York. (UNCLASSIFIED)

Green, S.J., and R.D. Perkins, "Triaxial Compression Tests at Varying Strain Rates on Three Geologic Materials," Basic and Applied Rock Mechanics, R.E. Gray (ed.), Proc. 10th Symp. Rock Mechanics, Austin, TX, 1972. (UNCLASSIFIED)

Harren, S.V., "Non-Normal Correlated Random Variables," *Probabilistic Structural Analysis Methods & NESSUS Workshop, Vol. II*, Lecture Notes, Southwest Research Institute, San Antonio, TX, 1990. (UNCLASSIFIED)

Hendron, A.J., and A.K. Aiyer, "Stresses and Strains Around a Cylindrical Tunnel in an Elasto-Plastic Material with Dilatancy," Technical Report No. 10, U.S. Army Corps of Engineers, Omaha District, 1972. (UNCLASSIFIED)

Hohenbichler, M. and R. Rackwitz, "Non-normal Dependent Vectors in Structural Safety," *J. of Engineering Mechanics*, ASCE, Vol. 100, No. EM6, pp. 1227-1238, 1981. (UNCLASSIFIED)

Iman, R.L., and W.J. Conover, "A Distribution-Free Approach to Inducing Rank Correlation Among Input Variables," *Comm. in Statistics*, Vol. B11, No. 3, pp. 311-334, 1982. (UNCLASSIFIED)

Key, S.W., Z.E. Beisinger, and R.D. Krieg, "HONDO II: A Finite Element Computer Program for the Large Deformation Dynamic Response of Axisymmetric Solids," SAND78-0422, Sandia National Laboratories, Albuquerque, NM, 1978. (UNCLASSIFIED)

Labreche, D.A., and S.V. Petney, "The SPECTROM-31 Compliant Joint Model: A Preliminary Description and Feasibility Study," SAND85-7100, prepared by RE/SPEC Inc., Albuquerque, NM, for Sandia National Laboratories, Albuquerque, NM, 1987. (UNCLASSIFIED)

Liu, P.-L. and A. Der Kiureghian, "Structural Reliability under Incomplete Probability Information," *J. of Engineering Mechanics*, ASCE, Vol. 112, No. 1, pp. 85-104, 1986. (UNCLASSIFIED)

Lysmer, J., and R.L. Kuhlemeyer, "Finite Dynamic Model for Infinite Media," *J. Eng. Mech. Div.*, ASCE, pp. 859-877, August, 1979. (UNCLASSIFIED)

Madsen, H.O., S. Kernk, and N.C. Lind, Methods of Structural Safety, Englewood Cliffs, New Jersey: Prentice Hall, IN, 1986. (UNCLASSIFIED)

McKay, M.D., W.J. Conover, and R.J. Beckman, "A Comparison of Three Methods for Selecting Values of Input Variables in the Analysis of Output from a Computer Code," *Technometrics*, Vol. 21, pp. 239-245, 1979. (UNCLASSIFIED)

Nataf, A., "Determination des Distribution dont les Marges sont Donnees," *Comptes Rendus de l'Academit des Sciences*, Paris, France, Vol. 225, pp. 42-43, 1962. (UNCLASSIFIED)

Newmark, N.M., "Design of Rock Silo and Rock Cavity Linings," Appendix II of Ground Motion Technology Review, SAMSO TR-70-114, 1969. (UNCLASSIFIED)

Osnes, J.D., "Summary of Underground Technology Program (UTP) Benchmark Calculations," RE/SPEC Technical Letter Memorandum RSI/TLM-0174, 1991. (UNCLASSIFIED)

Perzyna, P., "Fundamental problems in viscoplasticity," *Advances in Applied Mechanics*, Vol. 9, pp. 244-368, 1966. (UNCLASSIFIED)

Riha, D.S., B.H. Thacker, and J.D. Osnes, "Probabilistic Analysis of Deep Tunnels Involving Explicit Dynamic Finite Element Calculations," *Probabilistic Method in Geomechanics*, A.F. Fossum (ed.), ASME, AMD-Vol. 134, 1992. (UNCLASSIFIED)

Rosenblatt, M., 1952, "Remark on a Multivariate Transformation," *The Annals of Mathematical Statistics*, Vol. 23, No. 3, pp. 470-472. (UNCLASSIFIED)

Sandler, I.S., and D. Rubin, "An Algorithm and a Modular Subroutine for the Cap Model," *Int. J. Numer. Anal. Methods Geomech.*, Vol. 3, pp. 173-186, 1979. (UNCLASSIFIED)

Senseny, P.E., and D.A. Simons, "Comparison of Calculational Approaches for Structural Deformation in Jointed Rock," *Int. J. Numer. Anal. Meth. in Geomech.*, Vol. 18, 327-344, 1994. (UNCLASSIFIED)

Shooman, M.L., Probabilistic Reliability: An Engineering Approach, McGraw-Hill Book Co., No. CO2, September 1967. (UNCLASSIFIED)

Simons, D.A., "Numerical and Analytical Solutions to Benchmark Problems Related to Tunnel Mechanics," DNA-TR-92-176, Logicon RDA, 1993. (UNCLASSIFIED)

Simons, J.W., L. Seaman, P.R. Gefken, and A.L. Florence, "Tunnel Tests in Limestone," DNA-TR-92-164, 1993. (UNCLASSIFIED)

Southwest Research Institute, "NESSUS/PRE User's Manual," Version 1.0, San Antonio, Texas, July, 1991. (UNCLASSIFIED)

Taylor, L.M., and D.P. Flanagan, "PRONTO 2D: A Two-Dimensional Transient Solid Dynamics Program," SAND86-0594, Sandia National Laboratories, Albuquerque, NM, 1987. (UNCLASSIFIED)

Thacker, B.H., H.R. Millwater, and S.V. Harren, "Computational Methods for Structural Load and Resistance Modeling," Proc., 32nd AIAA/ASME/ASCE/AHS/ASC Structures, Structural Dynamics and Materials (SDM) Conf., Baltimore, Maryland, Paper No. AIAA-91-0918, pp. 1227-1235, AIAA, Washington, D.C., April 7-10, 1991. (UNCLASSIFIED)

Thacker, B.H., and P.E. Senseny, "Probabilistic Structural Analysis of Deep Tunnels," AMD-Vol. 134, Probabilistic Methods in Geomechanics, A.F. Fossum (ed.), pp. 1-13, ASME, Scottsdale, AZ, April 28-May 1, 1992. (UNCLASSIFIED)

Thacker, B.H., and P.E. Senseny, "Approximation of the Joint Density Function for the Parameters in a Probabilistic CAP Model," Proc. Computer Methods and Advances in Geomechanics, H.J. Siriwardane and M.M. Zaman (eds.), Vol. II, pp. 1705-1710, 1994. (UNCLASSIFIED)

Thacker, B.H. and Y.-T. Wu, "Sampling-based Probabilistic Sensitivity Analysis" Proc., 24th Midwestern Mechanics Conference, Ames, IA, 1995. (UNCLASSIFIED)

Torng, T.Y., and B.H. Thacker, "Confidence Bounds Assessment for Probabilistic Structural Reliability Analysis," Proc. 33rd AIAA/ASME/ASCE/AHS/ASC Structures, Structural Dynamics, and Materials Conf., Paper No. AIAA-92-2409, Dallas, TX, April 13-15, 1992a. (UNCLASSIFIED)

Torng, T.Y., and B.H. Thacker, "Probabilistic Assessment of Uncertainties in Geomechanics Problems," AMD-Vol. 134, Probabilistic Methods in Geomechanics, A.F. Fossum (ed.), pp. 27-40, ASME, Scottsdale, AZ, April 28-May 1, 1992b. (UNCLASSIFIED)

Torng, T.Y., and B.H. Thacker, "An Efficient Probabilistic Scheme for Constructing Structural Reliability Confidence Bounds," Proc. 34th AIAA/ASME/ASCE/AHS/ASC SDM - Structures, Structural Dynamics, and Materials Conf., Paper No. AIAA-93-1627, La Jolla, CA, April 19-21, 1993. (UNCLASSIFIED)

Tvedt, L., "Distribution of Quadratic Forms in Normal Space—Application to Structural Reliability," *J. of Engineering Mechanics*, ASCE, Vol. 116, No. 6, June, pp. 1183-1197, 1990. (UNCLASSIFIED)

William, K.J., and E.P. Warnke, "Constitutive Model for the Triaxial Behavior of Concrete," *Pres. Seminar Concrete Structures Subjected to Triaxial Stresses*, ISMES, Bergamo, Italy, pp. 1-30, 1975. (UNCLASSIFIED)

Wintergerst, G.L., D.N. Burgess, J.L. Merritt, and P.E. Senseny "Axisymmetric Compression of a Mohr-Coulomb Medium with Arbitrary Dilatancy," DNA-001-87-C-0259, 1991. (UNCLASSIFIED)

Wu, Y.-T., O.H. Burnside, and T.A. Cruse, "Probabilistic Methods for Structural Response Analysis," Computational Mechanics of Probabilistic and Reliability Analysis, W.K. Liu and T. Belytchko (eds.), Elmeppress Int., Lausanne, Switzerland, 1989. (UNCLASSIFIED)

Wu Y.-T. and O.H. Burnside, "Efficient Probabilistic Structural Analysis Using an Advanced Mean Value Method," Proc. ASCE Specialty Conf. on Probabilistic Mechanics and Structural and Geotechnical Safety, Virginia Polytechnic Institute and State University, Blacksburg, Virginia, pp. 492-495, May 25-27, 1988. (UNCLASSIFIED)

Wu, Y.-T., H.R. Millwater, and T.A. Cruse, "Advanced Probabilistic Structural Analysis Method for Implicit Performance Functions," *AIAA Journal*, Vol. 28, No. 9, 1990. (UNCLASSIFIED)

Wu, Y.-T. and P.H. Wirsching, "A New Algorithm for Structural Reliability Estimation," *Journal of Engineering Mechanics*, Vol. 113, No. 9, ASCE Paper No. 21770, 1987. (UNCLASSIFIED)

Wu, Y.-T., "Computational Methods For Efficient Structural Reliability And Reliability Sensitivity Analysis," *AIAA Journal*, Vol 32, No. 8, pp. 1717-1723, 1994. (UNCLASSIFIED)

## DISTRIBUTION LIST

DNA-TR-95-64

### DEPARTMENT OF DEFENSE

DEFENSE INTELLIGENCE AGENCY  
ATTN: PGI-4B

DEFENSE NUCLEAR AGENCY  
2 CY ATTN: ISST  
ATTN: OPNA  
ATTN: PMT P SENSENY  
ATTN: WEL D PYLE

DEFENSE TECHNICAL INFORMATION CENTER  
2 CY ATTN: DTIC/OCF

FIELD COMMAND DEFENSE NUCLEAR AGENCY  
ATTN: FCTO  
ATTN: FCTOS  
ATTN: FCTT DR BALADI

### DEPARTMENT OF THE ARMY

ADVANCED RESEARCH PROJECT AGENCY  
ATTN: DEFENSE SCIENCES OFFICE

U S ARMY CORPS OF ENGINEERS  
ATTN: CERD-L

U S ARMY ENGINEER DIST OMAHA  
ATTN: MROED-S H GAUBE

U S ARMY ENGR WATERWAYS EXPER STATION  
ATTN: C D NORMAN  
ATTN: CEWES-SD  
ATTN: CEWES-SE L K DAVIS  
ATTN: CEWES-SS-R DR BALSARA  
ATTN: DR D BANKS CEWES-GS  
ATTN: J WARRINER WESGR-M  
ATTN: RESEARCH LIBRARY  
ATTN: W MCMAHON  
ATTN: W MILLER

### DEPARTMENT OF THE AIR FORCE

AIR FORCE CTR FOR STUDIES & ANALYSIS  
ATTN: AFSAA/SAI

AIR UNIVERSITY LIBRARY  
ATTN: AUL-LSE

### DEPARTMENT OF ENERGY

LOS ALAMOS NATIONAL LABORATORY  
ATTN: REPORT LIBRARY

SANDIA NATIONAL LABORATORIES  
ATTN: TECH LIB 3141  
ATTN: 9312 C W SMITH  
ATTN: 9700 A F FOSSUM

### OTHER GOVERNMENT

CENTRAL INTELLIGENCE AGENCY  
ATTN: OSWR/NED 5S09 NHB

DEPARTMENT OF THE INTERIOR  
ATTN: P SANDS

### DEPARTMENT OF DEFENSE CONTRACTORS

AEROSPACE CORP  
ATTN: LIBRARY ACQUISITION

ANALYTIC SERVICES, INC (ANSER)  
ATTN: K BAKER

APPLIED RESEARCH ASSOCIATES, INC  
ATTN: C J HIGGINS

APPLIED RESEARCH ASSOCIATES, INC  
ATTN: S BLOUIN

APPLIED RESEARCH ASSOCIATES, INC  
ATTN: R FRANK

APTEK, INC  
ATTN: B LEWIS  
ATTN: Y MURRAY

BOEING TECHNICAL & MANAGEMENT SVCS, INC  
ATTN: W M LEAVENS  
ATTN: A W SPENCER  
ATTN: R BRYAN CAIRNS

IIT RESEARCH INSTITUTE  
ATTN: DOCUMENTS LIBRARY  
ATTN: M JOHNSON

INSTITUTE FOR DEFENSE ANALYSES  
ATTN: CLASSIFIED LIBRARY

JAYCOR  
ATTN: CYRUS P KNOWLES

KAMAN SCIENCES CORP  
ATTN: RICHARD KEEFFE

KAMAN SCIENCES CORPORATION  
ATTN: DASIAC

LACHEL AND ASSOCIATES, INC  
ATTN: C LINAMEN  
ATTN: J BECK

LOGICON R & D ASSOCIATES  
ATTN: DR T A PUCIK  
ATTN: LIBRARY

LOGICON R & D ASSOCIATES  
ATTN: E HUMPHREYS

MAXWELL LABORATORIES INC  
ATTN: K D PYATT JR

NTS ENGINEERING  
ATTN: S SHORT

PACIFIC-SIERRA RESEARCH CORP  
ATTN: H BRODE

PACIFIC-SIERRA RESEARCH CORP  
ATTN: D GORMLEY

DNA-TR-95-64 (DL CONTINUED)

SCIENCE APPLICATIONS INTL CORP  
ATTN: H PRATT  
ATTN: M MCKAY  
ATTN: TECHNICAL REPORT SYSTEM

SCIENCE APPLICATIONS INTL CORP  
ATTN: W LAYSON

SOUTHWEST RESEARCH INSTITUTE  
2 CY ATTN: B THACKER  
2 CY ATTN: D S RIHA  
2 CY ATTN: Y T WU

SRI INTERNATIONAL  
ATTN: DR JIM GRAN

TITAN CORPORATION  
ATTN: J THOMSEN

TITAN CORPORATION (THE)  
ATTN: LIBRARY  
ATTN: S SCHUSTER  
ATTN: Y M ITO

TRW SPACE & DEFENSE SECTOR SPACE &  
ATTN: W WAMPLER

UTD, INC  
ATTN: E FOSTER

WEIDLINGER ASSOC, INC  
ATTN: E WONG  
ATTN: H LEVINE

WEIDLINGER ASSOCIATES, INC  
ATTN: I SANDLER  
ATTN: M BARON